NTNU
Norwegian University of
Science and Technology

Understanding the growth and physico-chemical properties of multifunctional nanoparticles

Jibin Antony

Chemical Engineering
Submission date: August 2018
Supervisor: Jens-Petter Andreassen, IKP
Co-supervisor: Sulalit Bandyopadhyay, IKP
Karthik Raghunathan, IKP

Norwegian University of Science and Technology
Department of Chemical Engineering

Abstract

Gold nanoparticles (Au NPs) exhibit localized surface plasmon resonance (LSPR) that provides wide applications in photothermal therapy, imaging and other theranostic[1] applications. Recently, understanding the growth of anisotropic Au nanostructures has become an important topic of interest, since by controlling their growth, it is possible to optimize their physico-chemical properties. On the other hand, another class of nanomaterials that has garnered interest for stimuli directed release of cargo molecules are nanogels (NGs). Although NGs were initially studied for their temperature responsive behavior, it is possible to incorporate other sensitivities like pH, light, magnetism and so on to make them multifunctional.

In this project, polymerization methods developed in Ugelstad Laboratory were used to synthesize stimuli-responsive NGs and NGs coupled with inorganic NPs that can be triggered to release a cargo of interest in a controlled manner. Hybrid NPs (obtained by combining NGs with inorganic NPs) were synthesized via in situ polymerization by combining Au NSs with temperature and pH sensitive pNIPAm-AAc NGs. Primary focus of the study was on optimization of system parameters in order to modify the physico-chemical properties of the constructs. Three different molar ratios of the monomers were used to synthesize NGs/hybrid NPs having different physico-chemical properties. Increased size and stability of NGs/hybrid NPs could be observed at high AAc mole ratio.

The effect of size, concentration and surface charge of the NPs on the properties of resulting hybrid NP was studied. An optimum weight of 0.75 mg Au NS was chosen for the studies as it was shown to give prominent LSPR peak of Au, thereby enabling detection in addition to enhanced physico-chemical properties of the hybrid. The swelling-collapse properties of hybrid NPs in response to pH and temperature were compared to that of NGs at different molar ratios of AAc. Rapid swelling-deswelling characteristics were observed for NG/hybrid NP samples at high AAc mole ratio. Swelling effects were observed with an increase in pH for NG/hybrid NP samples maintained above their VPTT.

Time based studies were performed to obtain an understanding of the growth mechanisms involved in the synthesis of NGs/hybrid NPs. Loading studies were performed on these nanocarriers via breathing-in technique using Cyt C as model drug. Two different methods (dialysis and centrifuging) were studied to separate free Cyt C from the loaded systems. Since the maximum deviation observed in loading efficiencies (LEs) from these methods were only

[1] Combination of diagnostics and therapy

around ~13%, they were found to be comparable at all molar ratios of AAc. LEs were found to increase in NGs/hybrid NPs with an increase in AAc content, with values ranging from ~30% (AAc:10) to ~71% (AAc:25). The encapsulation efficiencies (EEs) were observed to range from ~180 µg/mg (AAc:10) to ~417 µg/mg (AAc:25).

Drug release profiles of bare NGs and hybrid NPs were studied at low pH (pH 3) and with an additional temperature stimulus (pH 3 + 40°C). Increased values of release exponents with additional temperature stimulus indicated a switch in geometry of the NG/hybrid NP matrix from spherical/cylindrical to thin film. This was also associated with a change in transport mechanism from anomalous transport to Case-II/Super Case-II transport.

Preface

This thesis is being delivered to the Chemical Engineering Department at Norwegian University of Science and Technology (NTNU) in partial fulfilment for the degree of Master of Science (MSc). This project is a part of a larger research study performed by our group to understand the growth and physico-chemical properties of multifunctional NPs and to study their potential in drug delivery applications. The work presented in this thesis was carried out at Ugelstad Laboratory and Crystallization Laboratory in the Department of Chemical Engineering, and Nanolab, NTNU. This work was performed under the supervision of Dr. Jens-Petter Andreassen and co-supervised by Dr. Sulalit Bandyopadhyay.

I completed my Bachelor's in Chemical Engineering from National Institute of Technology Calicut, India in May 2013 and thereafter worked in Reliance Industries Limited, Jamnagar, India for three years. After this stint in the industry, I joined NTNU for my Master's in Chemical Engineering in August 2016.

Dedicated to my family for helping me
finish this race strong.

Acknowledgement

First and foremost, I would like to express my deepest gratitude to my supervisor, Prof. Jens-Petter Andreassen, for his constant support and guidance in spite of his busy schedule. Thank you for giving me the opportunity to work on this exciting project and for enlightening me with your valuable suggestions during the group meetings.

I am extremely thankful to my co-supervisor, Dr. Sulalit Bandyopadhyay, for introducing me to the big world of small things[2]. Thank you for instilling in me ideas and perspectives for tackling problems in a field which was rather new to me and for being there as a constant pillar of support and guidance.

A special thanks to Karthik Raghunathan for being there as a mentor and for helping and motivating me throughout this work. From giving valuable inputs during group meetings to answering every little query of mine, you were there like a brother to help me at all times. I would like to thank Romit for familiarizing me with the reaction setup and for helping me with the initial experiments. Special thanks goes to all Post-Doc's, PhDs, and my fellow master students in Ugelstad Lab for their help and for making life easier in the lab.

This journey would not have been possible if not for the moral support that I received from my family and friends. You all were there to boost me during tough times and showed faith in me throughout. I love you all.

Finally, I thank God for providing me the strength and blessings for making this attempt a fruitful one.

[2] nanoparticles

Table of Contents

Abstract i

Preface iii

Acknowledgement vii

Table of Contents ix

List of Figures xiii

List of Tables xix

List of Abbreviations xxi

1 Introduction 1

2 Literature Review 5

2.1 Inorganic NPs 5

2.1.1 Au NPs 5

2.2 Polymer based NPs 8

2.2.1 Polymeric Micelles 9

2.2.2 Dendrimers 9

2.2.3 Hydrogels 10

2.3 Hybrid NPs 14

2.4 Synthesis of multifunctional NPs 15

2.4.1 Solution based reduction of metal precursor 15

2.4.2 Reverse micellar template 15

2.4.3 Precipitation polymerization 16

2.5 Recent advances on multifunctional NPs 16

2.5.1 Inorganic multifunctional NPs 16

2.5.2 Polymer based multifunctional NPs 20

2.5.3 Hybrid multifunctional NPs 22

3 Material and Methods 25

3.1 Materials 25

3.1.1 Chemicals used 25
3.2 Methods 25
3.2.1 Synthesis of Au NSs 26
3.2.2 Recrystallization of NIPAm 28
3.2.3 Synthesis of NGs 29
3.2.4 Synthesis of hybrid NPs 30
3.2.5 Dialysis 31
3.2.6 Freeze-drying 31
3.2.7 Timed Experimental Study 32
3.2.8 Loading 32
3.2.9 Release Studies 33
3.2.10 Characterization Techniques 34
3.2.11 Analysis Techniques 38
4 Results and Discussion 41
4.1 Synthesis and Characterization of Inorganic NSs 41
4.2 Synthesis and Characterization of NGs 43
4.2.1 Effect of changing pH of reaction medium 45
4.3 Synthesis and Characterization of hybrid NPs 47
4.3.1 Effect of Concentration 48
4.3.2 Effect of Size 51
4.3.3 Effect of surface charge 52
4.4 Swelling-Collapse properties as a function of temperature 53
4.5 Swelling-Collapse properties in response to pH 56
4.6 Time based studies 60
4.7 Characterization of Freeze-dried samples 64
4.8 Loading studies 66
4.9 Drug Release studies 72

5 Conclusion 85
6 Future work 87
7 Bibliography 89
Appendix 95
A. Significance of recrystallization of NIPAm batch 95
B. Effect of stirring speed in synthesis of hybrid NPs 95
C. Size versus Temperature plots 96
D. Curve fitting on normalized growth curves 97
E. Percentage removal of Cyt C using dialysis 98
F. Calculating loading and encapsulation efficiencies 98
G. Finding drug release profiles and kinetics 99
H. Fitting release models for pH controlled release 101
I. Fitting release models for pH + Temperature controlled release 104

List of Figures

Figure 1.1: Schematic representation of multifunctional NPs [7]. 2

Figure 2.1: Schematic representation of LSPR in a metallic NP [23]. 6

Figure 2.2: UV-Vis spectra of colloidal aqueous solutions of Au NPs. Dashed curve: NS; Solid curve: NR. 6

Figure 2.3: Schematic illustration of seed-mediated growth method. 8

Figure 2.4: Schematic showing the location of drug inside a nanocapsule and nanosphere [31]. 9

Figure 2.5: Schematic representation of the structure of (a) polymeric micelles [36] (b) dendrimer [37]. 10

Figure 2.6: Phase transition in a stimuli-sensitive hydrogel [45]. 11

Figure 2.7: Representation of phase transition associated with LCST and UCST [48]. 11

Figure 2.8: Chemical structure of pNIPAm indicating hydrophobic and hydrophilic regions [52]. 12

Figure 2.9: Precipitation polymerization in thermo-sensitive NGs [50]. 13

Figure 2.10: pH-responsive swelling/collapse behaviour of (a) anionic and (b) cationic hydrogels [45]. 13

Figure 2.11: Design strategies for different hybrid NPs based on location of functional nanocomponent; Functional nanocomponent located (a) at the surface, and (b) within the structural nanocomponent . 15

Figure 2.12: Schematic illustration of reverse micellar synthesis (a) reverse micelles containing metal precursor and reducing agent subject to Brownian motion (b) Fusion of cores followed by reaction (c) Formation of metal NP [59]. 16

Figure 2.13: Schematic showing sequence of synthesis of PEG modified Fe@Au NPs [60]. 17

Figure 2.14: Schematic illustration of the growth of Au-Fe_3O_4 dumbbell-like NPs [67]. 18

Figure 2.15: Stabilization of gold coated iron oxide NPs using thiolated SA [73]. 19

Figure 2.16: UV-Vis absorbance spectra of NIPAm and pNIPAm [76]. 21

Figure 2.17: UV-Vis absorption spectra of pNIPAm during polymerization initiated by KPS [76]. 22

Figure 3.1: Synthesis of citrate coated Au NS. 26

Figure 3.2: Citrate coated Au seed. 27

Figure 3.3: Schematic representation of the seed mediated growth (a) CTAB solution (b) after addition of $HAuCl_4$ (c) after adding AsA (d) 5 min after adding the seed (e) 12 hrs from seed addition. 28

Figure 3.4: Reaction setup for recrystallization. 29

Figure 3.5: Schematic depicting the sequence in NG synthesis. 30

Figure 3.6: Different concentrations of Au NSs re-dispersed in 5ml SDS solution. 30

Figure 3.7: Reaction setup for synthesis of hybrid NPs. 31

Figure 3.8: NG sample kept for overnight dialysis 31

Figure 3.9: Freeze-drying setup used for drying the samples. 32

Figure 3.10: Schematic depiction of breathing in technique. 33

Figure 3.11: Samples kept on shaking for loading Cyt C. 33

Figure 3.12: Samples kept on dialysis at release conditions. 34

Figure 3.13: (a) Malvern Zetasizer Nano-ZS (b) Folded capillary cell used for the zeta potential measurements [83]. 35

Figure 3.14: Auto-titrator for adjusting pH 36

Figure 3.15 (a): Transmission of light through a particle solution [84] (b) UV-Vis spectrophotometer. 37

Figure 3.16: Hitachi S-5500 S(T)EM. 38

Figure 3.17: Schematic showing calculation of VPTT. (a) Swelling ratios plotted as a function of temperature. (b) Fitting a sigmoidal 5 parameter curve. (c) Equalizing the area and determining VPTT using MATLAB code. 39

Figure 4.1: UV-Vis spectra and S(T)EM images of inorganic NSs used in the study. (a) Au NS1 (b) Au NS2 (c) Au NS3 (d) Ag NS. 42

Figure 4.2: Average (a) hydrodynamic sizes and (b) zeta potentials of inorganic NSs. 43

Figure 4.3: (a) Size comparison of NGs with increasing mole ratios of AAc (b) Change in VCE of NG with increasing mole ratio of AAc. 44

Figure 4.4: Change in zeta potential of NG with increasing mole ratio of AAc. 45

Figure 4.5: Variation in (a) size and (b) ZP of NG as a function of pH of reaction medium. . 46

Figure 4.6: Structure of SDS [86]. 47

Figure 4.7: NPs sticking to magnet after reaction. 47

Figure 4.8: Effect of concentration of inorganic NP on the (a) size, and (b) VCE of hybrid NP. 48

Figure 4.9: Normalized absorbance plot of hybrid NPs with various concentrations of NPs showing the peak for Au. 50

Figure 4.10: Comparing bNGs and hNPs of different AAc mole ratio..... 51

Figure 4.11: Effect of NP size on the size of hybrid NP. 52

Figure 4.12: Effect of NP surface charge on the (a) size, and (b) zeta potential of hybrid NP. 53

Figure 4.13: Swelling ratio versus temperature for (a) bNG_10 (b) hNP_10 (c) bNG_15 (d) hNP_15 (e) bNG_25 (f) hNP_25. 54

Figure 4.14: VPTT comparison between bNG and hNP at different AAc ratios..... 55

Figure 4.15: Effect of pH on (a) size and (b) ZP of bNG_10 and hNP_10; (c) size and (d) ZP of bNG_15 and hNP_15; (e) size and (f) ZP of bNG_25 and hNP_25. 57

Figure 4.16: Swelling of NGs with increase in pH at 45^{o}C (a) pH 3 (b) pH 7. 59

Figure 4.17: pH response of bNG and hNP at 25^{o}C and 45^{o}C, (a) bNG_10 and hNP_10, (b) bNG_15 and hNP_15, (c) bNG_25 and hNP_25. 60

Figure 4.18: Size as a function of reaction time for (a) bNG_10 and hNP_10, (b) bNG_15 and hNP_15, (c) bNG_25 and hNP_25..... 62

Figure 4.19: Normalized size (at 25C) of bNG and hNP as a function of time (a) bNG_10 and hNP_10 (b) bNG_15 and hNP_15 (c) bNG_25 and hNP_25. 63

Figure 4.20: ZP as a function of reaction time for hybrid NPs (AAc:10,15,25)..... 64

Figure 4.21: Comparison of (a) size, and (b) ZP of aqueous and freeze-dried NGs..... 65

Figure 4.22: Comparison of (a) size, and (b) ZP of aqueous and freeze-dried hybrid NPs. 65

Figure 4.23: VCE comparison of aqueous and freeze-dried (a) NGs (b) hybrid NPs..... 66

Figure 4.24: (a) Calibration curve of Cyt C; (b) Percentage removal of free Cyt C as a function of dialysis time. 67

Figure 4.25: Loaded samples post dialysis. (a) bNG_10 (b) bNG_15 (c) bNG_25 (d) hNP_10 (e) hNP_15 (f) hNP_25. 68

Figure 4.26: Staining observed in tubes post dialysis. (a) bNG_10 (b) bNG_15 (c) bNG_25 (d) hNP_10 (e) hNP_15 (f) hNP_25. 68

Figure 4.27: Cyt C loaded hybrid NP samples before and after centrifuging (a,d) hNP_10 (b,e) hNP_15 (c,f) hNP_25. 69

Figure 4.28:(a,b,c) Supernatant (2.5x dilution) of Cyt C loaded hybrid NPs (AAc:10, 15, 25 arranged from left to right); (d,e,f) Bottom precipitate (2.5x dilution) of Cyt C loaded hybrid NPs (AAc: 10, 15, 25 arranged from left to right). 70

Figure 4.29: Comparison of LEs obtained by dialysis and spinning methods. 71

Figure 4.30: (a) LEs as a function of increasing AAc content (b) EEs as a function of increasing AAc content. 72

Figure 4.31: ZP of NGs/hybrid NPs before and after loading Cyt C. 73

Figure 4.32: Cyt C release profile from bare NGs and hybrid NPs at pH 3. 74

Figure 4.33: Additional release of Cyt C from bare NGs and hybrid NPs by increasing the temperature to 40^{o}C without altering the pH from initial study(pH = 3). 75

Figure 4.34: Fitting release models in bNG_10 sample for studies performed at pH 3. (a) Zero order model (b) First order model (c) Higuchi model (d) Power law model. 78

Figure 4.35: Fitting release models in bNG_10 sample for studies performed at pH 3 + 40^{o}C. (a) Zero order model (b) First order model (c) Higuchi model (d) Power law model. 80

Figure 4.36: Fitting release models in hNP_10 sample for studies performed at pH 3 + 40^{o}C. (a) Zero order model (b) First order model (c) Higuchi model (d) Power law model. 81

Figure 7.1: Polymers (a) phase separating, (b) sticking to the magnet after the reaction. 95

Figure 7.2: Size versus temperature for (a) bNG_10 (b) hNP_10 (c) bNG_15 (d) hNP_15 (e) bNG_25 (f) hNP_25. 96

Figure 7.3: Sigmoidal 5 parameter curve fits for growth curves of (a) bNG_10 and hNP_10 (b) bNG_15 and hNP_15 (c) bNG_25 and hNP_25 97

Figure 7.4: Fitting release models in hNP_10 sample for studies performed at pH 3. (a) Zero order model (b) First order model (c) Higuchi model (d) Power law model. 101

Figure 7.5: Fitting release models in bNG_15 sample for studies performed at pH 3. (a) Zero order model (b) First order model (c) Higuchi model (d) Power law model. 102

Figure 7.6: Fitting release models in hNP_15 sample for studies performed at pH 3. (a) Zero order model (b) First order model (c) Higuchi model (d) Power law model. 103

Figure 7.7: Fitting release models in bNG_15 sample for studies performed at pH 3 + 40^{o}C. (a) Zero order model (b) First order model (c) Higuchi model (d) Power law model. 104

Figure 7.8: Fitting release models in hNP_15 sample for studies performed at pH 3 + 40^{o}C. (a) Zero order model (b) First order model (c) Higuchi model (d) Power law model. 105

Figure 7.9: Fitting release models in bNG_25 sample for studies performed at pH 3 + 40^{o}C. (a) Zero order model (b) First order model (c) Higuchi model (d) Power law model. 106

Figure 7.10: Fitting release models in hNP_25 sample for studies performed at pH 3 + 40^{o}C. (a) Zero order model (b) First order model (c) Higuchi model (d) Power law model. 107

List of Tables

Table 3.1: Different molar ratios of monomers used in NG synthesis 29

Table 4.1: DLS size, S(T)EM size and zeta potential of inorganic NSs. 43

Table 4.2: LEs and EEs of different NGs/hybrid NPs. 72

Table 4.3: Drug release mechanisms from different geometries based on the values of release exponent. 77

Table 4.4: Release Model, Higuchi dissolution constant and $t_{1/2}$ for bNG/hNP systems at pH 3. 79

Table 4.5: Release exponent and transport mechanism shown by bNG/hNP samples at pH 3. 79

Table 4.6: Release Model, rate constant and $t_{1/2}$ for bNG/hNP systems at pH 3 + 40^{o}C. 82

Table 4.7: Release exponent and transport mechanism for bNG/hNP systems at pH 3 + 40^{o}C. 82

Table 7.1: Release kinetics data for bNG_10 sample at pH 3. 100

List of Abbreviations

AAc	Acrylic Acid
AR	Aspect Ratio
AsA	Ascorbic Acid
Au NPs	Gold Nanoparticles
BIS	N, N'-Methylenebis(acrylamide)
Cyt C	Cytochrome C
DLS	Dynamic Light Scattering
E.E.	Encapsulation Efficiency
FD	Freeze-dried
hNP	Hybrid NP
KPS	Potassium Persulphate
LSPR	Localized Surface Plasmon Resonance
MWCO	Molecular Weight Cut-off
NIPAm	N-Isopropylacrylamide
NG / bNG	Nanogel / bare nanogel
NM	Nanomakura
NR	Nanorod
NPs	Nanoparticles
NS	Nanosphere
PDI	Polydispersity Index
pNIPAm	Poly(N-Isopropylacrylamide)
SDS	Sodium Dodecyl Sulphate
rpm	Revolutions per minute
S(T)EM	Scanning Transmission Electron Microscopy
UV-Vis	Ultraviolet-Visible
VCE	Volumetric Collapse Efficiency
VPTT	Volume Phase Transition Temperature
ZP	Zeta Potential

1 Introduction

Nanoparticles (NPs) have gained considerable interest of researchers in the recent years owing to their unique size dependent properties. Increased surface to volume ratio at the nanoscale results in unprecedented physico-chemical properties and superior performance of these NPs, which has led to their use in wide range of technological applications in fields ranging from electronics [1], energy [2-4], and biotechnology [5, 6] among others. Nanomedicine, which applies nanotechnology to healthcare, holds great potential for revolutionary medical treatments and therapies in areas such as imaging, quicker diagnosis, targeting and drug delivery [7].

The use of gold NPs (Au NPs) in drug delivery has gained significant importance due to its remarkable optical properties and ease of surface functionalization. Controlled release of the drug and other bio-therapeutic agents possess considerable advantages over the conventional release owing to reduced toxicity and improved drug effectiveness in addition to its fine-tuned release mechanism [8]. Though NP based drug delivery systems have demonstrated reduction in systemic toxicity of a wide range of drugs, their use has not always translated into enhanced clinical outcomes due to biocompatibility and stability issues [9]. This has led to the development of novel multifunctional NPs, by combining various NPs of different properties into a single construct, leading to enhanced physico-chemical properties of the hybrid.

Nanogels (NGs) are a potential class of polymer-based nanosized systems that has garnered interest in stimuli directed release of cargo molecules. These are smart systems which can sense changes in the surrounding environment and respond by changing its physico-chemical properties, thereby modulating drug release profiles[10, 11]. This would help in reducing premature drug release and would maintain effective drug levels at the pathological site[12]. The high-water content coupled with soft texture of NGs enables them to exhibit physical properties which are analogous to that of body tissues [13]. Although NGs were initially studied for their temperature responsive behaviour, other sensitivities such as pH, light, magnetism etc. could be incorporated to make them multifunctional. Combining potential drugs with hybrids of plasmonic NPs and stimuli responsive polymeric gels would lead to efficient release of the drug coupled with prospects in bio-imaging and sensing. A schematic representation of multifunctional NP is shown in Figure 1.1.

One of the widely studied temperature and pH-dependent polymeric NGs which has captured research attention is that of poly(N-isopropylacrylamide-co-acrylic acid) (pNIPAm-AAc) [14-17]. Previous research performed by our group in Ugelstad Laboratory has shown that the size

and physico-chemical properties of these NGs can be modified by altering different parameters in the synthesis process which include monomer-comonomer ratio and concentrations of stabilizer, initiator and cross-linker among others [14]. pNIPAm-AAc NGs coupled with Au NPs have been shown to provide pH and temperature sensitivities in addition to plasmonic attributes of Au NPs [15].

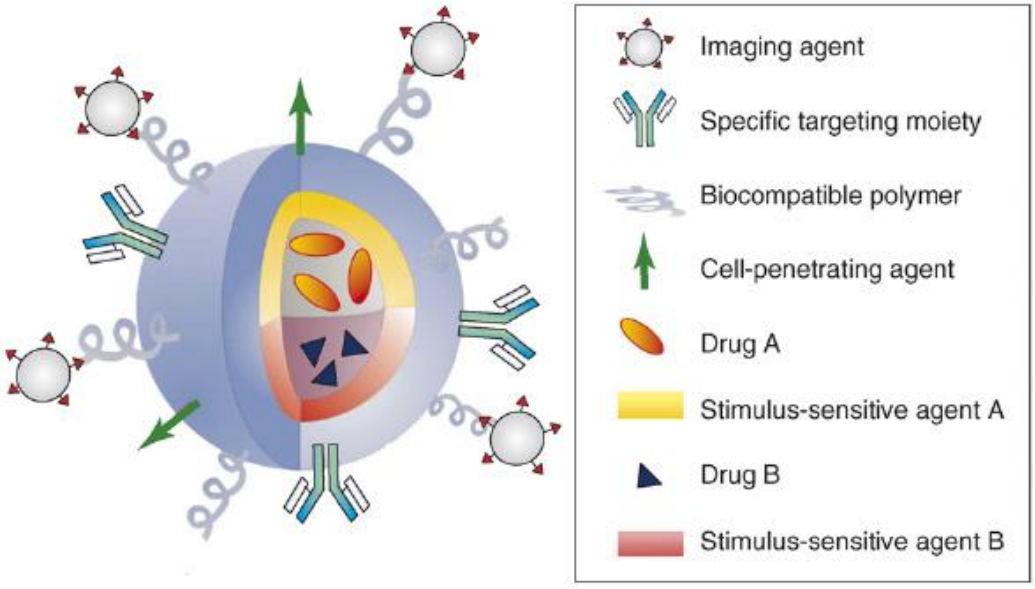

Figure 1.1: Schematic representation of multifunctional NPs [7].

Though enhanced properties of the hybrid have been reported by incorporating NPs in NGs, there has not been a systematic study to understand the effect of constituent NPs on the hybrid. Monitoring the growth of multifunctional NPs and comparing its physico-chemical properties with that of NGs, would help in mapping the effects of constituent NPs on the resulting hybrid. Previous works have been focussed on coating the inorganic NPs with stimuli-responsive NGs post synthesis [15, 18]. Performing in situ[3] synthesis of multifunctional hybrid NPs and comparing their properties with that of coated counterparts will lead to a new class of nanocarriers which could fit specific applications in nanomedicine.

The overall goal of this work was to synthesize and characterize multifunctional NPs of different compositions, understand their growth mechanisms and subsequently use the hybrids for drug delivery studies. In this project, NGs were synthesized via precipitation polymerization using an approach previously reported by our group [19]. Three different molar ratios of reactants were used to obtain NGs with different properties. Inorganic NPs of different sizes and surface charges were incorporated into these NGs via in situ method and a detailed study

[3] NPs added during the synthesis of NGs

of the properties of these novel multifunctional NPs were performed using characterization techniques such as dynamic light scattering (DLS), UV-Vis measurements and S(T)EM. This was followed by time-based studies to monitor the growth of these hybrids. The hybrids were further loaded with a model protein drug, Cytochrome C and the loading and release kinetics from different matrix morphologies were studied. Furthermore, suggestions for future work in this direction have been discussed in the light of the observed properties in order to achieve the overall aim of the project.

2 Literature Review

The enhanced physico-chemical features of NPs, as discussed in the previous section, render them suitable candidates for wide array of applications. Based on composition, NPs can be classified as inorganic, polymer based and hybrid NPs, the latter being synthesized by combining the inorganic and polymeric counterparts. In this chapter, various types of NPs, both inorganic and polymeric, will be discussed based on their physico-chemical properties, synthesis routes and biomedical applications. This will be followed by a discussion on hybrid NPs which possess collective properties of the constituent moieties.

2.1 Inorganic NPs

Inorganic NPs, as the name suggests, are primarily constituted of inorganic materials and can be broadly classified as noble metal NPs, fluorescent NPs and magnetic NPs based on their properties. Most of the inorganic NPs are metals while the other categories include metal oxide NPs and semi-conductor NPs among others. The optical features of noble metal NPs, such as Au and Ag, have made them important candidates in various biomedical applications. Since Au NPs were mainly used in this work, the scope of discussion will be limited to these NPs.

2.1.1 Au NPs

Au NPs have been a topic of intensive research owing to their excellent optical properties, biocompatibility, enhanced stability[2] and low cytotoxicity[20]. This has led to a dramatic increase in the potential applications of Au NPs in fields such as bio-sensing, photothermal applications, targeted drug delivery and catalysis among others. The rich surface chemistry and diverse applications of Au NPs makes it necessary to delve into their physico-chemical properties.

2.1.1.1 Physico-chemical properties of Au NPs

The optical features of Au NPs gives rise to various fascinating properties such as varied colours in aqueous solution, as well as electromagnetic field enhancement effects based on their sizes and shapes [21]. Au NPs exhibit a unique phenomenon called localized surface plasmon resonance (LSPR), which is caused by interaction between the incident light and oscillation of conduction electrons on the surface of the NPs[22]. This occurs as a result of confinement of surface plasmon in a NP which is of a size similar or smaller to the wavelength of light used to excite the plasmon. The conduction electrons on the surface of Au NPs undergo a shift on getting impinged by an electromagnetic wave, which leads to a polarity in the molecule. A

restoring force established in order to cancel the effect of polarization, brings back the plasmon to its equilibrium position. But when the frequency of oscillation of the plasmon becomes equal to the frequency of the incident electromagnetic wave, a resonance effect is observed which results in increased absorption and scattering of light. This phenomenon is termed as LSPR and is responsible for the optical brilliance of these NPs. Figure 2.1 gives a schematic representation of LSPR effect in a metallic NP.

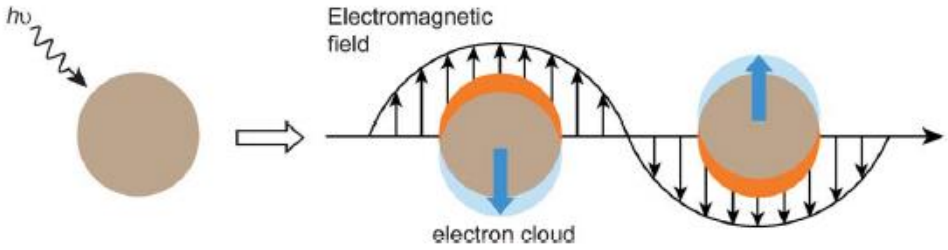

Figure 2.1: Schematic representation of LSPR in a metallic NP [23].

The LSPR wavelengths of Au NPs are greatly influenced by the size and shape of these NPs. For instance, Au nanospheres (Au NSs) possess only a single LSPR peak in comparison to two distinct LSPR peaks for Au nanorods (Au NRs) corresponding to the transverse and longitudinal axes respectively.

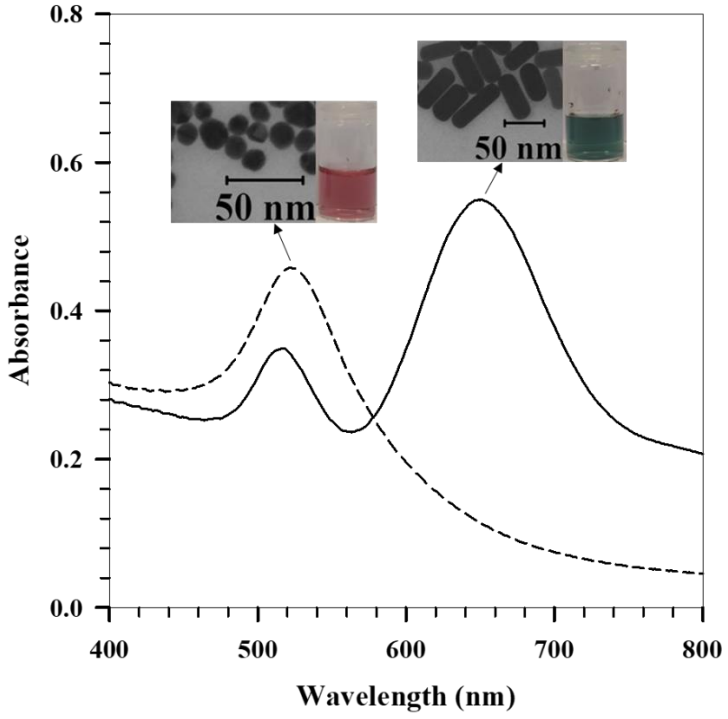

Figure 2.2: UV-Vis spectra of colloidal aqueous solutions of Au NPs. Dashed curve: NS; Solid curve: NR.

The size and shape of these NPs can be tuned to either scatter or absorb more light at the LSPR wavelength, thereby rendering improved bio-medical applications. Figure 2.2 provides a comparative representation of UV-Vis spectra observed for Au NSs and Au NRs. Having discussed the properties of Au NPs and the importance of tuning their morphology, the following section would deal with the synthesis routes for obtaining Au NPs.

2.1.1.2 Synthesis routes for Au NPs

Synthesis of Au NPs can be broadly classified into top-down and bottom-up approaches. Top down approach involves the reduction in size of a bulk of gold, which acts as the starting material, by physical or chemical means. Lithography techniques such as electron-beam lithography (EBL) and focussed ion beam (FIB) lithography are examples of top-down approaches [24]. This approach is associated with limitations which include presence of defects and polydispersity in the final product [25] and hence are used rarely.

Bottom-up approaches have been more commonly used in Au NP synthesis owing to homogeneity and fewer defects in the NPs. This approach involves the growth of NPs via self-assembly of atoms. The NP surface gets constructed atom-by-atom, and the initially formed NPs assemble into final shape under specific controllable thermodynamic conditions for synthesis [25, 26]. Various solution based wet chemical methods have been extensively used in the synthesis of Au NPs through bottom-up approach. Seed mediated growth is one such method that has gained wide popularity in recent years owing to the ease with which specific shapes of Au NPs could be synthesized in high yields, and hence is described in detail in the following section.

2.1.1.2.1 Seed Mediated Growth Method

Seed mediated growth refers to the step by step synthesis of Au NPs in which Au NP seeds are prepared in the first step. The second step involves preparation of growth solution followed by the addition of seeds to it. Hence this makes it easier to control the sizes and shapes of the Au NPs by altering the concentration and nature of additives used in the synthesis. Au seeds (Au^0) which are prepared by reduction of gold precursor in the presence of strong reducing agent such as $NaBH_4$, are added to the growth solution consisting of gold precursor, stabilizing agent and a mild reducing agent. In addition, the growth solution can also contain other additives such as $AgNO_3$ and co-surfactants to improve the shape selectivity of the NPs. The reducing agents used in the second step are mild ones (such as ascorbic acid) which reduce Au^{3+} to Au^0 only in the presence of Au seeds as catalyst [27]. Hexadecyltrimethylammonium bromide (CTAB), a

cationic surfactant, has commonly been used as stabilizing agent in the growth solution, while both CTAB and sodium citrate have been found to observe good stabilizing effects in the seed solution [28]. Figure 2.3 depicts a schematic illustration of the seed-mediated method for growth of Au NPs.

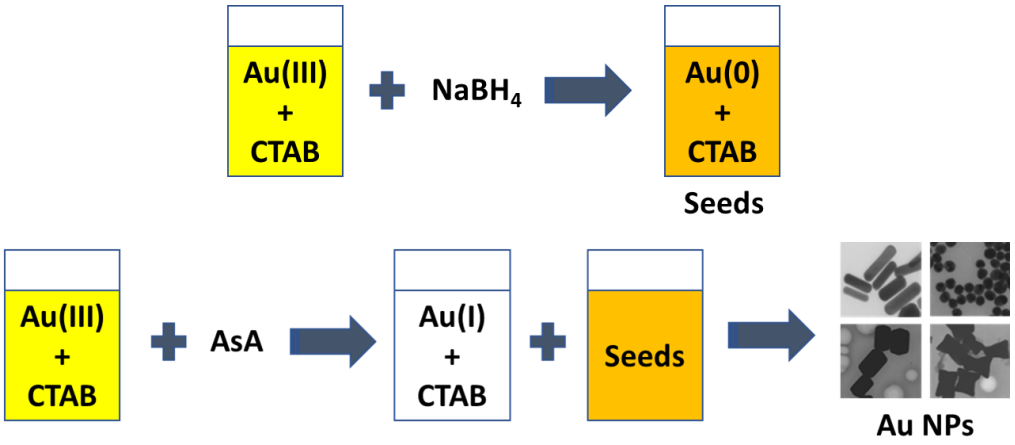

Figure 2.3: Schematic illustration of seed-mediated growth method.

Seed mediated growth method and simple reduction of Au precursor by modified Turkevich method were used in this project for Au NP synthesis and have been reported in Section 3.2.

2.2 Polymer based NPs

Polymer based NPs have attracted research attention in the last few decades owing to their multitude of fascinating properties such as biocompatibility, biodegradability, ease of surface modification, targeting potential, high structural and chemical homogeneity and controlled degradation among others [29]. These properties make them important candidates for drug delivery applications. The particle size and particle size distribution of these NPs are of significant importance as they determine their characteristic properties such as viscosity, surface area and packing density. Based on structure, polymer based NPs can be broadly classified into nanospheres and nanocapsules. Nanospheres refers to homogeneous matrix systems in which the active agent could either be dispersed throughout the polymer matrix or be adsorbed on the surface. On the contrary, nanocapsules are heterogeneous vesicular systems in which the bioactive materials are confined to an inner cavity (aqueous or oily core) which is surrounded by an ultrathin polymeric membrane thus providing better protection of the molecule [30]. Figure 2.4 provides an illustrative image of a drug molecule inside a nanocapsule and nanosphere.

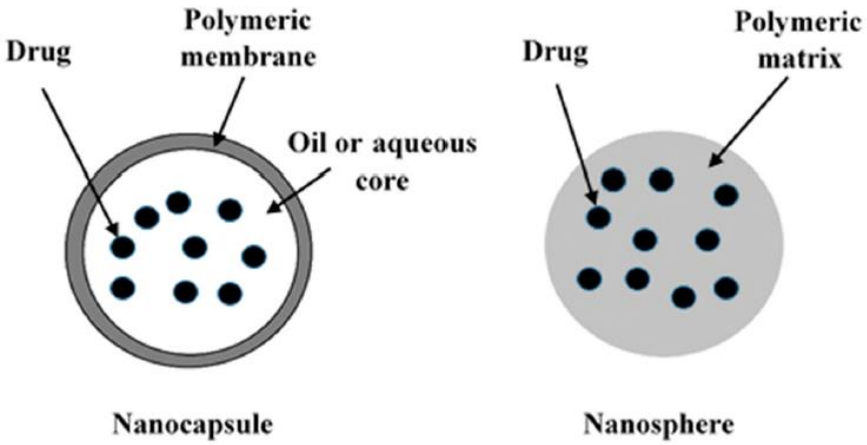

Figure 2.4: Schematic showing the location of drug inside a nanocapsule and nanosphere [31].

Based on the composition, polymer based NPs can be classified into polymeric micelles, dendrimers or hydrogels. Since this work mainly focusses on hybrid NPs prepared using hydrogels, more emphasis will be laid on discussing their properties. However, a brief discussion on the properties of polymeric micelles and dendrimers have also been provided in the following sub-sections.

2.2.1 Polymeric Micelles

Polymeric micelles are formed by the spontaneous self-assembly of individual amphiphilic block co-polymers [32]. This occurs as a result of large solubility difference between the hydrophilic and hydrophobic segments of the polymer. These micelles have a fairly narrow size distribution and have a core-shell architecture, where the hydrophobic segments are segregated from the aqueous exterior to form an inner core surrounded by hydrophilic segments [33]. This enables poorly water-soluble drugs to be incorporated into the inner core, which gets protected from the outer aqueous environment by the outer shell of hydrophilic segments.

2.2.2 Dendrimers

Dendrimers are highly branched three-dimensional structures of synthetic polymers with a layered architecture that display high potential in several biomedical applications. These structures consist of three compartments- the multivalent surface, an outer shell just beneath the surface having a well-defined microenvironment and the core, which is protected from the surroundings, thereby creating a microenvironment surrounded by the dendritic branches [34]. These three parts of the dendrimer can be tailored precisely for the particular applications such as anti-viral drugs, tissue repair scaffolds, targeted drug delivery and optical sensors [35].

Figure 2.5 shows a schematic representation of the structure of a polymeric micelle and a dendrimer.

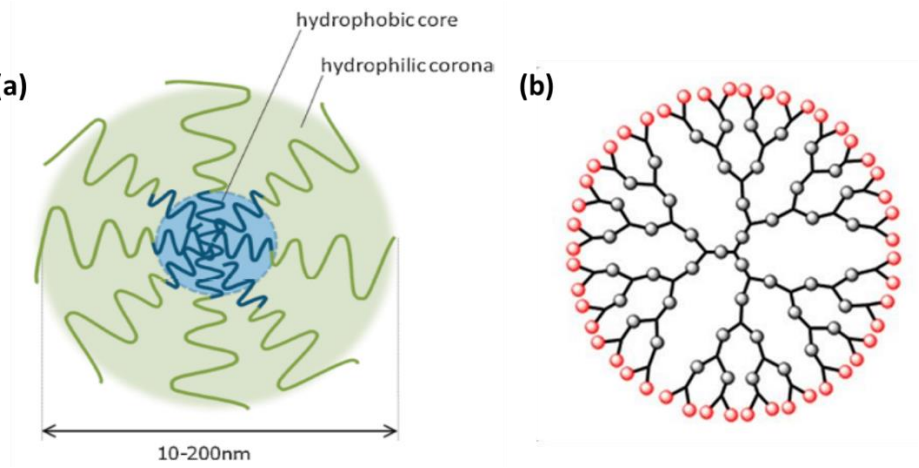

Figure 2.5: Schematic representation of the structure of (a) polymeric micelles [36] (b) dendrimer [37].

2.2.3 Hydrogels

Hydrogels are three-dimensional, cross-linked polymer networks which have high affinity for water. These are composed of a hydrophilic organic polymer and have porous structures which enables water to enter their networks forming swollen structures of hydrogels. Hydrogels in the nano-regime are often termed as nanogels. In this report, both terms have been used interchangeably. The high water content in addition to the soft texture of hydrogels, provides them physical properties that have close resemblance to that of the body tissues, thereby exhibiting excellent biocompatibility[38]. Based on the type of crosslinks, NGs can be classified into physical and chemical hydrogels. While physical cross links occur due to forces such as hydrogen bonding, van der Waals interactions or physical entanglements, chemical cross links are a result of covalent bonds [39].

The most important characteristic of hydrogels arises from their stimuli responsiveness to a wide range of stimuli such as temperature, light, pH, electric and magnetic field and ionic strength among others [40]. The stimuli causes these hydrogel systems to modify their microstructures, phase volume, surface charge or their combination, thereby leading to phase transitions [41, 42] as depicted in Figure 2.6. This response to stimuli is usually reversible, which would revert back the properties of NGs on removal of the stimulus. Due to their ability to sense the fluctuations in their external environment and respond smartly by changing its physico-chemical properties, these polymers are often regarded as “smart polymers” [43]. This has led to breakthrough advances in drug delivery applications where conventional drug

delivery systems such as liposomes, microspheres etc. [44] could be replaced with NGs to provide finer temporal control over drug release, reduced side effects and longer circulation times.

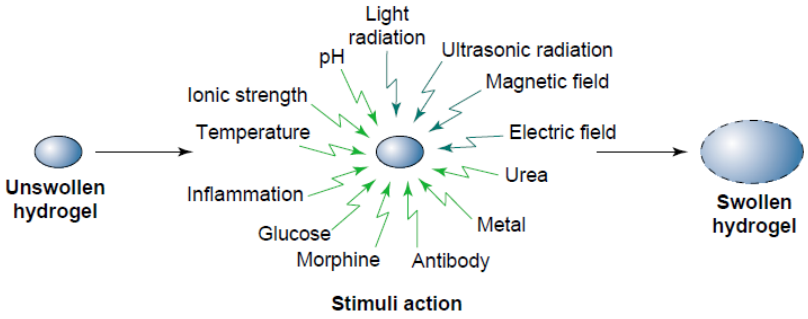

Figure 2.6: Phase transition in a stimuli-sensitive hydrogel [45].

Since this work is primarily concerned with temperature and pH responsive hydrogels, the scope of discussion will be limited to these stimuli.

2.2.3.1 Temperature-sensitive hydrogels

These hydrogels, as the name suggests, undergo transitions in their properties with an alteration in the surrounding temperature. At a critical solution temperature, the homogeneous aqueous solution prepared from these temperature responsive polymers undergo phase transition into a polymer rich and polymer lean phase [10]. This occurs due to variations in the hydrophilic and hydrophobic interactions between polymer chains and the aqueous solvent [46]. The behaviour of a polymer in a solvent is usually governed by solvent -solvent, solvent-polymer and polymer-polymer interactions, often described in terms of the solubility parameter (χ) [34]. The polymer stays in random coil orientation in solvents having $\chi < 0.5$, whereas it collapses into a globule in solvents having $\chi > 0.5$ [47]. This coil to globule transition can occur at two different critical solution temperatures: the lower critical solution temperature (LCST) and upper critical solution temperature (UCST), which can be observed in the phase diagram (Figure 2.7).

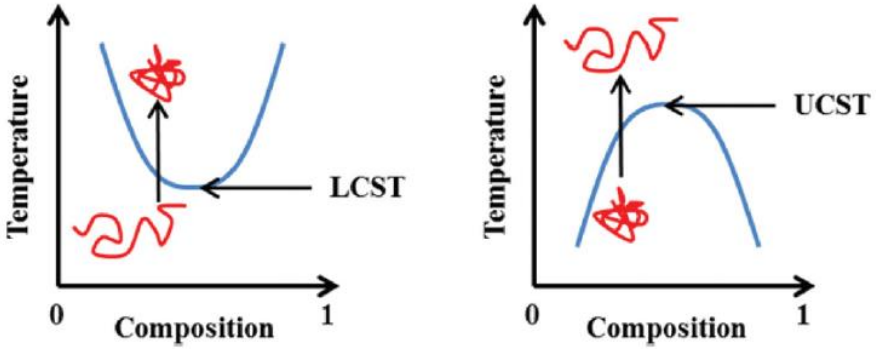

Figure 2.7: Representation of phase transition associated with LCST and UCST [48].

The polymer chains remain in a hydrated random coil state below LCST but shifts to a globular structure on increasing the temperature. On the other hand, polymers possessing UCST, exist in phase separated state below the critical solution temperature and acquires monophasic form on increasing the temperature [10].

One of the most widely investigated thermo-responsive polymers is pNIPAm, which has found potential in various biomedical applications [14, 15, 49]. pNIPAm forms hydrogen bonds with water through the amide side chains of the polymer. However, polymer-polymer hydrophobic interactions also take place due to the presence of isopropyl groups on the side chain, which induce hydrophobic structuring of the water molecules (Figure 2.8) [50, 51]. Below the LCST of pNIPAm (~32°C), the solvent-polymer interactions are stronger than the polymer-polymer interactions. Higher temperatures lead to breaking of the hydrogen bonds followed by the release of bound and structured water. In this case the polymer-polymer hydrophobic interactions become stronger than the polymer-solvent interactions, leading to the formation of a collapsed globular confirmation of the polymer [50].

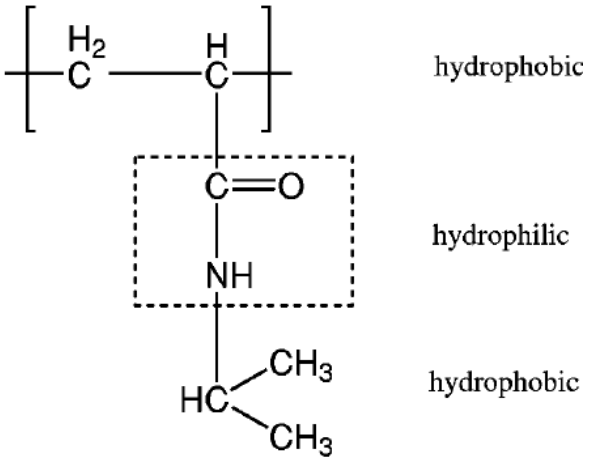

Figure 2.8: Chemical structure of pNIPAm indicating hydrophobic and hydrophilic regions [52].

Similar to homopolymers, in case of cross-linked hydrogels, phase transition occurs at a temperature referred to as volume phase transition temperature (VPTT). Even though LCST and VPTT are defined as single temperatures, actual phase transition of these polymers happen over a range of temperatures owing to varying crystalline and amorphous domains in the polymer, polydispersity, branching and side chains among other factors [53]. The method used to estimate the VPTT in this work has been discussed in Section 3.2.11.2.

The most common technique which has been used in the synthesis of thermo-responsive NGs is precipitation polymerization [50] (Figure 2.9). This method proceeds via homogeneous nucleation at a temperature above the LCST of the polymer. The high temperature would aid

in forming initiator free radicals which initiate the polymerization. These free radicals then attack the monomer leading to radical propagation and chain growth. On reaching a critical length, the polymer chain collapses on itself producing precursor particles. This occurs since the polymerization temperature is maintained above the LCST of the polymer. The precursor particles further grow by aggregation with other precursor particles, by capturing growing oligo radicals and by monomer addition [50].The advantage of this method lies in the ease with which it can produce particles with a very narrow size distribution.

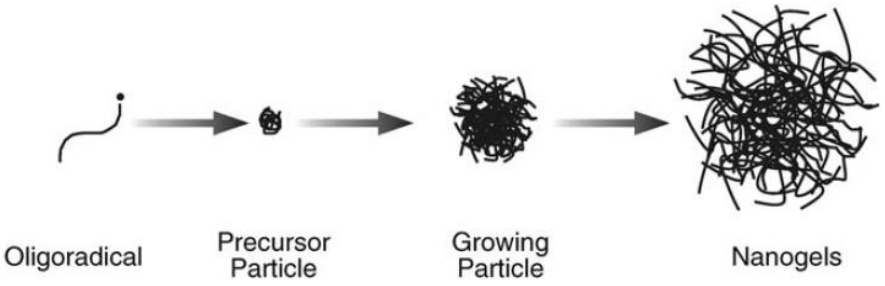

Figure 2.9: Precipitation polymerization in thermo-sensitive NGs [50].

2.2.3.2 pH-sensitive hydrogels

Fluctuations in pH are known to occur at several body sites such as gastro-intestinal tract [54], blood vessels and also locally in certain pathological sites [45]. pH-sensitive hydrogels, as self-evident from their name, refers to a class of hydrogels that undergo an alteration in their structure and inherent properties in response to a change in the pH of the surrounding medium. These polymers are polyelectrolytes and are generally composed of weakly acidic or basic moieties. On encountering a variation in the environmental pH, these polymers would lead to dissociation or association of hydrogen ions based on the pH-dependence of its acidic or basic pendant groups [10].

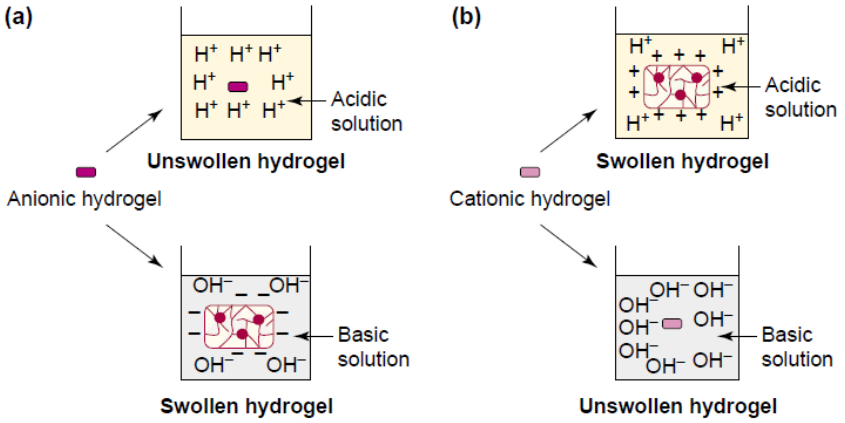

Figure 2.10: pH-responsive swelling/collapse behaviour of (a) anionic and (b) cationic hydrogels [45].

The key factors that influence the degree of swelling or collapse of these hydrogels include the properties of the hydrogel (charge, concentration and pK_a of the ionizable group, degree of ionization, cross-link density and hydrophilicity or hydrophobicity) and properties of the swelling medium (pH, ionic strength and the counterion and its valency) [45, 55] In aqueous solutions, the pendant groups ionize and develop fixed charges on the polymeric network, thereby leading to electrostatic repulsive forces responsible for pH-dependent swelling or collapse of the hydrogel. Anionic hydrogels have their pendant groups un-ionized below the pK_a of the polymeric network. Above pK_a, these groups ionize, leading to swelling of the hydrogel due to large osmotic swelling force due to the presence of ions. A reverse trend is followed in case of cationic hydrogels which swell at lower pH [45]. Figure 2.10 gives a schematic of differential swelling and de-swelling behaviour of ionic hydrogels in acidic and basic buffer solutions.

Multiple stimuli responsiveness can be incorporated into NGs by combining polymers with different stimuli sensitivities, thus providing them multiple phase transition behaviour. One of the extensively studied temperature and pH responsive hydrogel is that of pNIPAm-AAc. These hydrogels undergo a collapse with decrease in pH and swell up on increasing pH. As discussed above, this occurs as a result of de-protonation of the weak carboxylic group of AAc in basic conditions, while at low pH the carboxylic group remains in the associated state [56].

2.3 Hybrid NPs

Hybrid NPs, as the name suggests, refer to a class of NPs that are formed by incorporating more than one distinct NP into a single construct, thereby providing multifunctionality stemming from the different counterparts. These hybrids are highly suitable for theranostic applications, where one of the constituent NP could facilitate diagnostics, while others would aid in curing and therapy [46]. These hybrids can be formed with inorganic NPs, polymer-based NPs or a combination of both. Combinations of these NPs can give rise to various structural geometries of the hybrid such as core-shell NPs, dumbbell shaped or Janus NPs, alloy NPs or self-assembled NPs [34].

Sailor, M.J. et al. [57] had suggested two different design strategies for describing the structure of these hybrid NPs. The nanocomponents constituting the hybrid can be classified as structural and functional based on their properties. The structural nanocomponents include NGs, micelles, liposomes or Au nanoshells, and deliver therapeutic functionality to the hybrid. The functional nanocomponents which include Au NPs, magnetic NPs or quantum dots which would impart

diagnostic features to the hybrid, can either be incorporated into the inner space of a structural nanocomponent, or can be equipped on its surface. A schematic illustration of these design strategies has been shown in Figure 2.11.

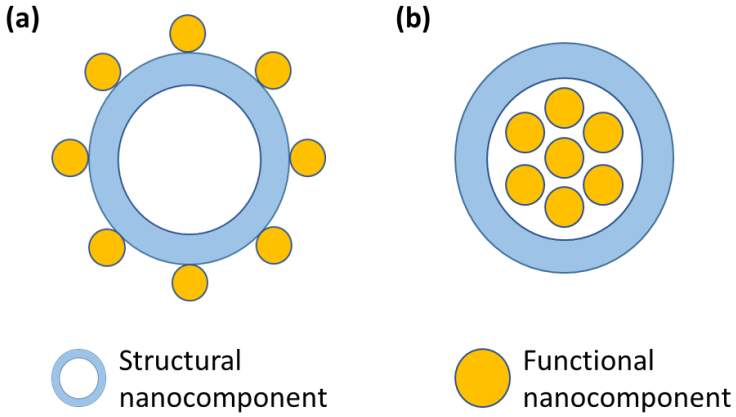

Figure 2.11: Design strategies for different hybrid NPs based on location of functional nanocomponent; Functional nanocomponent located (a) at the surface, and (b) within the structural nanocomponent .

2.4 Synthesis of multifunctional NPs

The synthesis of multifunctional NPs can be done either in-situ or post-synthesis, in which the second component is grown on top of the pre-formed first component. Various techniques have been established for the synthesis of different multifunctional NPs. Few of these are discussed in the following sub-sections.

2.4.1 Solution based reduction of metal precursor

This method is most commonly applied for the synthesis of multifunctional NPs with inorganic core and shell. It involves the initial reduction of a metallic precursor to form the core. The shell is later grown on top of the core NP by the reduction of second metal precursor. The core NP would serve as nucleation sites for the growth of the shell. Fe@Au NPs which consist of Fe core and Au shell is one such example [58].

2.4.2 Reverse micellar template

This method involves reverse micelles, which act as nanoreactors in the synthesis of metallic NPs. This method can be described by a metallic precursor and reducing agent being present in two different reverse micelles. The aqueous core of the reverse micelles would provide a nanoscale reaction medium with controlled volume [59]. The reverse micelles when subject to Brownian motion, collapse and mixing of aqueous contents leads to the formation of core

metallic NPs (Figure 2.12). This is followed by the addition of second metallic precursor and reducing agent which would impart bifunctionality to the NP.

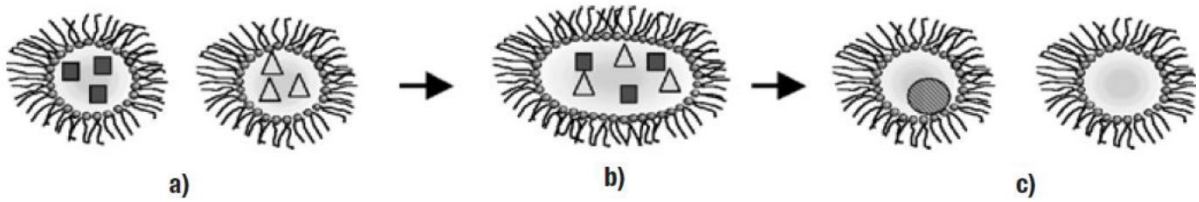

Figure 2.12: Schematic illustration of reverse micellar synthesis (a) reverse micelles containing metal precursor and reducing agent subject to Brownian motion (b) Fusion of cores followed by reaction (c) Formation of metal NP [59].

2.4.3 Precipitation polymerization

Precipitation polymerization is commonly applied for the synthesis of multifunctional hydrogels [50]. For instance, synthesis of pNIPAm-AAc hydrogel proceeds via this technique. In this method, the reaction is maintained at a temperature higher than the LCST of pNIPAm, causing pNIPAm to collapse and form the inner core. These then act as nuclei for the growth of outer shell consisting of AAc units. The mechanism of precipitation polymerization has been discussed in Section 2.2.3.1.

2.5 Recent advances on multifunctional NPs

As discussed in the previous sections, multifunctional NPs are being actively investigated as the next generation of NPs in the biomedical field, which would help in facilitating personalized and tailored treatment of numerous diseases [29]. This section highlights recent advancements and applications that have been reported with regards to multifunctional NPs formed by inorganic NPs, polymer based NPs and a combination of both.

2.5.1 Inorganic multifunctional NPs

This section would primarily focus on various synthesis routes and applications that have been reported for inorganic multifunctional NPs consisting of Au and Fe counterparts. Based on the method used, different shapes of multifunctional NPs have been reported which are found to have specific applications in biomedicine.

Bandyopadhyay et al. had developed a novel method to synthesize highly stable, monodisperse Fe@Au core-shell multifunctional NPs which exhibit magneto-plasmonic characteristics [60]. Iron oxide NPs have found applications in various fields such as drug delivery, magnetic cell sorting, MRI (magnetic resonance imaging) etc. [61, 62] owing to their unique properties of superparamagnetism [63]. One drawback of iron oxide NPs is their high tendency to aggregate

[64]. This can be overcome by surface modification of these NPs with noble metals and polymer ligands which would prevent them from aggregating, thus imparting stability [65]. In this work, Au NPs were coupled with the magnetic NPs to provide additional functionality stemming from the LSPR properties, chemical stability, low cytotoxicity and biocompatibility.

The control over size of the resultant multifunctional core-shell NPs is very important as it has a pronounced effect on the toxicity and mode of administration [60]. Effective control of the crystalline Au shell thickness was reported in this study by varying the Au precursor concentration. Fe NPs were initially synthesized via thermal decomposition of iron pentacarbonyl ($Fe(CO)_5$) in the presence of oleylamine. These NPs were then transferred to an aqueous phase, and a thin coating of Au was obtained over the presynthesized Fe NPs via reduction of Au salt in the presence of sodium citrate. The Fe NPs would act as heterogeneous nucleation sites and would lead to the formation of a continuous shell of Au. These NPs were further functionalized with thiolated polyethylene glycol (PEG-SH) molecules and then tested for toxicity by performing in vitro cellular interactions on two different cell types. PEG shell on the surface of NPs have been reported to enhance biocompatibility and provide stealth properties to the NPs [66]. A schematic showing the sequence of steps involved in the synthesis of PEG modified Fe@Au NPs is shown in Figure 2.13.

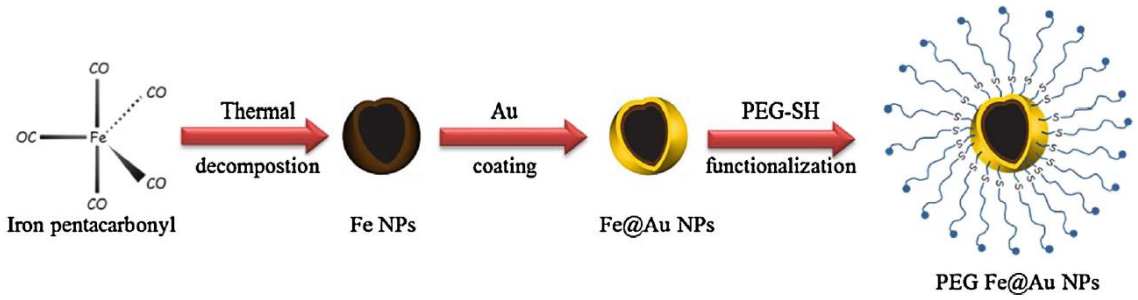

Figure 2.13: Schematic showing sequence of synthesis of PEG modified Fe@Au NPs [60].

Results obtained from Energy Dispersive X-Ray Spectroscopy (EDX) and X-Ray photoelectron spectroscopy (XPS) confirmed the presence of Au coating around Fe NPs. A bathochromic[4] shift observed in the absorbance peak for PEG coated Fe@Au NPs from UV-Vis spectroscopy, indicated an increase in size of the NPs following PEG coating. Increasing Au precursor concentrations also demonstrated a bathochromic shift indicating thicker Au coating on the surface. Fe NPs, which were reported to retain substantial magnetic properties even after Au

[4] shift to longer wavelength

coating, coupled with non-toxicity of the NPs on either cell type, makes them ideal candidates for theranostic applications.

Synthesis of dumbbell-like bifunctional Au-Fe_3O_4 NPs have also been reported by the decomposition of $Fe(CO)_5$ on the surface of Au NPs [67]. In this study, 1-octadecene was used as the solvent and the decomposition reaction was carried out in the presence of oleic acid and oleylamine, followed by room-temperature oxidation under air, as illustrated in Figure 2.14 [67]. The dumbbell-like multifunctional NPs synthesized were reported to have several advantages over the traditional bifunctional systems such as their direct solution phase synthesis without any pre-treatment of particle surface, size-tunability of individual NPs up to 20 nm, and further conversion of Au-Fe_3O_4 to Au-Fe_2O_3 or Au-Fe leading to wide range of properties.

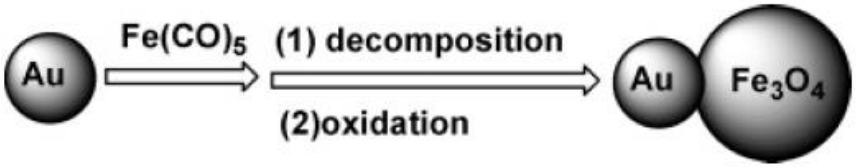

Figure 2.14: Schematic illustration of the growth of Au-Fe_3O_4 dumbbell-like NPs [67].

The Au NPs were synthesized by in-situ injection of $HAuCl_4$ solution into the reaction mixture. The size of the Au NPs could be tuned by adjusting the temperature at which $HAuCl_4$ was injected, or by controlling $HAuCl_4$/oleylamine ratio. On the other hand, Fe_3O_4 NP sizes were controlled by adjusting the ratio between $Fe(CO)_5$ and Au. The dumbbell-like Au-Fe_3O_4 composite NPs showed red-shift of the Au LSPR peak which was attributed to the charge variation of Au NPs within the dumbbell structure. Previous studies which have reported a red-shift associated with electron deficiency on the Au NPs [2], indicate that nanocontact of Au with Fe_3O_4 would lead to deficient electron population on Au.

The interface communication between the nanoscale Au and Fe_3O_4 also leads to change of magnetization behaviours of the Fe_3O_4 NPs. The dumbbell shape of the NPs was reported to be a result of epitaxial growth of iron oxide on the Au seeds, and a change in polarity of the solvent was reported to give rise to new shapes of bifunctional NPs.

A narrow particle size distribution is of prime importance in biomedical applications [68]. Performing synthesis of multifunctional NPs in conditions of a restricted environment, such as that of water-in oil micro emulsions would provide narrow size distribution of the particles. One such synthesis of core-shell Fe@Au NPs was performed by Jafari, T., et al. [69] by reverse micelle method (described in Section 2.4.2). Ultrafine Fe NPs (9-16 nm) with a thin gold layer of about 2 nm thickness were synthesized using this method. Previous studies show that the

size of NPs have a significant effect on their magnetic properties [70]. Since the tiny droplets of water in reverse micelles act as micro-reactors, the size of NPs obtained are dependent on the size of these droplets. Increasing the water to surfactant molar ratio was observed to show an increase in the size and size distribution of the multifunctional NPs. This was a result of increased size of nano-reactors with decreasing amounts of surfactant due to higher surface tension between the water and oil phase [71]. The Fe@Au NPs were coated with poly-glycerol by initially capping with thiol followed by polymerization of glycidol. This was done to prevent the destabilization of NPs due to adsorption of plasma proteins and also to prevent its nonspecific uptake by the reticulo-endothelial system (RES) [72]. The Fe@Au NPs were found to exhibit superparamagnetic behaviour and good biocompatibility at low concentrations, thus making them ideal candidates for biomedical applications.

A recent study conducted by Sood, A., et al. involved the synthesis of multifunctional gold coated iron oxide core-shell NPs [73]. To prevent the elimination of these core-shell NPs by RES, these were further stabilized by attaching thiolated sodium alginate (SA) to the surface of the NPs. High affinity of thiols towards gold leads to formation of strong bonds with the gold surface. Figure 2.15 shows a schematic of the stability imparted to the core-shell NPs with the incorporation of SA polymers.

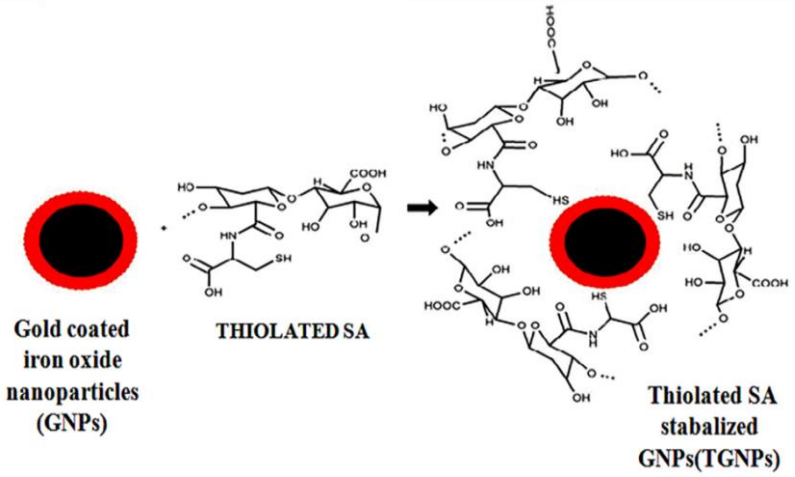

Figure 2.15: Stabilization of gold coated iron oxide NPs using thiolated SA [73].

X-ray diffraction (XRD) studies performed showed a reduction in the peak intensity of iron oxide, which indicated a coating of gold shell on the surface. EDX analysis showed peaks for Fe, O, Au and S which confirmed presence of Au and iron oxide in the sample as well as successful attachment of SA to the surface. The LSPR band corresponding to Au shell in the multifunctional hybrid was observed at a wavelength of 544 nm in comparison to pure Au NP peak at 518 nm and was also found to be broader. This shift in wavelength was reported to be

a result of plasmonic interactions of aggregated particles. Au shells normally have a broader LSPR band when compared to solid Au NPs [73]. Hence the broader peak in UV-Vis confirmed the existence of Au shell on iron oxide surface.

Curcumin, an anti-cancer drug with low aqueous solubility was encapsulated in this system. Loading curcumin in the thiolated SA stabilized nanocomposite system was found to improve the bioavailability of the drug. The loading and encapsulation efficiencies were reported to be 7.2 wt % and 72.8 % respectively. 99% of curcumin was reported to release in a duration of 72 hours confirming controlled release of the drug.

2.5.2 Polymer based multifunctional NPs

In a very recent study, Prasannan, A., et al.[74] had proposed the use of pNIPAm based thermo-responsive hydrogels in ophthalmic drug delivery. The hydrogels were synthesized by mixing poly(acrylic acid-graft-N-isopropylacrylamide) (pAAc-graft-pNIPAm) with pAAc-co-pNIPAm gel. Epinephrine was then incorporated in the hydrogels to study its in vitro drug release profile. pAAc-graft-pNIPAm was reported to show faster release kinetics while the mixture of pAAc-graft-pNIPAm and pAAc-co-pNIPAm gel displayed a more sustained release profile. The results indicated crosslinking density of the polymer to control the kinetics of drug release.

In another interesting study, smart composite hydrogels were synthesized by physically embedding chitosan (CS) microspheres within a thermo-responsive hydrogel based on poly(N-isopropylacrylamide-co-hydroxyethylacrylamide) copolymer [75]. This was then used to study the loading and release profiles of salicylic acid (SA), taken as model drug. CS microspheres display pH-sensitivity and also has the capacity to electrostatically bind to the oppositely charged SA. The cross-linking degree of the hydrogel was reported to play a major role in governing the swelling ratios and sharpness of phase transition. The thermo-responsive polymer network was reported to provide protection of CS microspheres from degradation.

Understanding the polymerization kinetics of multifunctional NPs would provide better insight into the mechanism of growth of these NPs. One such study was performed by Chen, S., et al., who studied the polymerization kinetics in the synthesis of pNIPAm using UV-Vis spectrophotometer [76]. pNIPAm was synthesized via soap-free emulsion polymerization using an oil-soluble initiator- 2,2'-azobisobutyronitrile (AIBN) and a water-soluble initiator-potassium persulfate (KPS). AIBN-initiated polymeric NGs were reported to have different thermal responses when compared to the one initiated by water soluble initiators, thus making

it possible to modulate the LCST of the polymer by varying the type of initiator. The absorbance peak of NIPAm at 220 nm was considered for the kinetic studies which gave a measure of residual monomer concentration after polymerization. The advantage of this method over conventional gravimetric methods to study kinetics lies in that it requires less volumes of reaction solution and very low monomer contents (≤ 0.2 wt% based on water) [76].

Initially, a calibration curve of NIPAm was obtained by measuring its UV-absorbance spectra at known concentrations. pNIPAm samples at different polymerization times were diluted, followed by measurement of its UV-absorbance. The residual NIPAm monomer concentration could be obtained by correlating the absorbance peak at 220 nm of the pNIPAm samples with the calibration curve. As shown in Figure 2.16, NIPAm possess two absorption bands, one at 198.6 nm (primarily contributed by ─C═O) and at 220 nm (mainly contributed by ─C═C).

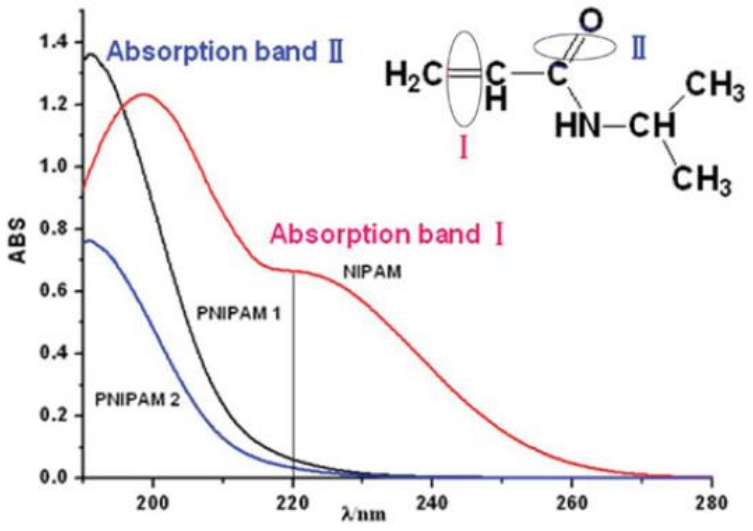

Figure 2.16: UV-Vis absorbance spectra of NIPAm and pNIPAm [76].

As polymerization proceeds, the ─C═C bonds change to ─C─C which would result in a gradual decrease in the absorption band at 220 nm, as can be observed from the UV-Vis absorbance spectra of pNIPAm in Figure 2.17. This decrement in absorbance was observed till the polymerization reached equilibrium and was used to get the residual NIPAm concentration and thereby obtaining the polymerization kinetic curves. The KPS-initiated polymerization was reported to have a shorter induction time, while the AIBN initiated reaction had a slower initial rate but had a higher rate in the later stages of polymerization. Dynamic light scattering (DLS) and Gel permeation chromatography (GPC) were used to examine the change in hydrodynamic size, size distribution and molecular weight during the reaction process. Using this information, reaction mechanisms were suggested for polymerization based on the different initiators.

However, the discussion on reaction mechanisms would be limited to the one initiated with KPS as it has been used as initiator in this thesis.

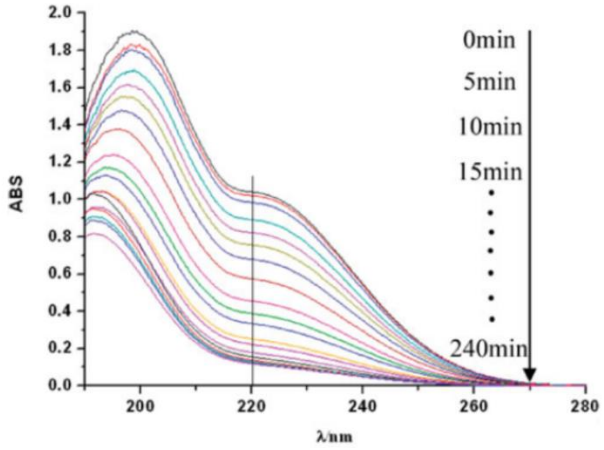

Figure 2.17: UV-Vis absorption spectra of pNIPAm during polymerization initiated by KPS [76].

Results from DLS indicated a slight increase in the size of hydrogels from 170 nm to 190~200 nm during the whole reaction, and the size distribution was observed to get wider with increasing polymerization time. The initial stage had NIPAm dissolved in aqueous solution to which KPS (also in aqueous phase) was added. KPS then decomposed to active free radicals and initiated the NIPAm monomers, which led to the formation of oligomers with hydrophilic end groups. The reaction temperature being far above the LCST of PNIPAm would cause the polymer chains to separate out from aqueous phase and coil, forming the primary particles of 170 nm. The charged hydrophilic persulfate radical ($-SO_4^-$) was reported to play the role of surfactant and thereby stabilize the primary particles. With increasing time, subsequent reactions would happen in the primary particles. New primary particles were reported to form even at increased reaction times which could explain the wider size distribution.

Though this study was performed to analyse the polymerization mechansim for PNIPAm hydrogels, expanding this study by using multifunctional hydrogels such as that of PNIPAm-AAc would provide better understanding of the underlying mechanism.

2.5.3 Hybrid multifunctional NPs

Studies performed by Bandyopadhyay, S., et al.[14] have incorporated Fe@Au NPs into multiresponsive pNIPAM-AAc NGs, thereby providing magneto-plasmonic properties in addition to temperature and pH responsiveness. The NPs were incorporated in the NGs using coating method and in situ growth. These hybrids were subsequently loaded with Cyt C by using a modified breathing-in mechanism. Cyt C is a small protein complex which is loosely

associated with the inner membrane of mitochondria. It is highly water-soluble which makes it advantageous to absorb on hydrogel matrices.

The swelling-collapse properties of the in situ grown hybrid NPs resembled that of the bare NGs, while the coated hybrids resembled the properties of bare Fe@Au NPs. The volume increase observed in case of NG coated Fe@Au NPs at 40°C was reported to be a result of cross-linking effect of NPs which pull together the already collapsed NG blocks. The hybrids were reported to show high loading (~96%) and encapsulation of Cytochrome C and highest release kinetics were observed at 40°C and pH 3.2, with maximum release from Fe@Au coated NGs.

A magnetic thermo-responsive hydrogel which changes phase upon magnetic stimulation near physiological temperatures (around 34°C) has been reported by Crippa, F., et al. [77]. These multifunctional NPs were prepared by embedding superparamagnetic iron oxide NPs into thermosensitive pNIPAm hydrogels. These nanocomposite substrates were reported to show cyclical swelling/de-swelling behaviour on actuating by an alternating magnetic field. Additionally, these hybrid NPs displayed no cytotoxicity on fibroblast cells, thus providing them biocompatibility and making them promising candidates as dynamic cellular substrates.

As discussed in Section 2.1.1.1 , anisotropic Au NPs play an inevitable role in biomedical applications, since its plasmon absorption can be shifted between visible and near infrared regions by tuning the size and shape of the NPs. Studies conducted by Bandyopadhyay, S., et al. [15] had made use of such anisotropic NPs to harness their properties in multifunctional hybrids. Nanorods, tetrahexahedral, bipyramids, nanomakura[5] and nanospheres of Au were coated with polyethylene glycol (PEG) followed by pNIPAm-AAc hydrogel. PEG coating was reported to aid in reducing the cationic charge induced by CTAB on the NPs, thus reducing their cytotoxicity. In addition to that, it also offers stealth properties to Au NPs owing to its hydrophilic nature, thereby protecting the NPs from the external environment [78]. pNIPAm-AAc hydrogels displayed stimuli-responsive properties, rendering multifunctional characteristics to the hybrid. Loading and release studies on these hybrid NPs performed with Cyt C showed higher release profiles for larger sizes of PEG-hydrogel-coated Au NPs. The shape, size and concentration of Au NPs along with hydrogel content were reported to influence the loading and release kinetics.

[5] pillow-shaped NP

These examples of multifunctional NPs in biomedical applications showcase the potential of these hybrid NPs in facilitating new opportunities for controlled drug release, hence emphasizing the need for understanding their growth and physico-chemical properties.

3 Material and Methods

3.1 Materials

3.1.1 Chemicals used

The following chemicals were used for the synthesis of NGs and Au NSs. The provider name has been listed alongside the chemical name.

3.1.1.1 Synthesis of NGs

- Sodium dodecyl sulphate (SDS), Sigma-Aldrich
- N-Isopropylacrylamide (NIPAm), Sigma-Aldrich
- N, N'-Methylenebis(acrylamide) (BIS), Sigma-Aldrich
- Acrylic Acid (AAc), Sigma-Aldrich
- Potassium persulphate (KPS), Sigma-Aldrich

3.1.1.2 Synthesis of Au NSs

- Gold(III) chloride trihydrate ($HAuCl_4.3H_2O$), Sigma-Aldrich
- Sodium citrate dihydrate ($C_6H_5Na_3O_7.2H_2O$), Merck
- Hexadecyltrimethylammonium bromide (CTAB), Fisher Scientific
- Sodium borohydride ($NaBH_4$), Sigma-Aldrich
- Ascorbic acid(AsA), Fluka

Apart from the synthesized Au NSs, silver (Ag) colloid (45 nm hydrodynamic diameter) purchased from BBI solutions were also used in this study. Cytochrome C from bovine heart, used as the model drug, was purchased from Sigma-Aldrich. HCl and NaOH purchased from Merck Millipore and VWR respectively were used for adjusting the pH of solutions wherever required. Cellulose dialysis tubing from Sigma-Aldrich with a MWCO of 14 kDa was used for carrying out dialysis of the NGs as well as for the drug release studies. Distilled de-ionized water (MQ water, resistivity ~ 18.2μΩ.cm @ 25°C) was used for preparing all solutions. Except for NIPAm, all other chemicals were used as received. NIPAm was recrystallized before further use, the steps for which have been described in Section 3.2.2.

3.2 Methods

The synthesis procedure for the synthesis of Au NSs, polymeric NGs and multifunctional hybrid NPs are described in this section. This is followed by a description on various

characterization techniques used in this study. Finally, the procedure used for loading and release studies of the drug are discussed.

3.2.1 Synthesis of Au NSs

Citrate and CTAB coated Au NSs were synthesized to study their effects on incorporating these into polymeric nanogels. Two different sizes of Au NSs were synthesized by the citrate reduction of gold precursor. CTAB coated Au NS was synthesised via seed mediated growth. The synthesis route followed have been discussed in the following sections.

3.2.1.1 Synthesis of citrate coated Au NSs

Au NSs were synthesized by the simple reduction of gold precursor ($HAuCl_4.3H_2O$) by sodium citrate. Different concentrations of precursor were used to obtain different sizes of NSs. In a typical reaction, 10 ml of 10mM sodium citrate solution was heated to 70ºC, to which 10 ml of a known concentration of gold precursor was added dropwise under constant stirring. 0.9 mM and 1.5 mM concentrations of gold precursor were used in this study to obtain samples AuNS1 and AuNS2 respectively. The stirring speed was maintained at 700 rpm and the reaction was stopped after 20 minutes. A schematic of the synthesis process is shown in Figure 3.1.

Figure 3.1: Synthesis of citrate coated Au NS.

The reaction mixture was then centrifuged in a micro-centrifuge (Eppendorf Minispin plus) at 10000 rpm for 10 minutes. The bottom precipitate after centrifuging was re-dispersed in 5 ml of MQ water.

3.2.1.2 Synthesis of CTAB coated Au NSs

Seed mediated growth involving seed and growth solutions was used for the synthesis of CTAB coated Au NS. Citrate coated Au seeds used in this study were synthesized by mixing 0.5 ml of 10 mM $HAuCl_4$ to 0.5 ml of 10 mM Na-citrate solution in a round bottom flask followed by the addition of 18.4 ml of MQ water. To this mixture, 600 µl of ice cold solution of 0.1 M $NaBH_4$ was added under vigorous stirring. After 3 more minutes of stirring, the seed solution was aged for 3 hours at room temperature. Figure 3.2 shows the synthesized citrate coated Au seeds after 3 hours of ageing.

Figure 3.2: Citrate coated Au seed.

The growth solution was prepared by dissolving 1.2 g of CTAB in 15 ml MQ water at 80°C. After the surfactant solution was cooled down to 35ºC, 15 ml of 0.86 mM $HAuCl_4$ solution was added and the mixture was stirred at 750 rpm for 15 minutes. The stirring speed was then increased to 1000 rpm and 135 µl of 128 mM AsA followed by 96 µl of aged seed solution were added and the stirring was stopped immediately. The mixture was left overnight at 35ºC. The sample was then centrifuged at 11000 rpm for 20 minutes in an ultra-centrifuge followed by 14500 rpm for 20 minutes in a micro-centrifuge to remove excess surfactant and smaller NSs. After discarding the supernatant, the NSs were re-dispersed in 5 ml of MQ water. Au NS synthesized using this method will be named Au NS3 in the rest of the report. Figure 3.3 shows a schematic representation of the seed mediated synthesis method.

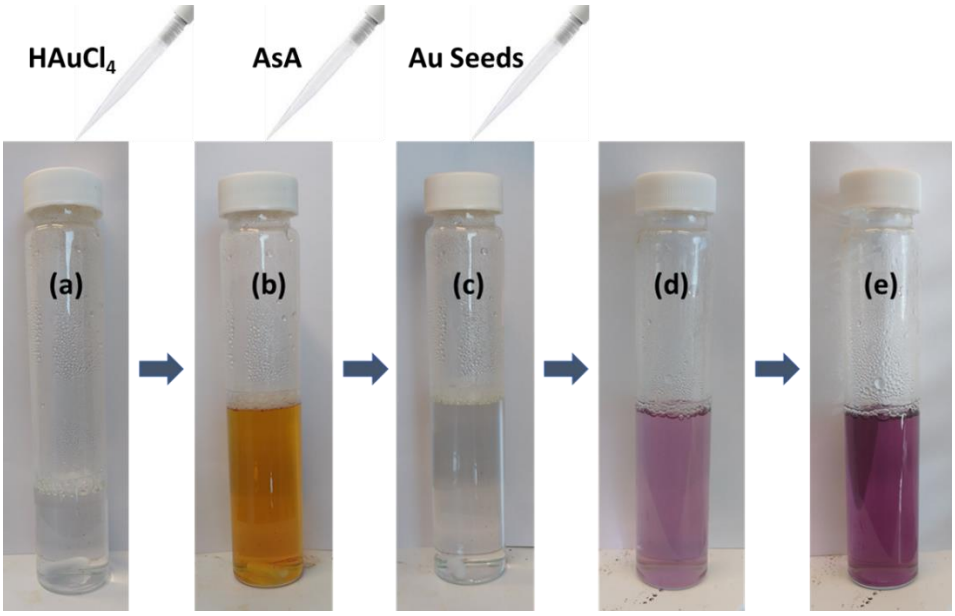

Figure 3.3: Schematic representation of the seed mediated growth (a) CTAB solution (b) after addition of $HAuCl_4$ (c) after adding AsA (d) 5 min after adding the seed (e) 12 hrs from seed addition.

3.2.2 Recrystallization of NIPAm

NIPAm was recrystallized in order to get rid of impurities that could inhibit the polymerization reaction. Figure 3.4 shows the setup used for the recrystallization process. 5 g of NIPAm was taken in a one-necked glass flask and to it 50 ml of n-Hexane was added. The flask was equipped with a water condenser and the reaction was carried out at 110°C for 2 hours. Thereafter, the reaction flask was directly transferred to an ice bath for 30 minutes to allow recrystallization of the purified monomer. The solution was then filtered using Whatman filter paper circles (90mm). It was then kept for drying for 24 hours and was later stored at -20ºC to prevent absorption of moisture. Recrystallization of NIPAm was found to be an important step prior to its use in the synthesis of NGs (Appendix A).

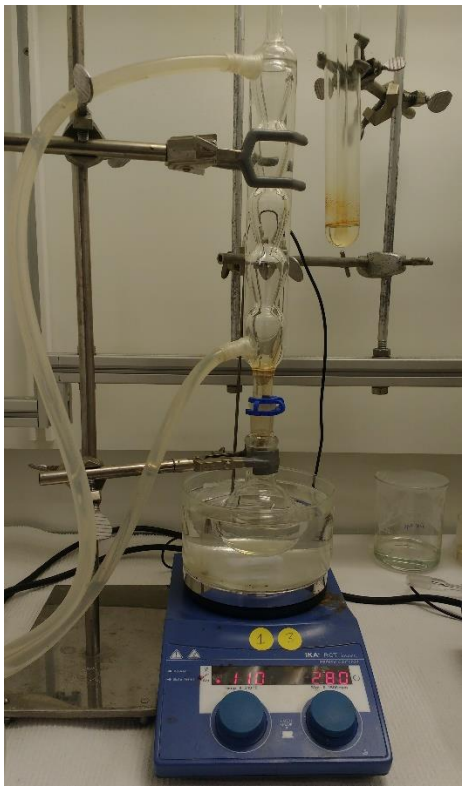

Figure 3.4: Reaction setup for recrystallization.

3.2.3 Synthesis of NGs

Precipitation polymerization was used for synthesizing NGs. The procedure used for the synthesis was developed by Raghunathan, K., et al.[79] and Chakraborty. R., et al.[19]. Three different molar ratios of the monomers were used to obtain NGs of different compositions and properties. Table 3.1 shows the amount of reactants used for a particular mole ratio. The molar ratio in the table corresponds to NIPAm:AAc:BIS where NIPAm and AAc are temperature sensitive and pH sensitive respectively, and BIS functions as the crosslinker. In a typical synthesis process, the measured amounts of NIPAm and BIS were added to a round bottom flask maintained at 70ºC. To this mixture 5 ml of 4.2 mM SDS solution was added and kept stirring for 1 hour.

Sample Mole Ratio	NIPAm (mg)	AAc (µl) (1.46 M)	BIS (mg)	SDS (ml) (4.2mM)	KPS (µl) (103.6mM)
85:10:05	80	57	6.4	5	800
80:15:05	80	91	6.8	5	800
70:25:05	80	175	7.8	5	800

Table 3.1: Different molar ratios of monomers used in NG synthesis

After one hour, the system was purged with nitrogen for 1-2 minutes for ensuring an oxygen free atmosphere before addition of the initiator. Different volumes of the co-monomer, AAc, (as stated in Table 3.1) was added to the reaction mixture followed by 800 µl of freshly prepared 103.6 mM KPS solution. The nitrogen purging was continued for 5 more minutes from the point of addition of KPS and then stopped. The reaction mixture was left for 2 more hours after which the reaction was stopped and the samples were dialysed overnight.

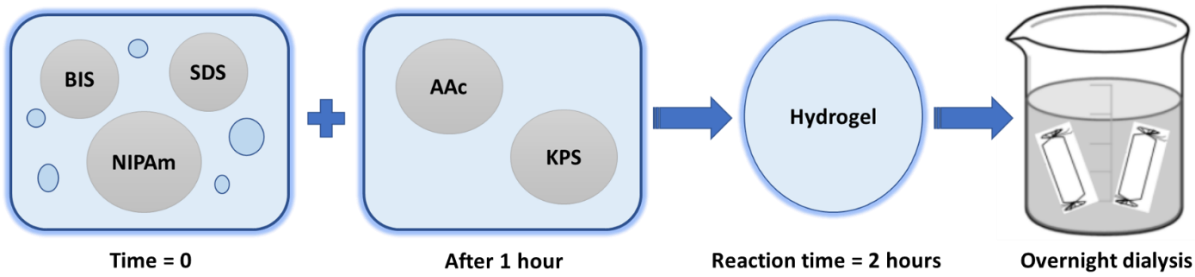

Figure 3.5: Schematic depicting the sequence in NG synthesis.

3.2.4 Synthesis of hybrid NPs

Hybrid NPs were synthesized by in situ method in which Au NSs were added to the reaction mixture during polymerization. The synthesis procedure used was similar to the one discussed in the previous section, the only difference being dispersing the Au NSs in SDS solution before its addition to the mixture. The required concentration of the Au NSs was withdrawn from the stock and spun down in Minispin at 10000 rpm for 10 minutes. The supernatant was discarded, and the bottoms were re-dispersed in 5 ml of SDS solution (Figure 3.6). The reaction setup for the synthesis of hybrid NPs has been shown in Figure 3.7.

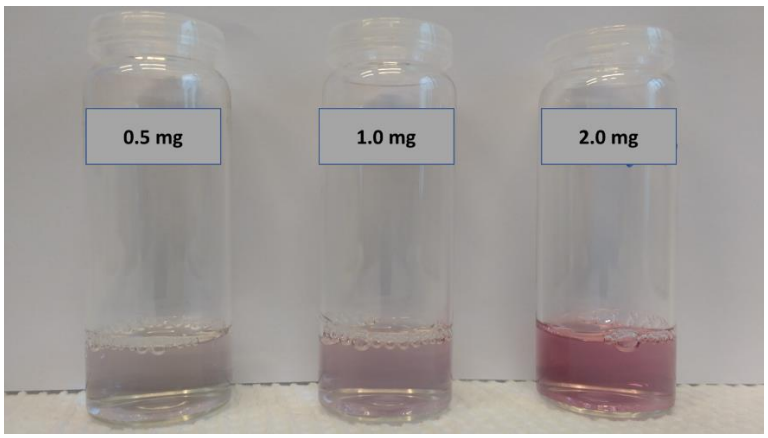

Figure 3.6: Different concentrations of Au NSs re-dispersed in 5ml SDS solution.

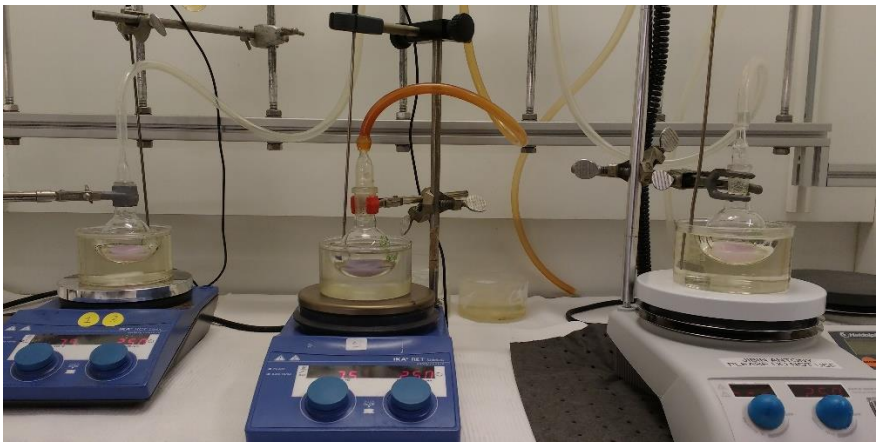

Figure 3.7: Reaction setup for synthesis of hybrid NPs.

3.2.5 Dialysis

Dialysis of the bare NGs and hybrid NPs were conducted to remove unreacted monomers and excess surfactant from the sample. This was done by transferring the samples after completion of reaction into cellulose dialysis tubes which was washed twice in MQ water. The tubes were clipped on both ends and was immersed in MQ water overnight (Figure 3.8).

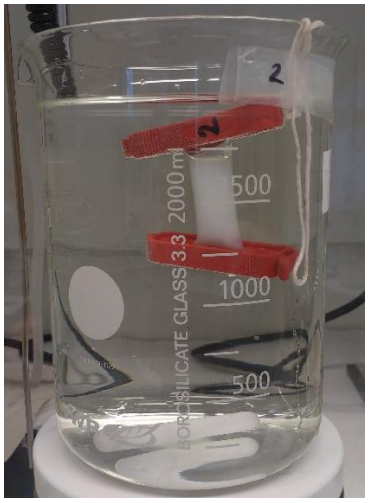

Figure 3.8: NG sample kept for overnight dialysis

3.2.6 Freeze-drying

Freeze-drying refers to dehydration process at low temperatures wherein the sample is first freezed followed by lowering of pressure which would result in removal of ice by sublimation [80]. Both NGs and hybrid NPs were freeze-dried prior to loading and release studies. The samples were transferred into centrifuge tubes and freezed prior to clipping them onto the freeze-drier. A parafilm was placed on the mouth of the tube and holes were pierced on it using a needle. This was done to prevent any contamination to the sample. The samples were then

placed in a glass flask which was attached to one of the inlets of the freeze-drier. VirTis Benchtop Pro freeze-dryer from SP Scientific was used for freeze-drying the samples (Figure 3.9).

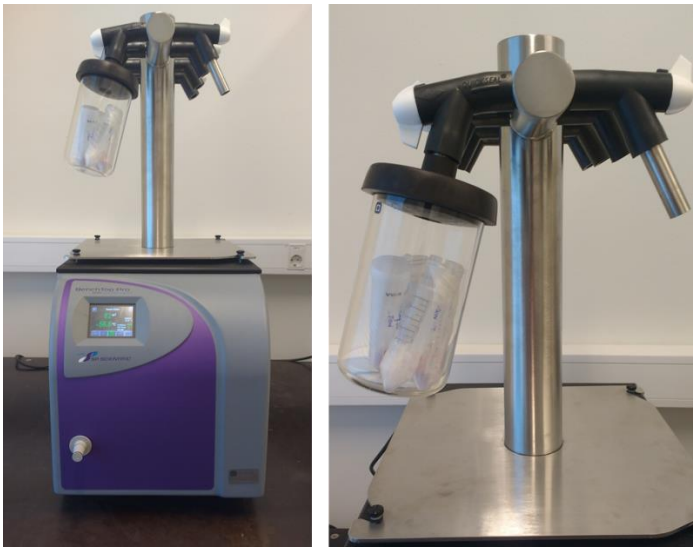

Figure 3.9: Freeze-drying setup used for drying the samples.

3.2.7 Timed Experimental Study

Time based studies were performed to understand the growth of NGs and hybrid NPs during the course of reaction. In this study, a predetermined volume (250 µl) of the reaction mixture was withdrawn at intervals and dropped into 1 ml of ice-cold MQ water to arrest the reaction. This was performed after the addition of AAc and KPS starting from the point a visible colour change is observed in the reaction mixture. The sample withdrawn was replenished with MQ water maintained at reaction temperature (70°C). These samples were then characterized using DLS.

3.2.8 Loading

The model protein drug Cyt C was loaded onto NGs and hybrid NPs using breathing in technique (Figure 3.10) [81]. In this method, a known weight of the freeze-dried NG/hybrid NP is resuspended in an aqueous solution of the drug of known concentration. Loading occurs by absorption of the drug by the lyophilized NG/hybrid NPs as they swell up in the hydrophilic medium.

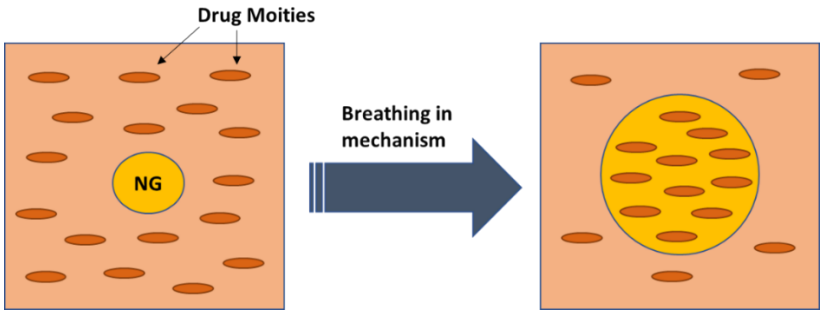

Figure 3.10: Schematic depiction of breathing in technique.

In this study, 1.7 mg of freeze-dried samples were taken in a vial and to this 2 ml of 0.5 mg/ml Cyt C solution was added. The mixture was kept for shaking at 300 rpm for 2 hours which was followed by two different methods to remove free Cyt C. The first method involved dialysis for 24 hours in MQ water, whereas in the second approach, the loaded samples were centrifuged at 14500 rpm for 10 minutes. In case of dialysis, the free cyt C is expected to leave the dialysis tube due to lower molecular weight of the drug compared to the MWCO of the tubing. Centrifuging at a high speed would lead to precipitation of bound drug, thereby making it possible to separate the free Cyt C by removing the supernatant. Figure 3.11 shows NG/hybrid NP samples kept on shaker for loading Cyt C. After successful removal of free Cyt C, these samples were further used for release studies.

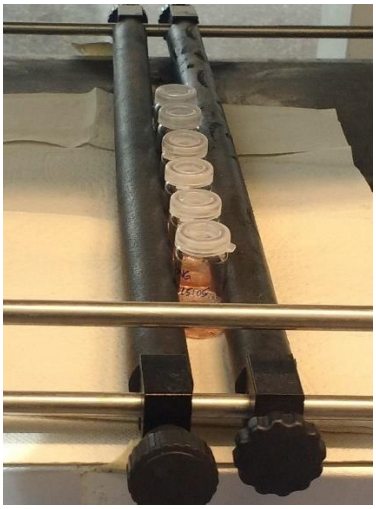

Figure 3.11: Samples kept on shaking for loading Cyt C.

3.2.9 Release Studies

After loading the NGs and hybrid NPs with Cyt C, release studies were performed on these samples at different release conditions. In this study, the precipitate obtained after centrifuging 2 ml of the loaded sample was re-dispersed in the same volume of MQ water followed by further dilution (2.5x times) in order to prevent saturation of the instrument. The Cyt C absorbance

peak of the diluted sample was measured using UV-Vis spectrophotometer before proceeding with dialysis at release conditions. Initial release of the drug was monitored at a low pH 3 which was followed by increasing the temperature of the release medium to 40°C (after a time span of 32 hours) to study the combined effect of stimuli on the samples. The decrease in absorbance peak of Cyt C was measured at various intervals which gave a measure of the drug released as a function of time. Figure 3.12 shows the typical setup of dialysis used for drug release studies.

Figure 3.12: Samples kept on dialysis at release conditions.

3.2.10 Characterization Techniques

3.2.10.1 Dynamic Light Scattering (DLS)

DLS is a characterization technique which can be used to determine the size distribution profile of small particles in suspension or polymers in solution. Light from a monochromatic source, usually a laser is impinged on the sample which is in a state of random motion. This technique works by measuring the rate of particle diffusion via Brownian motion by analysing the rate of fluctuation in the intensity of scattered light [16]. These fluctuations are then auto-correlated in order to estimate the average diffusion coefficient [82]. Substituting the diffusion coefficient in the Stokes-Einstein equation would provide the hydrodynamic diameter of the particle. The expression for Stokes-Einstein equation is given by Equation (1)

$$d_H = \frac{k_B T}{3\pi\eta D} \quad (1)$$

where d_H is the hydrodynamic diameter, k_B is the Boltzmann's constant, T is absolute temperature, η is the solvent viscosity and D is the average diffusion coefficient.

Bigger particles in the sample would move slowly and result in a slow variation in intensity. Smaller particles move quickly and thus leads to quick variations in intensity. Hence DLS provides information about the size distribution of the sample via polydispersity index (PDI). The hydrodynamic sizes of the NPs and NGs were measured using a Malvern Zetasizer Nano-ZS instrument shown in Figure 3.13(a).

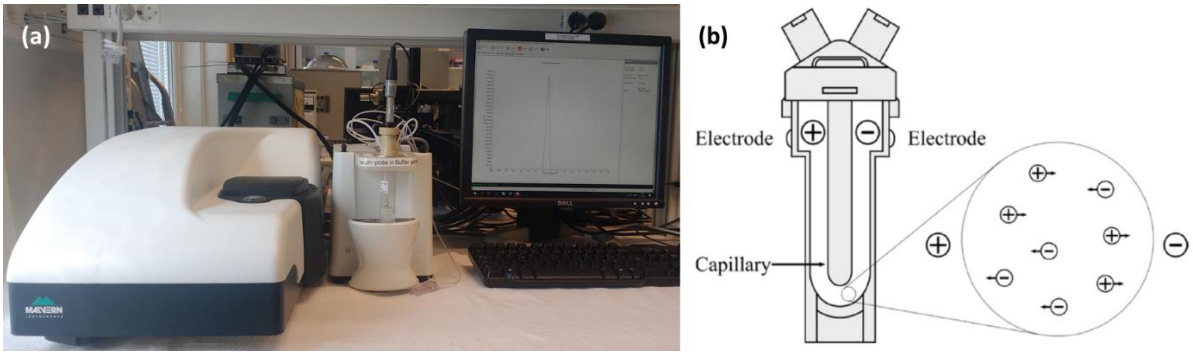

Figure 3.13: (a) Malvern Zetasizer Nano-ZS (b) Folded capillary cell used for the zeta potential measurements [83].

Zeta potential measurements were also obtained using this instrument by measuring how fast the particles move in a liquid in response to an applied electric field. These measurements were used to assess the stability of the samples. A schematic of folded capillary cell used for measuring zeta potential is shown in Figure 3.13(b). For characterizing NGs and hybrid NPs, the temperature of the system was varied from 25°C to 55°C, and then back to 25°C. The effect of this heating and cooling cycles on the sample properties were studied. The NG and hybrid NP properties at different pH were also studied by varying the pH from 3 to 9. This was performed both manually as well as with the help of an auto-titrator shown in Figure 3.14. The auto-titrator consists of a fast response, liquid filled pH probe which measures the pH of the sample and pumps the sample to Zetasizer Nano ZS for measuring the particle size and zeta potential. The pH is adjusted automatically to set intervals by using 0.1 M NaOH and 0.1 M HCl. All measurements were performed in aqueous solutions and an average over triplicate measurements were considered.

Figure 3.14: Auto-titrator for adjusting pH

3.2.10.2 UV-Vis Spectroscopy

UV-Vis spectroscopy was used to measure the amount of ultraviolet or visible radiation absorbed by different inorganic NPs, polymeric NGs and hybrid NPs. This information could be used for detecting the presence of inorganic NPs in the hybrid. UV-Vis spectroscopy is a useful characterization tool to obtain wavelength at maximum absorbance for particles that absorb light in the ultra violet or visible region of the electromagnetic spectrum. The UV-Vis spectra were acquired with a UV-2401PC (Shimadzu) spectrophotometer. Light of particular wavelength is passed through the sample and reference cuvettes via beam separator. The difference in transmitted light intensities from both cuvettes are analysed in the detector and this provides information about the light absorbed by the sample.

This technique is based on the principle of Beer-Lambert's law which states that absorbance of a material sample is directly proportional to the concentration of the species and the path length.

$$A = -\log_{10}\left(\frac{I}{I_0}\right) = \varepsilon C l \qquad (2)$$

Equation (2) represents Beer-Lambert's law where I_0 and I are intensities of incident and transmitted lights respectively, A is the absorbance, ε is the extinction coefficient, C is the concentration of the species and l is the path length.

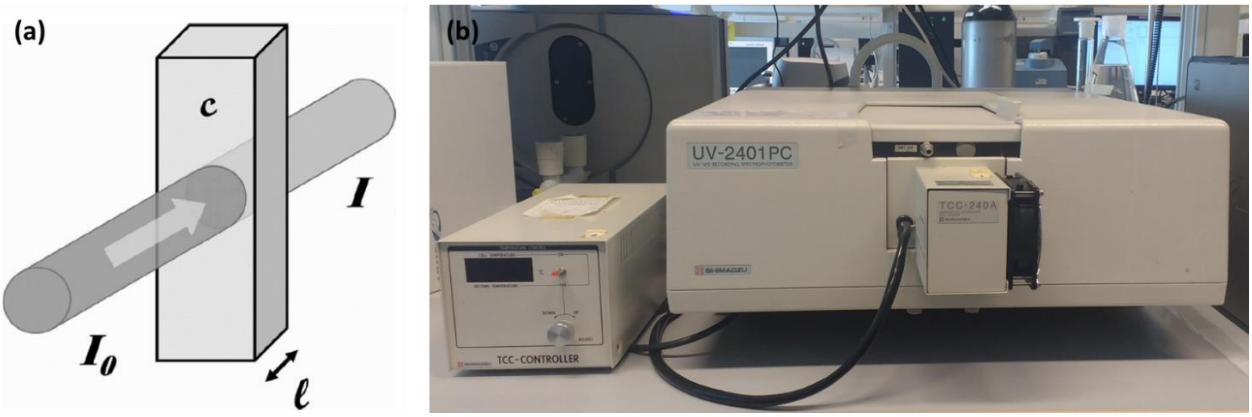

Figure 3.15 (a): Transmission of light through a particle solution [84] (b) UV-Vis spectrophotometer.

3.2.10.3 Scanning Transmission Electron Microscopy (S(T)EM)

S(T)EM was used to determine the size and shape of the inorganic NPs. It consists of an electron gun which generates highly accelerated beam of electrons which are focussed on to a thin sample. The electron beam hitting the sample can either pass directly through the sample, get diffracted or scattered, leading to emission of secondary or back scattered electrons. The electrons are scattered both elastically and inelastically. Elastic scattering is caused as a result of electrostatic repulsion from atomic nuclei which leads to emission of back scattered electrons. Inelastic scattering occurs due to interaction of atomic electrons which leads to emission of secondary electrons. Various detectors placed in the instrument captures information from all these interactions which then gives rise to a virtual image of the sample.

Figure 3.16: Hitachi S-5500 S(T)EM.

Bright field (BF) mode in Hitachi S-5500 electron microscope was used in acquiring the images. In BF mode, the objective aperture is located just below the specimen, which allows only the transmitted electrons to pass down the column. Hence this results in dark images of the NPs in bright background. Few drops of the sample were placed on Formvar carbon coated, 300 mesh copper grids for the analysis. Imaging software SPOT 4.0.1 was used for measuring particle sizes, in which the image pixels were calibrated against the scale bar of the image. 100 particles of each sample were considered in obtaining the average size.

3.2.11 Analysis Techniques

3.2.11.1 Volumetric Collapse Efficiency (VCE) Calculation

VCE provides the percentage decrease in volume of NGs/hybrid NPs after collapse and is therefore an important parameter in comparing the response properties of different NGs and hybrid NPs. VCE was calculated using Equation (3).

$$\mathrm{VCE} = \frac{\mathrm{Volume}_{25^{\circ}\mathrm{C}} - \mathrm{Volume}_{45^{\circ}\mathrm{C}}}{\mathrm{Volume}_{25^{\circ}\mathrm{C}}} \times 100 \qquad (3)$$

3.2.11.2 Volume Phase Transition Temperature (VPTT) Calculation

As discussed in Section 2.2.3.1, VPTT provides a measure of the phase transition temperature for cross-linked NGs. The method reported by Bandyopadhyay, S., et al. [85] was used for obtaining the VPTT. In this method, the temperature runs were performed for the NG and hybrid NP samples in Zetasizer Nano ZS from 25°C to 55°C with a step interval of 5°C. This was followed by a cooling cycle back to 25°C. Swelling and collapse ratios were obtained from these data using Equation (4).

$$\alpha = \left(\frac{D}{D_0}\right)^3 \tag{4}$$

where D is the hydrodynamic diameter of sample at a particular temperature and D_0 is the hydrodynamic diameter at 25°C. The swelling/collapse ratios were then plotted as a function of temperature and a sigmoidal 5 parameter curve was fitted on it. The fit parameters were then used to run a MATLAB® code which resulted in the VPTT by equalizing the area on both sides of the curve. Figure 3.17 shows a schematic representation of the steps involved in obtaining the VPTT. VPTTs for the heating and cooling cycles were calculated separately and an average was taken on triplicate measurements to obtain the final VPTT of the sample.

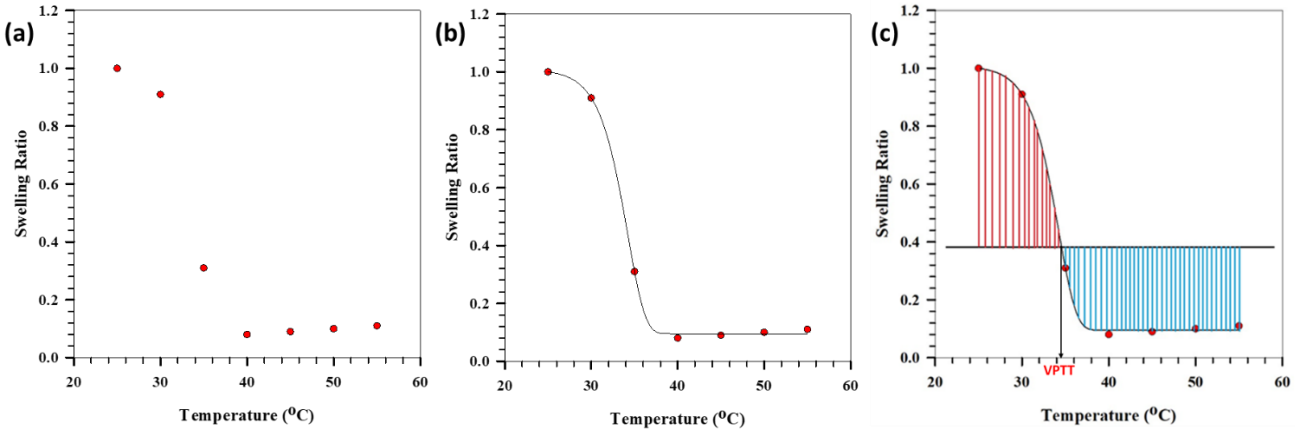

Figure 3.17: Schematic showing calculation of VPTT. (a) Swelling ratios plotted as a function of temperature. (b) Fitting a sigmoidal 5 parameter curve. (c) Equalizing the area and determining VPTT using MATLAB code.

4 Results and Discussion

The results obtained from the study have been presented in this section which are accompanied by discussions on the same. The initial part of this section deals with results obtained on synthesis and characterization of inorganic NSs. This is followed by characterization results obtained for NGs with three different molar compositions of the co-monomer (AAc). The effect of varying pH of the reaction medium has also been discussed. Subsequently, the results obtained on synthesizing hybrid NPs by combining inorganic NSs with NGs have been presented. The effects observed on the physico-chemical properties of the hybrid on changing the concentration, size and surface charge of the inorganic NSs have been reported. The next part of this section presents the observations made on the properties of NGs/hybrid NPs as a result of varying the temperature and pH of the external environment post synthesis. Findings from time-based studies to understand the growth of NGs and hybrid NPs have also been outlined. Finally, the results obtained from loading and release studies performed with Cyt C on the synthesized multifunctional hybrid NPs have been presented.

4.1 Synthesis and Characterization of Inorganic NSs

Au NSs and Ag NS with different properties were used in this study. Au NSs of different sizes and surface charges were synthesized using the procedure mentioned in Section 3.2.1. Ag NS was purchased from BBI solutions. UV-Vis spectroscopy was carried out to obtain the absorbance peak for these NSs. S(T)EM and DLS characterizations along with zeta potential (ZP) measurements were performed to gain information on the size and stability of these NSs. Figure 4.1 shows the UV-Vis peaks and S(T)EM images of the inorganic NSs used in this study.

The single LSPR peak (marked on respective plot) observed from Figure 4.1 coupled with the S(T)EM images confirm the spherical shape of these NPs. The DLS sizes along with ZP values of these NSs have been listed in Table 4.1. The standard deviations mentioned were calculated from triplicate measurements of the same sample unless mentioned otherwise. As mentioned in Section 3.2.1.1, Au NS2 was synthesized using a higher concentration of Au precursor when compared to Au NS1. Keeping the concentration of reducing agent constant, an increase in precursor concentration is expected to give higher particle sizes for the NSs. This is based on the assumption that the entire reducing agent gets consumed in the reaction. This would indicate similar numbers of nuclei getting formed is every case, but a higher supersaturation in case of increased precursor concentration. This can be verified from Table 4.1 which shows an increase in DLS size of 20 nm between the two batches.

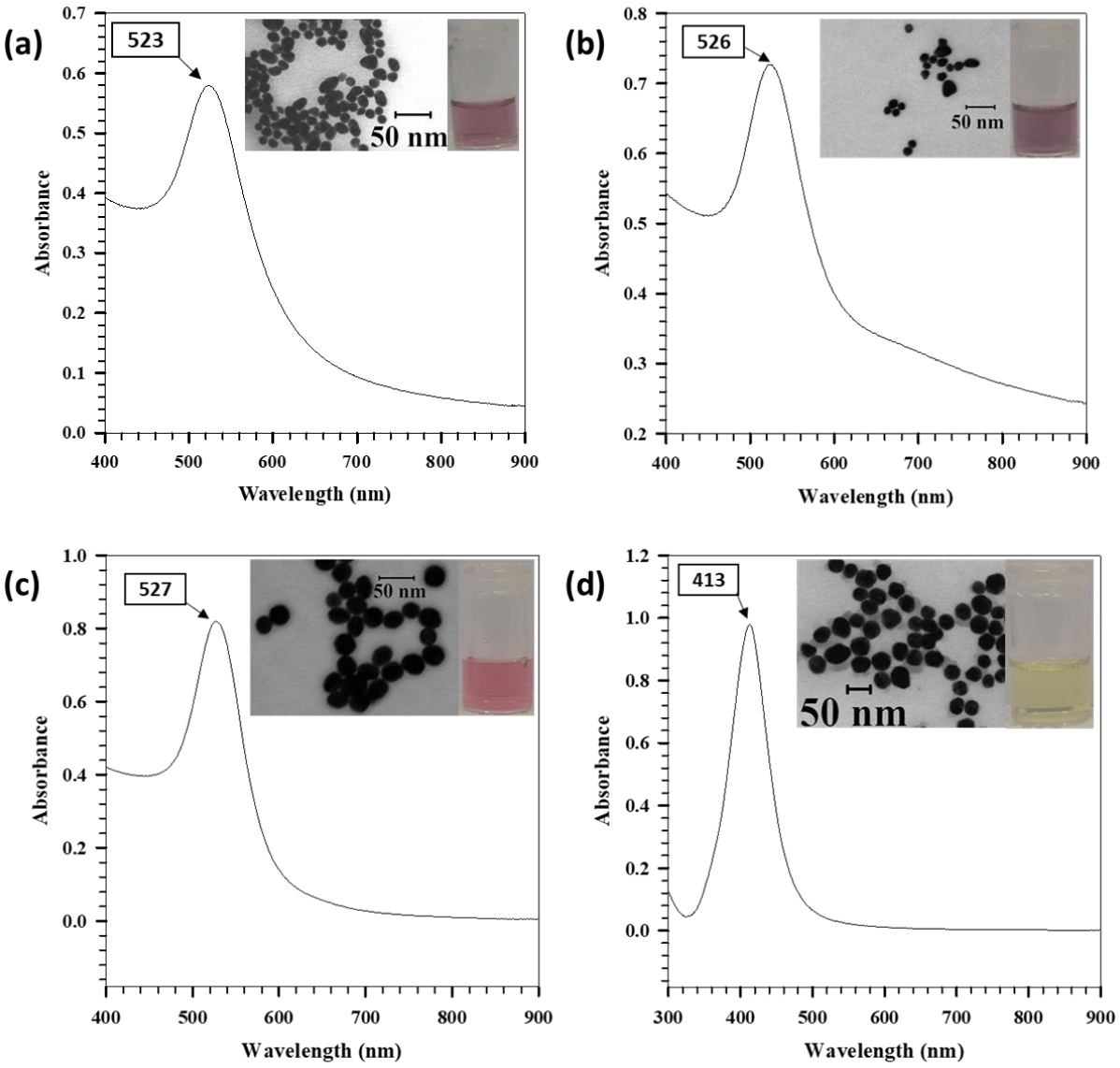

Figure 4.1: UV-Vis spectra and S(T)EM images of inorganic NSs used in the study. (a) Au NS1 (b) Au NS2 (c) Au NS3 (d) Ag NS.

Au NS3 had a similar size when compared to Au NS2 but was synthesized using seed mediated growth (Section 3.2.1.2). From Figure 4.1, a small red-shift in the LSPR peaks could be observed within the Au NSs. Au NS1 which has the smallest size showed absorbance peak at a wavelength of 523 nm in comparison to 526-527 nm for Au NS2/Au NS3. The red-shift observed for Au NS2/Au NS3 verified their increased DLS sizes when compared to Au NS1.

Sample	DLS size (nm)	ZP (mV)
Au NS1	13	-42.7 ± 0.5
Au NS2	33 ± 1	-43.5 ± 1.3
Au NS3	37 ± 1	26.3 ± 3.1
Ag NS	46 ± 1	-46.7 ± 1.4

Table 4.1: DLS size, S(T)EM size and zeta potential of inorganic NSs.

Figure 4.2 shows the plots of sizes and ZPs of the inorganic NSs. Au NS1, Au NS2 and Ag NS are negatively charged while Au NS3 is positively charged. The negative charge is attributed to the presence of citrate on the NP surface, while presence of CTAB induces a positive charge on the surface.

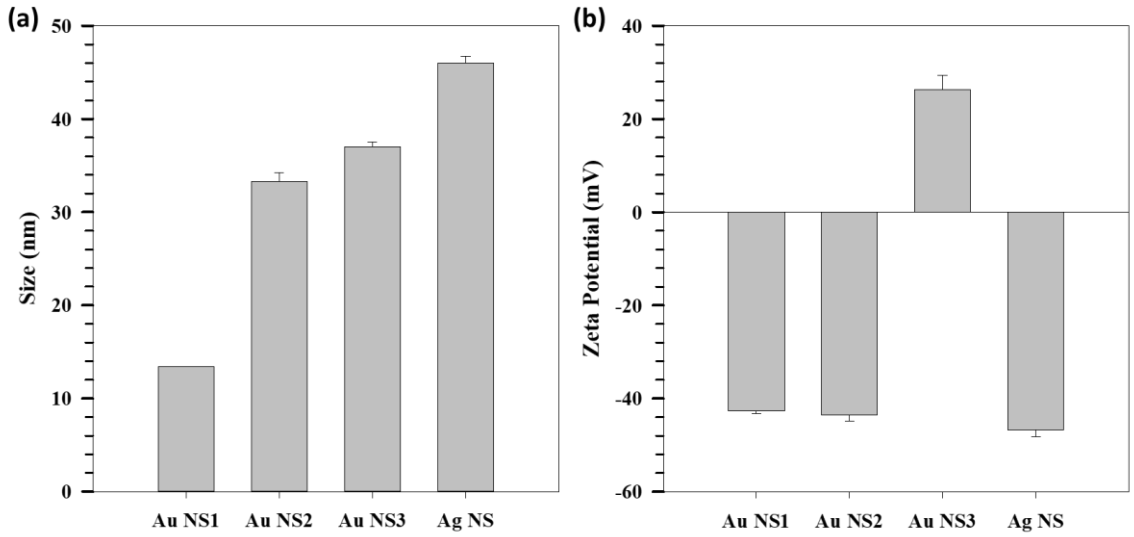

Figure 4.2: Average (a) hydrodynamic sizes and (b) zeta potentials of inorganic NSs.

4.2 Synthesis and Characterization of NGs

pNIPAm-AAc NGs were synthesized by precipitation polymerization using the procedure mentioned in Section 3.2.3. Three different molar ratios of the monomers were used to synthesize NGs with different properties. The molar ratio of the cross-linker (BIS) was kept constant in all three ratios. As can be seen from Table 3.1, the molar ratios were primarily controlled by varying the volume of AAc. Hence, for simplicity, the NG compositions have been denoted as AAc:10, AAc:15 and AAc:25 in the following sections, where the numbers denote the molar ratio of AAc in each sample.

The formation of NGs were accompanied with a characteristic colour change of the reaction mixture from colourless to pale white, which is primarily due to collapse of the formed NG at

the reaction temperature of 70°C (above the VPTT of NG). This colour change could be observed ~ 3-4 minutes of adding the initiator. Figure 4.3 shows the effect of increasing AAc mole ratio on the size and VCE of the NGs. VCE was calculated according to the method mentioned in Section 3.2.11.1. Two batches of recrystallized NIPAm were used to carry out the entire set of experiments in this study. Hence the values listed here are an average of several repeats done with both batches. From Figure 4.3(a), it can be seen that the size of the NGs at 25°C and 45°C show an increase with increase in AAc mole ratio. The sizes measured at 25°C were found to range from 318 ± 26 nm (AAc:10) to 462 ± 23 nm (AAc:25). The VCE, which denotes the effective collapse of the NGs, was found to decrease at higher AAc mole ratio (AAc:25), though the values were found to overlap for ratios AAc:10 and AAc:15. The VCE's ranged between 91.5 ± 0.7 % (AAc:10) and 88.3 ± 1.3 % (AAc:25). This observation could be the result of more AAc units getting incorporated in to the NG matrix with increasing AAc mole ratio. Since AAc units have a carboxylic acid group, they tend to dissociate in aqueous phase (when the pH of the reaction medium is close to or above the pK_a of AAc) leading to hydrophilic groups on the NGs. These hydrophilic groups of AAc could be present on the periphery of the NG or could even be incorporated within the NG matrix.

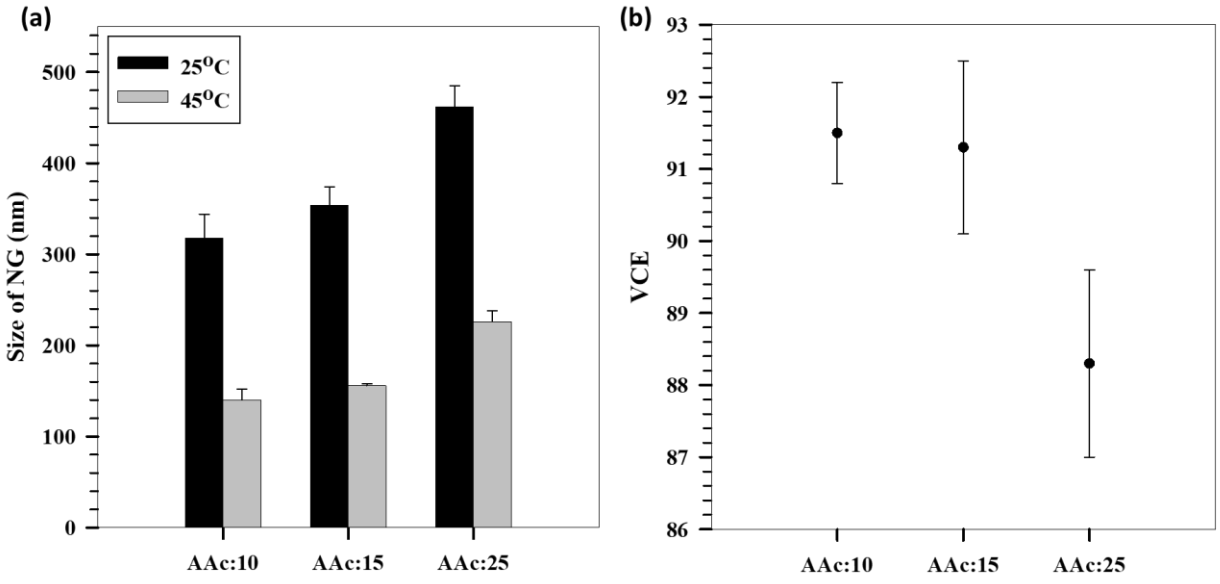

Figure 4.3: (a) Size comparison of NGs with increasing mole ratios of AAc (b) Change in VCE of NG with increasing mole ratio of AAc.

An increasing trend in size with increasing AAc content, could therefore hint towards more hydrophilic units present on the surface of NG, which would show high affinity for water via hydrogen bonds. As a result, increasing AAc could lead to higher swelling of the NGs in aqueous medium, thereby showing an increase in size. Increased swelling at high AAc mole

ratio, would thus provide the NGs a barrier force which needs to be overcome for effective collapse at 45°C. This could explain the decrease in VCE observed in Figure 4.3(b) at high AAc content.

Since ZP would give a better understanding of the surface charge and stability of these NGs, ZP measurements were performed for all three molar ratios at 25°C and 45°C. Figure 4.4 shows the effect of increasing AAc mole ratio on the ZP of the NGs.

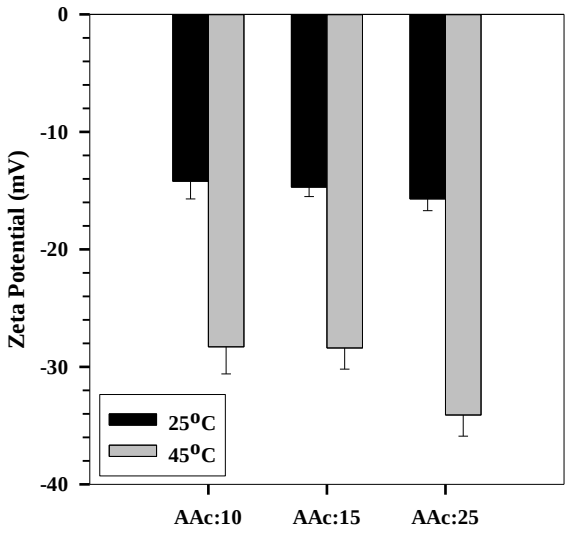

Figure 4.4: Change in zeta potential of NG with increasing mole ratio of AAc.

Though only a very small increase in absolute value of ZP could be observed with increasing molar ratio of AAc at 25°C, there was a substantial increase of ZP at 45°C for AAc:25. The small increase in absolute value of ZP at 25°C could be due to more COO^- units on the surface at higher AAc ratios. Since NGs have a porous cross-linked structure, there could also be many carboxylic acid groups located at the interior of these pores. Heating the NG to 45°C would cause the thermo-responsive part (NIPAm) of the NG to collapse and thereby expose the AAc units located within the pores. This could explain the relatively higher ZP values at 45°C when compared to that at 25°C. Since NGs with AAc:25 are bigger in size compared to the other ratios, it would have more pore space and hence could accommodate more AAc units within the pores. This could be the reason for observing higher absolute values of ZP at 45°C for AAc:25 amongst the different ratios.

4.2.1 Effect of changing pH of reaction medium

In this study, the pH of the reaction medium was changed by controlling the pH of SDS solution added to the reaction mixture. The actual pH of 4.2 mM SDS solution was found to be ~6.

Therefore, a pH value above and below 6 was used for studying this effect. pH 3 and pH 9 were chosen for this study. The pH was controlled using 0.1 M HCl and NaOH. All three ratios of NGs were synthesized at these pH conditions. Figure 4.5(a) shows the effect of reaction medium pH on the size of NGs. It can be observed that at pH 3, the sizes of NGs are larger compared to that at pH 6 and pH 9, irrespective of the NG composition. A similar observation was also made at 45ºC (not shown in Figure). Significant changes in size could not be observed within a particular NG ratio at pH 6 and pH 9.

SDS, structure of which is shown in Figure 4.6, has been reported to provide charge stabilization to the NIPAm monomer during NG synthesis [14]. Reducing the pH to 3 using HCl, would lead to H^+ and Cl^- ions in the reaction mixture and this could probably mask the charge stabilization provided by the surfactant. This could lead to more monomers coming close to each other thereby forming bigger NGs. Whereas an increase in pH using NaOH might not lead to dissociation into Na^+ and OH^- ions due to already existing Na^+ counter-ions of the surfactant. Hence, the sizes at pH 9 remains similar to that at actual pH (pH 6).

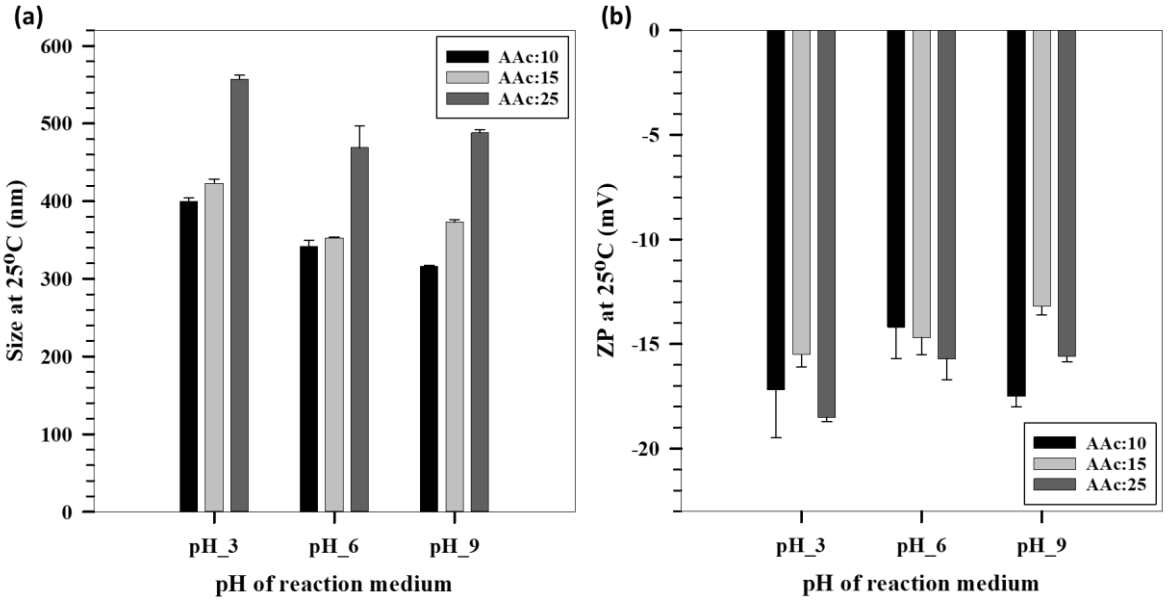

Figure 4.5: Variation in (a) size and (b) ZP of NG as a function of pH of reaction medium.

The pH of reaction medium was observed not to have an effect on the ZP of NGs. This could be because ZP is determined by the amount of AAc units on the NG surface. Change in charge stabilization of the NIPAm unit brought about by changing the pH of reaction medium might not affect the AAc units getting incorporated in the matrix. VCEs of the NG systems were also found to be fairly similar at the mentioned pH values.

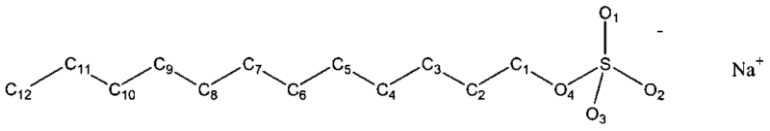

Figure 4.6: Structure of SDS [86].

4.3 Synthesis and Characterization of hybrid NPs

Hybrid NPs were synthesized by combining inorganic NPs with NGs as mentioned in Section 3.2.4. The synthesis procedure was similar to that of NGs, except for that a known concentration of NP was dispersed in SDS solution prior to its addition. In the presence of inorganic NPs, the characteristic colour change for the hybrid during synthesis was observed ~ 2.5 minutes which was less than that for NGs. In case of hybrid NPs, the colour of the hybrid resembled that of the inorganic NP used in the synthesis. Inorganic NPs might act as nucleation sites for the polymerization and thereby enhance the overall kinetics of the reaction. This could be a reason why the colour change is observed earlier when compared to bare NGs. Another observation which was made during the synthesis of hybrid NPs was that of inorganic NPs sticking to the magnet. At the end of reaction, a fraction of the introduced NPs was found sticking to the magnet (Figure 4.7). This could probably be due to the charges present of the NPs or due to the hydrophobic surface of the magnet. In order to analyse this precipitate, the magnet was gently washed with MQ water and the mass sticking to the magnet was then sonicated and brought in to solution. An increase in size observed at 45^{o}C for this precipitate, could possibly denote aggregation of NPs at high temperature, thereby serving as a proof that these could be bare NPs.

Figure 4.7: NPs sticking to magnet after reaction.

The reaction was tried at higher stirring speeds (550 rpm) to provide better mixing and thereby avoid NPs sticking to the magnet. However, no hybrid NPs were formed in this case (Appendix B). Since similar quantities of NPs were observed to stick in all cases, the effect was assumed

to be constant and hence neglected. The effect of concentration, size and surface charge of inorganic NPs on the hybrid were studied in this section.

4.3.1 Effect of Concentration

In addition to enhanced physico-chemical properties obtained in hybrid NPs, it is also important to detect them. Hence, optimizing the concentration of NPs in the hybrid would provide the minimum concentration that gives a distinct LSPR peak for Au. All NP stock solutions were maintained at 3 mg/ml. Au NS1 was used to study the effect of concentration. Different volumes of this stock were taken (corresponding to 0.5 mg, 0.75 mg, 1.0 mg and 2.0 mg NPs) and centrifuged. This was re-dispersed in 5 ml of 4.2 mM SDS solution and then added to the reaction mixture. The NG composition with AAc:10 was used for this study. Figure 4.8 shows the effect of NP concentration on the size and VCE of hybrid NPs. 'X' axis represents the weight of NPs in the reaction mixture.

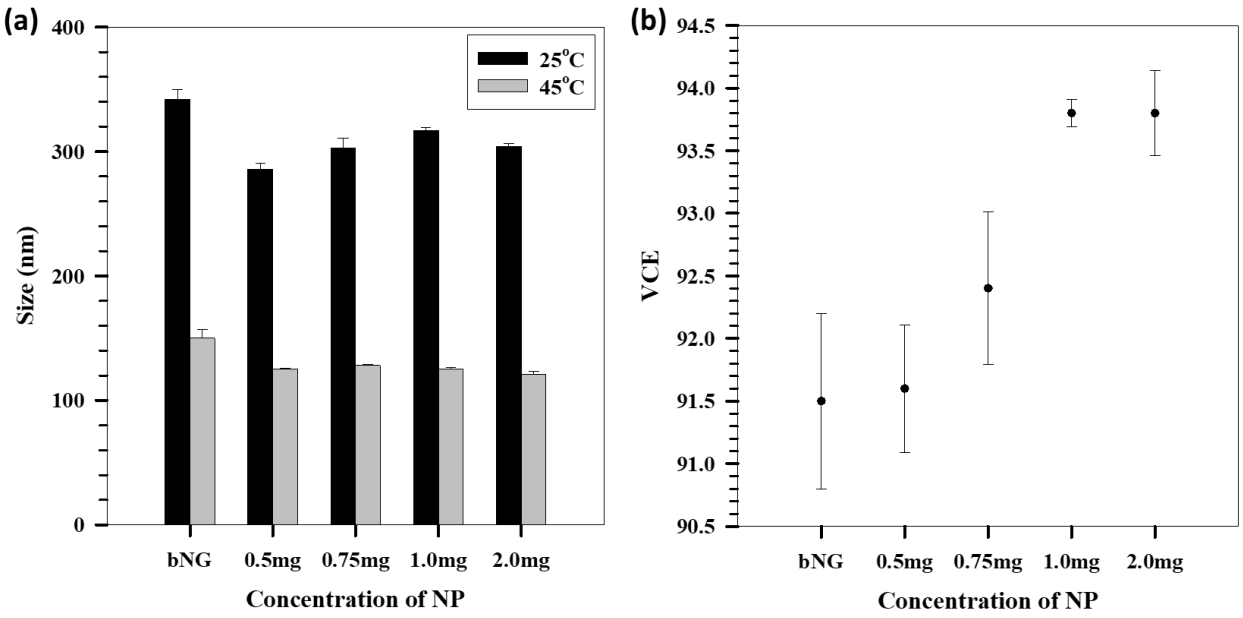

Figure 4.8: Effect of concentration of inorganic NP on the (a) size, and (b) VCE of hybrid NP.

From Figure 4.8(a), it can be observed that the sizes of the hybrid NPs were fairly similar (maximum deviation ~9%) with increasing NP concentration. However, a slight decrease in size with respect to bare NGs could be observed. A possible explanation for this observation could be location of most NPs inside the pores of the NGs (as NP sizes could be much smaller when compared to the pore dimensions of the NG). Hence, the sizes of the hybrid NPs would not change with increasing concentration of small inorganic NPs (~13 nm in this study). A similar observation has been reported in literature [79] even at a higher size of NP (~60 nm).

But incorporating NPs having sizes larger than the pore dimensions of the NGs might hinder their entry inside the matrix leading to terminal location of the NPs. Presence of NPs within the NGs might lead to cross-linking of the chains thereby leading to more hydrophobic interactions in the NG. This could probably be a reason for smaller size of hybrid NPs compared to the bare NGs.

From Figure 4.8(b), an increasing trend could be seen in the VCE's with an increase in NP concentration. This could again support the previous hypothesis on the location of NPs. Improved cross-linking imparted by the NPs within the hybrids might enhance the collapse of these hybrids leading to higher collapse efficiencies.

UV-Vis spectroscopy was performed on these hybrid NPs to confirm the presence of Au NPs in it. The absorbance values obtained for hybrid NPs from UV-Vis spectrophotometer was normalized with respect to bare NGs to observe the peak for Au. Figure 4.9 shows the plot of normalized absorbance as a function of wavelength for the hybrid NPs at different NP concentrations. The plots were smoothed using "Smoother 2D" function in Sigma Plot 14.0. From the plot, a more prominent peak for Au could be observed with increasing concentration of Au NPs. However, the peak observed was ~545 nm, when compared to the absorbance peak wavelength of bare NPs (523 nm). This shift is a result of increase in local refractive index at the Au NP surface, and thereby confirms the incorporation of Au NPs in the NG matrix. Previous works in literature (Section 2.5.1) have also reported a red-shift in LSPR wavelength of Au NPs with polymer coating on its surface.

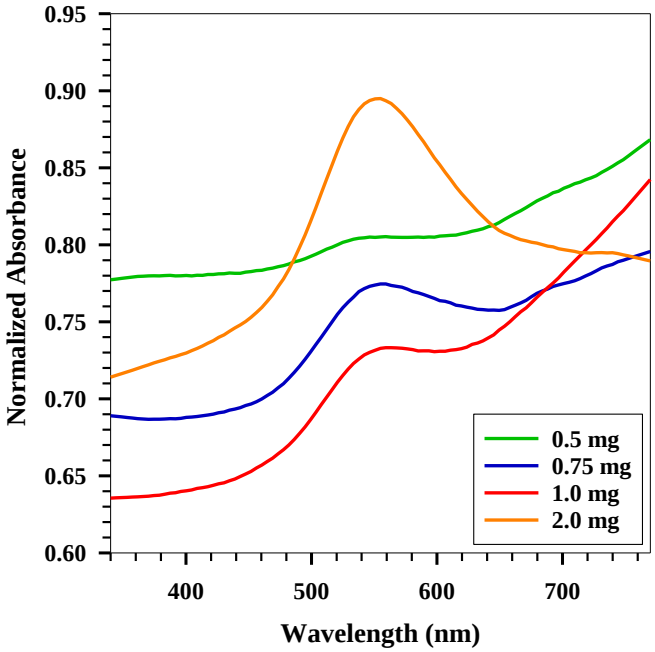

Figure 4.9: Normalized absorbance plot of hybrid NPs with various concentrations of NPs showing the peak for Au.

From Figure 4.9, since 0.75 mg NPs show a clear peak for Au, this was used as the optimized value for the remaining experiments. Therefore, all experiments with hybrid NPs mentioned from here on will be based on 0.75 mg of NP concentration. Using this concentration, hybrid NPs with different AAc ratios were synthesized to compare it properties with that of corresponding bare NGs. The results from this experiment, has been shown in Figure 4.10. In this section, 'bNG' and 'hNP' mentioned in plot legends correspond to bare NGs and hybrid NPs respectively.

From Figure 4.10(a), a small decrease in size can be observed for hybrid NPs at molar ratios of AAc:10 and AAc:15. Even though hybrid NP with AAc:25 showed a higher average size, it was within the error bars for the corresponding bare NG.

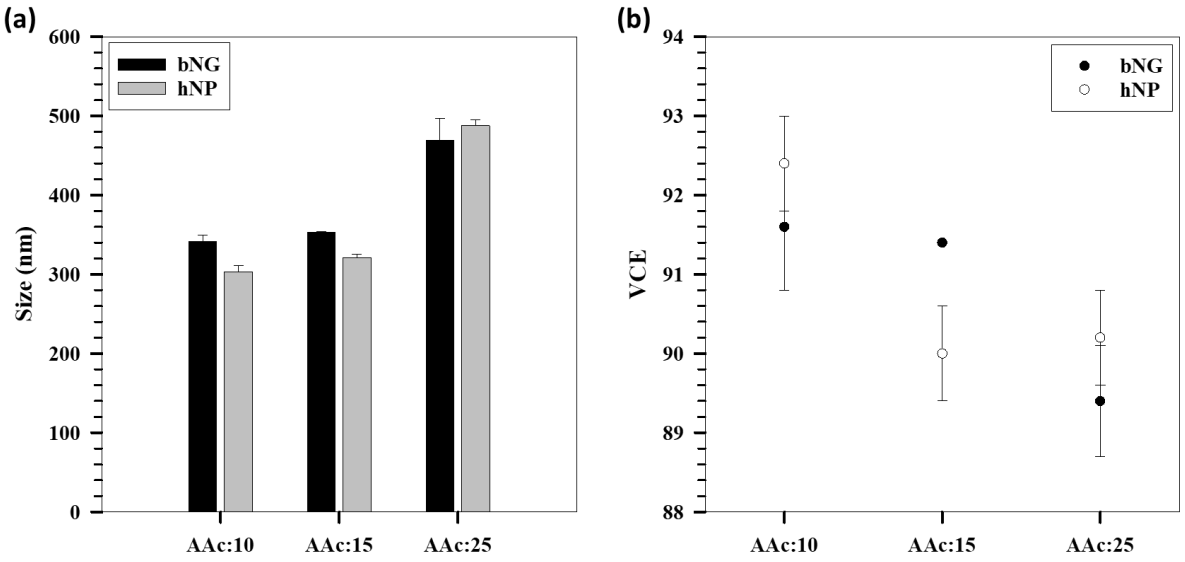

Figure 4.10: Comparing bNGs and hNPs of different AAc mole ratio.

Figure 4.10(b) shows a comparative plot of VCE's for bare NGs and hybrid NPs with different compositions. Similar to the observations made in bare NGs, VCE's of hybrid NPs were also observed to decrease with increasing mole ratio of AAc. However, no significant change could be observed in VCE between hybrid NP samples at AAc:15 and AAc:25.

4.3.2 Effect of Size

The effect of size of inorganic NPs on the hybrid was studied in this section. Au NS1, Au NS2 and Ag NS were used for this study. Au NS1 had the smallest size (13 nm) while Ag NS were the biggest (46 ± 1 nm). All three NSs used had similar surface charges. NG composition with AAc:10 was used for the reactions. As can be observed from Figure 4.11, increasing sizes of NSs seemed to have no effect on the size of the hybrid NPs. As mentioned in the previous Section, this could be due to larger pore dimensions of the NG when compared to the size of the NPs. This could lead to incorporation of all NPs inside the NG matrix, thereby leading to no significant change in the size of hybrid. A similar observation was reported by Raghunathan, et al. [79] where no substantial effect could be seen even on increasing the size of NPs from ~ 46 nm to ~150 nm.

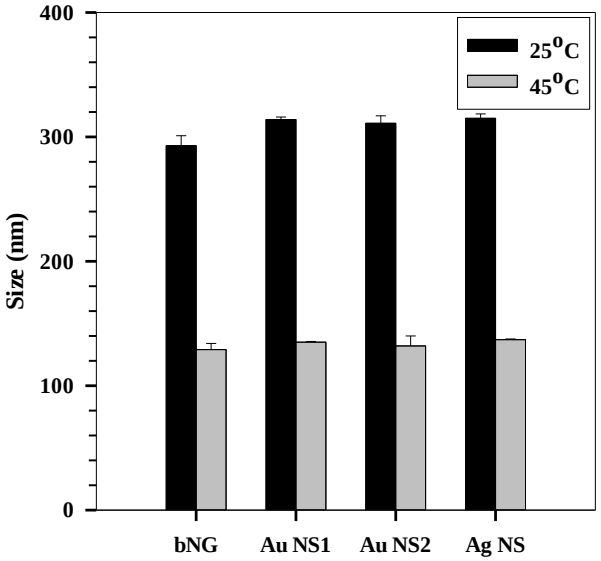

Figure 4.11: Effect of NP size on the size of hybrid NP.

Since NG composition with AAc:10 (having smallest dimensions) was used in this study, using NGs with higher AAc mole ratios (bigger sizes) was thought to have a similar effect (since these would have larger pore dimensions). As the size at 45°C for the hybrid NPs also remained fairly constant, no effect could be observed on the VCE as well.

4.3.3 Effect of surface charge

The effect of NP surface charge on the properties of the hybrid NP was studied by incorporating Au NSs of similar sizes but different surface charges. Au NS2 and Au NS3 were used in this study. The presence of citrate coating provided a negative charge (-43.5 ± 1.3 mV) on Au NS2, whereas CTAB coating gave a positive charge (26.3 ± 3.1 mV) on Au NS3. Changing the surface charge on the Au NSs showed no effect on the properties of the hybrid. This can be observed from Figure 4.12, as the size and zeta potential of the hybrid NPs showed no significant change.

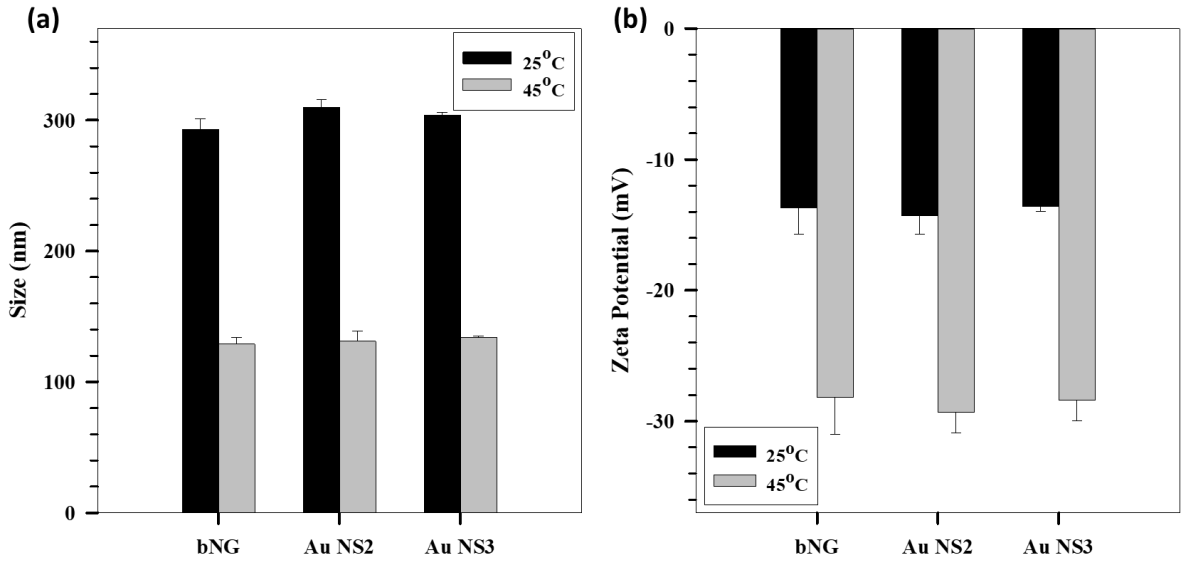

Figure 4.12: Effect of NP surface charge on the (a) size, and (b) zeta potential of hybrid NP.

4.4 Swelling-Collapse properties as a function of temperature

Temperature response of the NGs and hybrid NPs were studied by increasing the temperature of the sample from 25°C to 55°C, followed by a cooling cycle back to 25°C. The swelling ratios of the samples were obtained as discussed in Section 3.2.11.2, by cubing the hydrodynamic sizes obtained at a particular temperature and dividing it by the corresponding value at 25°C. Sizes at 25°C obtained from the initial point on the heating cycle and final point on the cooling cycle were considered separately for obtaining the heating and cooling curves. Figure 4.13 shows the comparison of swelling ratio as a function of temperature for NGs/hybrid NPs with different AAc content. The plots have been obtained by taking an average of swelling ratios shown by various samples synthesized using two different NIPAm batches. Hence, any differences between the NIPAm batches would be captured in the error bars provided.

Figure 4.13, a more rapid response to temperature could be observed with increasing AAc mole ratio. However, no significant changes could be seen between bare NGs and hybrid NPs containing same mole ratio of AAc. Since larger sizes could be observed for NGs/hybrid NPs with increased AAc mole ratio (Figure 4.10), these might also be characterized with bigger pore sizes. Studies conducted by Yan, Q., et al., have reported rapid swelling and de-swelling characteristics of pNIPAm hydrogels with increased pore sizes and porosities, when cycled through the VPTT [87]. Therefore, these observations could possibly hint to bigger pore sizes of NGs/hybrid NPs with high AAc mole ratio. Similar observations could also be made from the size versus temperature plots of these samples (Shown in Appendix C).

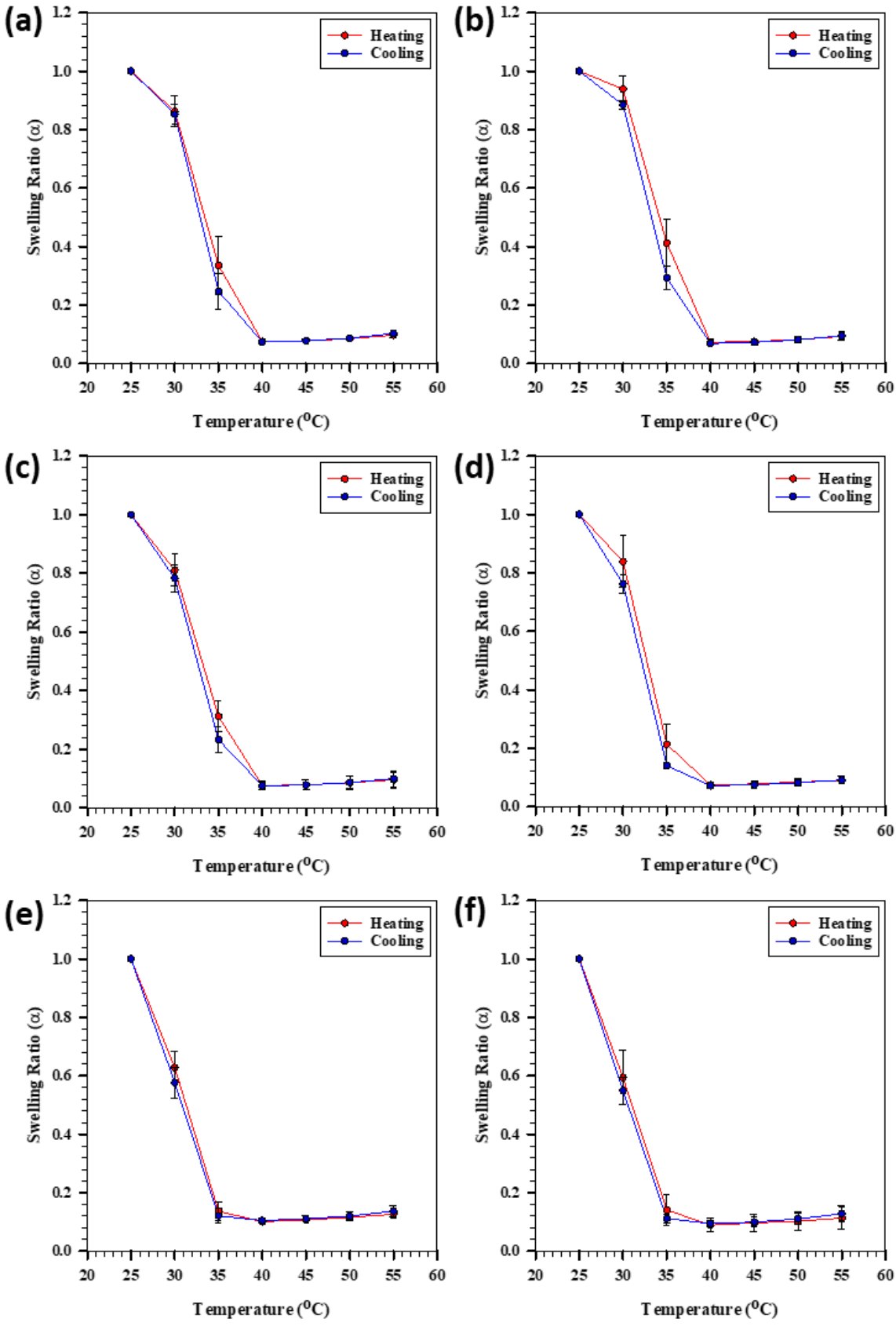

Figure 4.13: Swelling ratio versus temperature for (a) bNG_10 (b) hNP_10 (c) bNG_15 (d) hNP_15 (e) bNG_25 (f) hNP_25.

The VPTT of these samples were calculated by the method described in Section 3.2.11.2. Figure 4.14 shows the VPTT comparison between NG and hybrid NP at different AAc ratios. As previously mentioned the VPTT values shown in the plot are also based on an average obtained from various samples synthesized using two different NIPAm batches. The error bar for bare NG at AAc:25 was found to be quite high. This could be due to greater heterogeneity in the subchain lengths of the NG when compared to that at lower AAc ratios. The regions in the NG with longer subchain lengths would collapse at a lower temperature than the regions with shorter subchains [50].

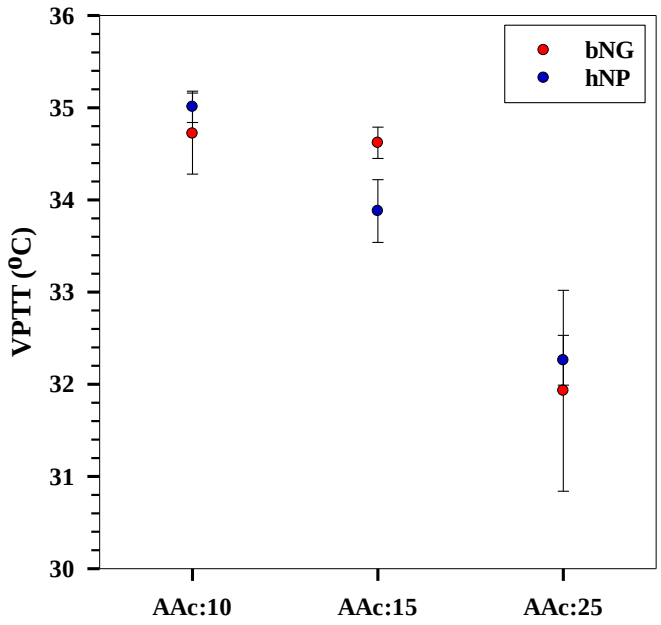

Figure 4.14: VPTT comparison between bNG and hNP at different AAc ratios.

It can be observed that the VPTT of NGs and hybrid NPs decrease with increasing AAc mole ratio. As discussed in Section 4.2, an increase in AAc mole ratio would lead to increased swelling of the NGs/hybrid NPs. Increased swelling would indicate higher energy requirement to break the hydrogen bonds to get into the collapsed state. This would hint towards a higher VPTT with increase in AAc content. This has been previously reported by Lue, S.J., et al.[88] for PNIPAm-co-AAc hydrogels synthesized via redox polymerization method. However, a reverse trend observed in this case could lead to a hypothesis that VPTT would not only depend on the hydrophilic interactions but can also be influenced by other properties of the system such pore size and porosity of the matrix.

4.5 Swelling-Collapse properties in response to pH

pH response of the NG and hybrid NP samples were obtained by varying the pH of the samples from 3 to 9 at step intervals of 0.5 using an auto-titrator as described in Section 3.2.10.1. This provided the response of the samples at 25°C. Manual pH studies were also performed to confirm these results, which in addition also provided the pH response at 45°C. Size and zeta potential measurements were recorded as a function of varying pH of solvent. Since the original pH of the sample was ~3.8, the pH was initially dropped down to 3 and then increased to 9.

Figure 4.15 illustrates the pH response obtained for NGs and hybrid NPs using auto-titrator. The numbers succeeding 'bNG' and 'hNP' in the plot legends correspond to the mole ratios of AAc used. For instance, 'bNG_10' would represent bare NG sample having AAc molar ratio of 10.

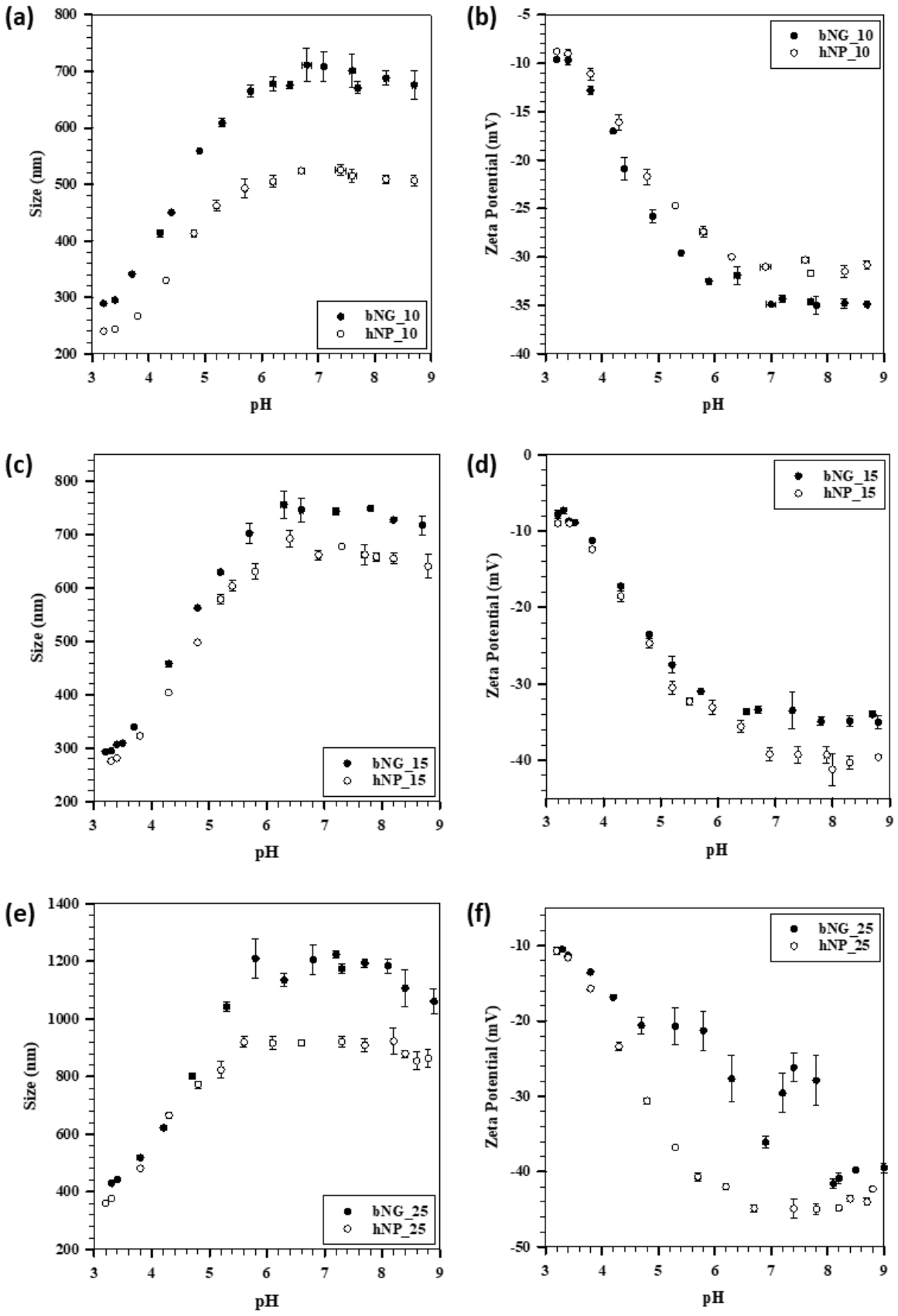

Figure 4.15: Effect of pH on (a) size and (b) ZP of bNG_10 and hNP_10; (c) size and (d) ZP of bNG_15 and hNP_15; (e) size and (f) ZP of bNG_25 and hNP_25.

From Figure 4.15, a small collapse (~55%) of NGs/hybrid NPs could be observed at low pH (~3) followed by swelling with an increase in pH. As discussed in Section 2.2.3.2, this occurs due to protonation of carboxylic group of AAc at a pH lower than the pK_a of AAc (4.25 at 25°C). Increasing the pH above the pK_a value, would lead to de-protonation of the weak carboxylic groups, and thereby lead to swelling of the NG/hybrid NP as a result of Coulombic repulsion between the charged monomer units and more favourable solvation of the deprotonated monomer by the solvent [50]. The reduced collapse of these systems at low pH would signify no effect of pH on the thermoresponsive part of these NGs/hybrid NPs. Hence a temperature above VPTT and low pH would indicate maximum collapse in these systems.

From Figure 4.15 (a), (c) and (e), it can be observed that the sizes of hybrid NPs were comparable to that of bare NGs at low pH but decreased with an increase in pH. This shows that the swelling in case of hybrid NPs were less compared to bare NGs. A plausible explanation for this observation could be the improved cross-linking and hydrophobic interactions brought about by the incorporation of NPs in the NG matrices. This might limit the extent of swelling in hybrid NPs.

Figure 4.15(b), (d) and (f) show the variation in ZP for bare NGs and hybrid NPs as a function of increasing pH. The absolute value of ZP was found to increase as the pH went to basic conditions. This again proves the fact that AAc would be in an associated state at low pH, which results in lower charge density on the particles. With increasing pH, due to enhanced dissociation of carboxylic group, the charge density on particle increases thereby bringing about an increase in ZP.

The important thing to be noted here is that the stimuli causing the collapse of the NG/hybrid NP systems govern the charge density on the particles. A collapse brought about by increasing the temperature above VPTT of these systems will enhance the charge density as the dissociation of AAc units are not affected in this case (discussed in Section 4.2). Whereas a collapse brought about by reducing the pH below the pK_a value would lead to a decrease in charge density.

Similar trends observed in manual pH runs could be used to confirm this effect. In case of manual pH runs, the sizes of the NGs/hybrid NPs were observed to be similar to that obtained using auto-titrator at low pH values. However, the sizes obtained at higher pH values were lower than that obtained from auto-titrator. This could be due to different steps of pH increase in the two methods. This could also be due to high PDI which can be observed in Figure 4.15 at increased pH.

Furthermore, manual pH runs were used to obtain the pH response of these systems at 45°C. Both NGs and hybrid NPs were found to swell at 45°C with increase in pH. Figure 4.16 illustrates the swelling observed with increase in pH. The sample pH was initially brought down to 3 and the temperature was set to 45°C. This would bring the system into a state of maximum collapse which could be observed by the solution turning turbid (Figure 4.16(a)). With increasing pH above pKa, the turbidity of the solution was found to disappear gradually, and the solution turned colourless ~ pH 7 (Figure 4.16(b)). This indicates that pH is the parameter of greater significance in these systems as it could lead to swelling of NGs/hybrid NPs maintained above their VPTT.

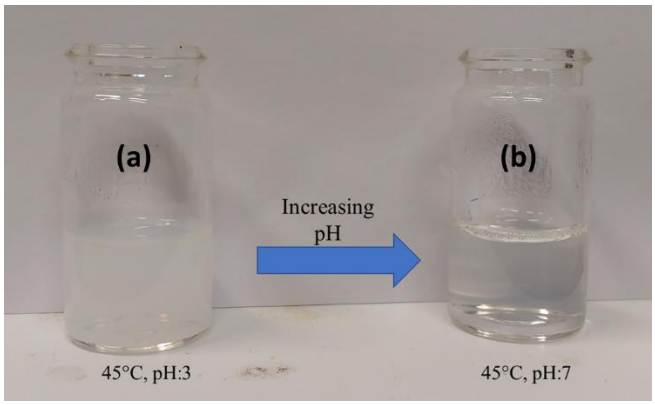

Figure 4.16: Swelling of NGs with increase in pH at 45ºC (a) pH 3 (b) pH 7.

Another interesting observation made during manual pH runs was an increased swelling of NGs/hybrid NPs at 45°C compared to 25°C. This is shown in Figure 4.17. It can be observed that at low pH, the size at 45°C was smaller than that at 25°C (due to collapse of particles), but a reverse trend could be seen with increasing pH. This could be explained by the location of AAc units in the NGs/hybrid NPs. As discussed in Section 4.2, there could be a fraction of AAc units located inside the pores of the NG matrix. These units would get exposed at temperatures greater than the VPTT. Hence at a pH of 3 and 45°C, even though there would be increased AAc units on the surface, these would be in an associated state. Increasing the pH, would lead to deprotonation of the of these units, thereby forming more hydrophilic carboxylic groups on the surface and enhanced swelling. As can be seen from Figure 4.17(a), this effect was not so pronounced in bare NGs and hybrid NPs having low mole ratios of AAc (AAc:10). This could be due to smaller sizes of these systems which would also indicate lower fraction of AAc units within the matrix.

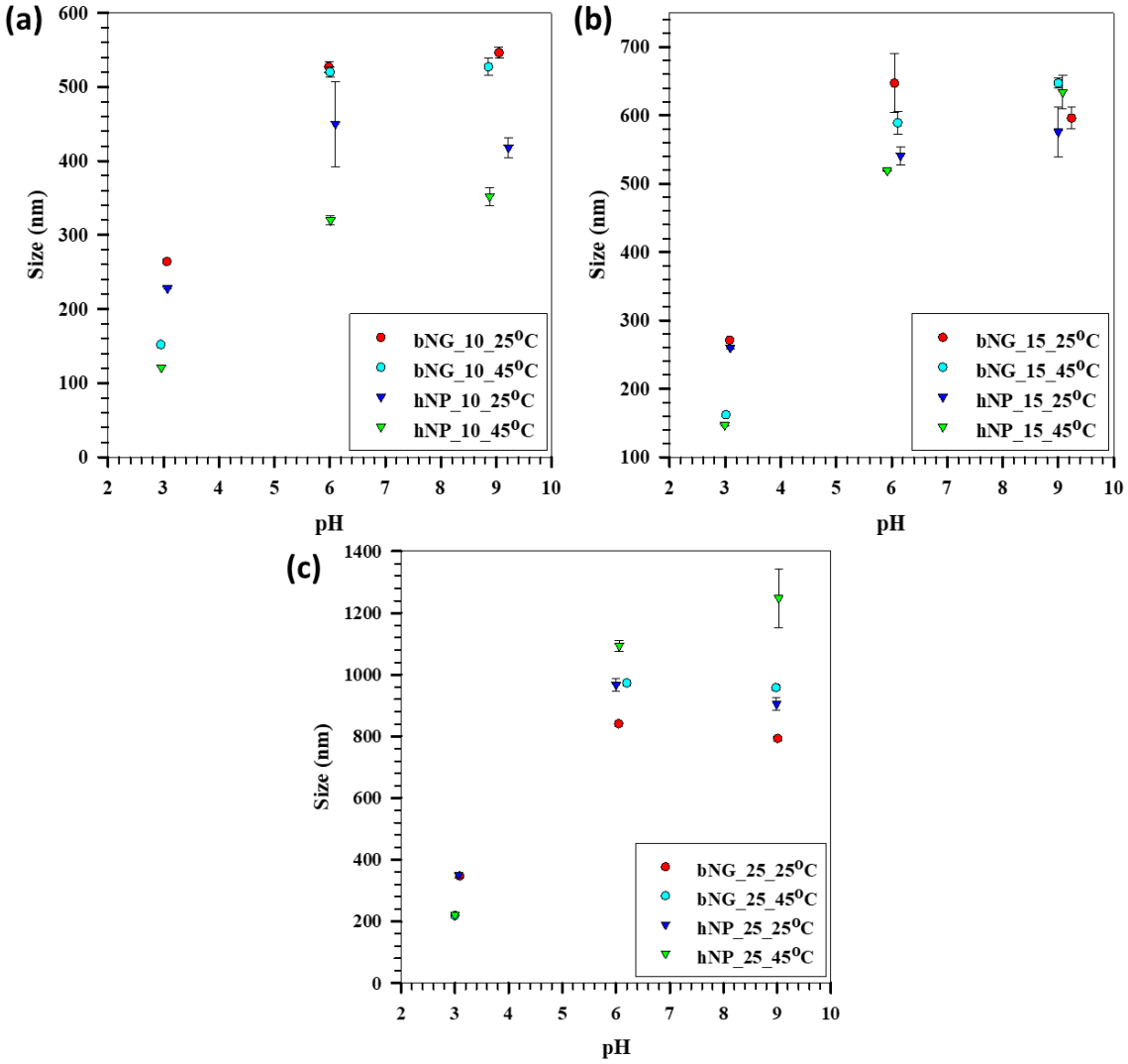

Figure 4.17: pH response of bNG and hNP at 25ºC and 45ºC, (a) bNG_10 and hNP_10, (b) bNG_15 and hNP_15, (c) bNG_25 and hNP_25.

4.6 Time based studies

Time based studies were performed for both NGs and hybrid NPs to get a better understanding on their growth. This was performed by following the procedure mentioned in Section 3.2.7. A predetermined volume of the reaction mixture was withdrawn at intervals and put in ice-cold water to arrest the reaction. Previous works from literature had studied the effect of loss of solvent during the reaction by replenishing the lost volume with MQ water maintained at reaction temperature. The loss of solvent was reported not to have an influence on the growth of NGs [79]. However, the studies performed in this section were carried out by replenishing the withdrawn volume with MQ water maintained at 70°C.

Two similar experiments were carried out simultaneously for each timed study in order to capture more time points during the reaction phase. Two common time points (at 10 minutes

and 2 hours) were also chosen from the experiments to compare any differences within the samples. Obtaining similar sizes at the common points proved that data points from both experiments could be combined to obtain the overall growth curve for the samples. Few minutes into the addition of AAc and KPS to the reaction mixture, a visible colour change could be observed in both NGs and hybrid NPs. A pale whitish colour could be observed for NGs and pinkish white colour for hybrid NPs (pinkish due to the presence of Au NPs). This would indicate the collapse of initially formed polymers to form the nuclei. It was noted that the induction time for showing an observable colour change was slightly shorter in hybrid NPs (~2.5 min) when compared to bare NGs (~3.5 min). A probable explanation for this observation could be NPs acting as nucleation sites, thereby leading to heterogeneous nucleation.

Previous studies on similar NGs had reported very high standard deviations for time points before observable colour change [79]. Therefore, in this study the first time point was taken at the point of observable colour change. The plots of sizes, normalized sizes and ZP's of these samples against reaction time have been discussed below.

Figure 4.18 shows the size comparison of bare NGs and hybrid NPs at different time points measured at 25°C. The sizes reported in this section are the ones obtained before dialysing the samples. From Figure 4.18, a rapid increase in size could be observed up to 10-15 minutes from the point of colour change. This would indicate the growth of precursor particles by combining with other precursor particles via crosslinks. Following the initial increase, the sizes of NGs/hybrid NPs were observed to stabilize. Except for hNP_10, hybrids at other mole ratios of AAc were observed to stabilize at a smaller size compared to bare NGs. This could be due to improved hydrophobic interactions between the chains with the incorporation of NPs. Even though hNP_10 showed higher sizes compared to bNG_10 at few initial time points, a smaller size for the hybrid could be observed at later time points.

Higher standard deviations were observed in sizes of hybrid NPs with AAc:25 between 20-60 minutes of adding the initiator. This could indicate that though the sizes tend to stabilize after the rapid initial growth, there could be precursor particles getting formed at later stages leading to non-uniform growth. A similar observation was previously reported by Chen, S., et al., [76] while studying the reaction mechanism of NIPAm polymerization.

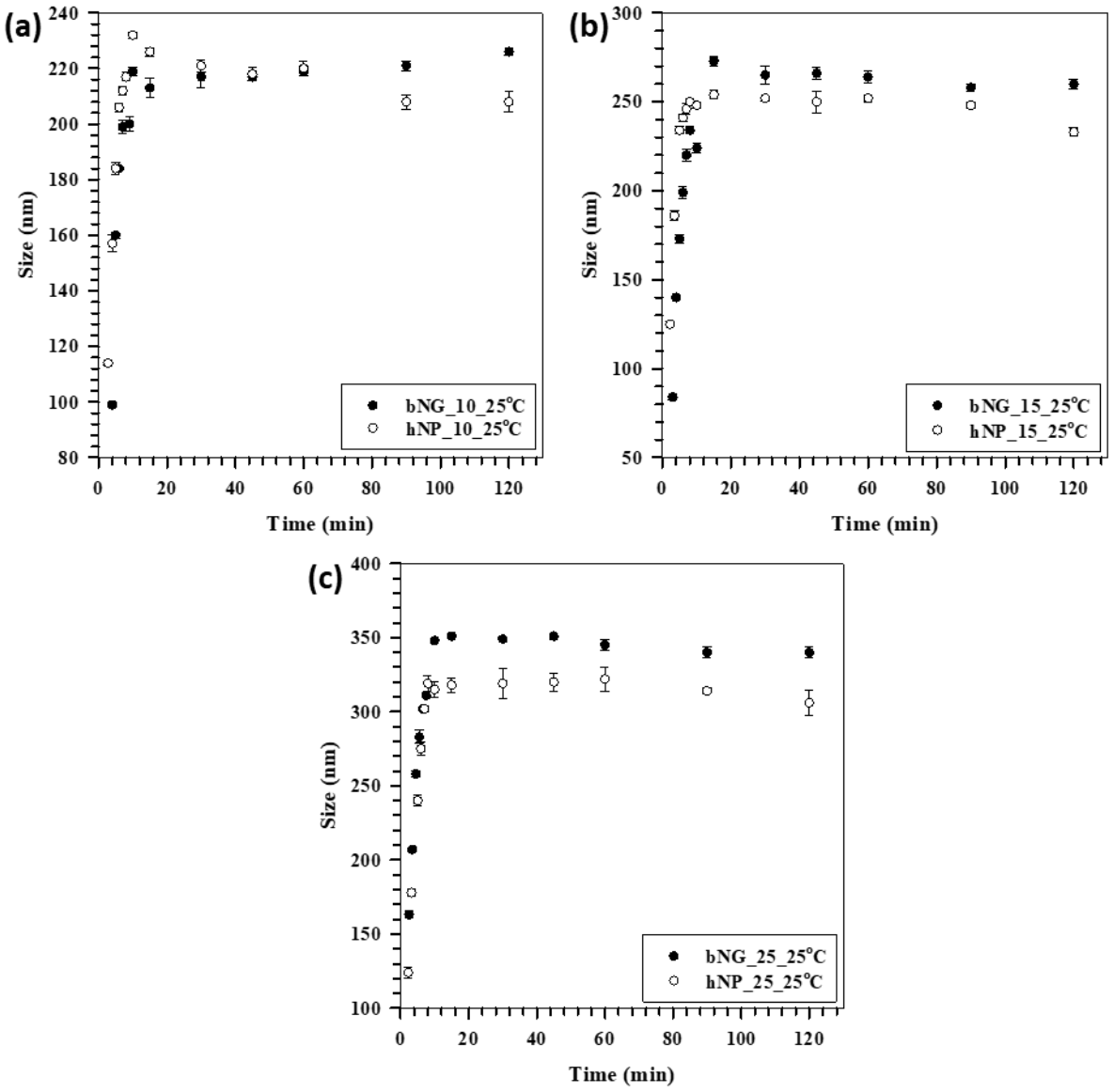

Figure 4.18: Size as a function of reaction time for (a) bNG_10 and hNP_10, (b) bNG_15 and hNP_15, (c) bNG_25 and hNP_25.

As normalizing the plots would help in providing better insights into the growth, the sizes of bare NGs and hybrid NPs were normalized with respect to average final size obtained for these systems. Figure 4.19 shows the plots of normalized sizes as a function of reaction time. All plots were observed to take the shape of a sigmoidal curve. Sigmoidal 5 parameter equation was fitted to these plots and R^2 values of ~0.99 ensured excellent accuracy of the fit (Appendix D). By knowing the order of reaction and using a similar sigmoidal fit, the rate constants could be obtained by using the fit parameters. This could be used to compare the reaction kinetics of bare NGs and hybrid NPs. However, it was difficult to predict the reaction order from these studies. A more detailed study into the kinetics of the growth is beyond the scope of this thesis.

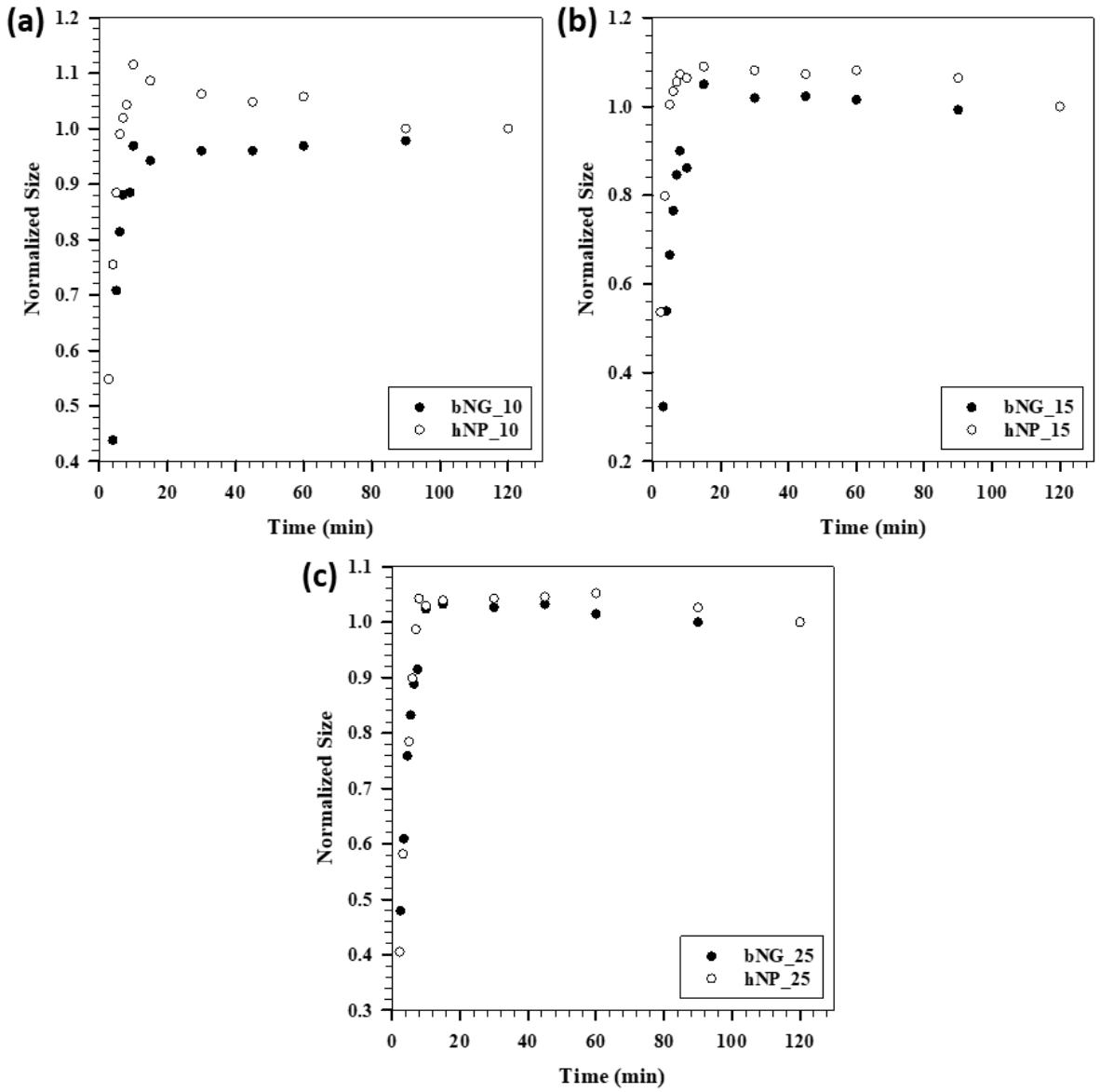

Figure 4.19: Normalized size (at 25C) of bNG and hNP as a function of time (a) bNG_10 and hNP_10 (b) bNG_15 and hNP_15 (c) bNG_25 and hNP_25.

The ZP of the hybrid NPs (before dialysis) with different AAc mole ratios were also measured as a function of reaction time. This is shown in Figure 4.20. A gradual decrease in absolute value of ZP could be observed with increasing reaction time. Previous studies have reported the charged hydrophilic persulfate radical ($-SO_4^-$) of initiator (KPS) to stabilize the precursor particles [76]. The combined stability provided by the initiator and SDS surfactant could be the reason for higher stability at initial time points. As the reaction proceeds, AAc units get cross linked in the network leading to stability imparted by dissociated carboxylic groups. But the charge stabilization provided by the carboxylic groups on the surface could be masked due to the presence of loosely bound surfactant on the surface. This could be the reason for the gradual

decrease observed in absolute value of ZP. The ZP measured after overnight dialysis (not shown in Figure) were observed to show higher absolute values (~ -15 mV), which could probably indicate the removal of loosely bound surfactants, thereby enhancing the charge stabilization provided by AAc units.

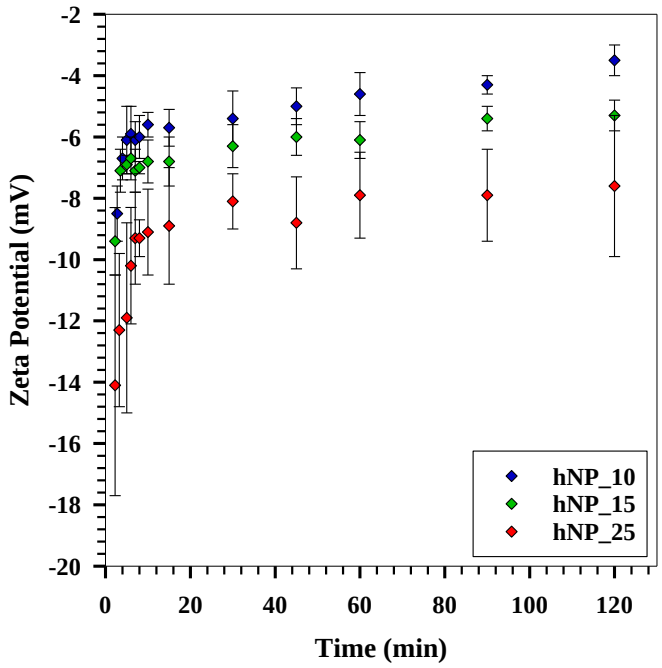

Figure 4.20: ZP as a function of reaction time for hybrid NPs (AAc:10,15,25).

From Figure 4.20, a higher absolute value of ZP could be observed throughout with increasing AAc mole ratio. This observation would probably indicate that even though a masking effect could be observed due to loosely bound surfactants, more carboxylic groups on the surface could provide additional stability.

4.7 Characterization of Freeze-dried samples

Prior to performing loading studies, the NGs and hybrid NPs were freeze-dried as described in Section 3.2.6. The properties of the freeze-dried samples were compared with that of the aqueous samples. Figure 4.21 provides a comparison of the size and ZP of aqueous and freeze-dried NGs. Even though a slight increase could be observed in the size of the freeze-dried NGs, the maximum increase observed was ~ 9 % (for AAc:25 ratio), which was considered insignificant (due to variations observed within a particular NG composition in Figure 4.3(a)).

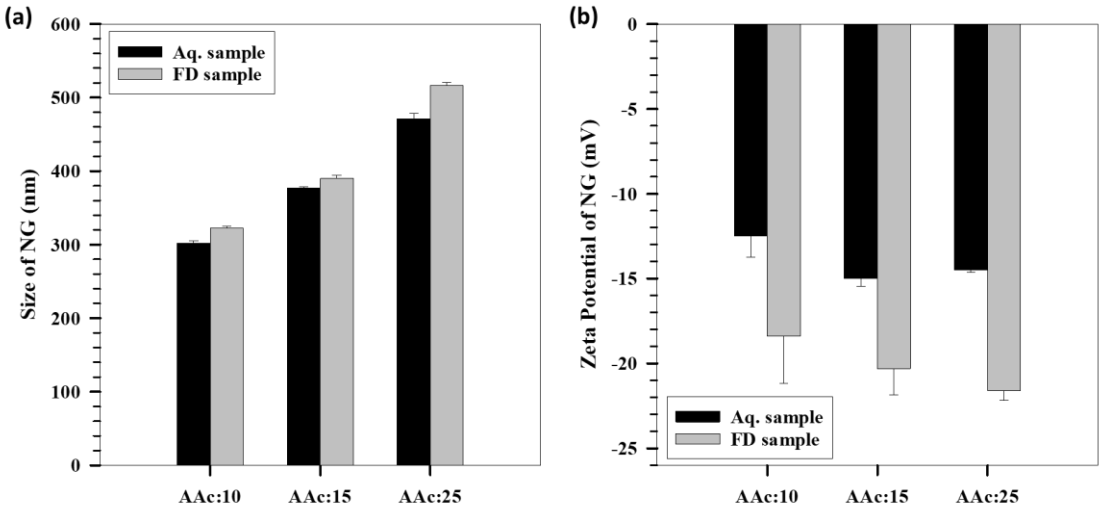

Figure 4.21: Comparison of (a) size, and (b) ZP of aqueous and freeze-dried NGs.

ZP of the freeze-dried sample showed a significant increase in the absolute value when compared to that of aqueous sample. However, the ZPs at 45°C (not shown in Figure) were found similar for both samples, which implies that the total charge density per particle does not change. The increase in ZP at 25°C could be a result of few AAc units within the polymer matrix being exposed to the surface during freeze-drying.

Similar observations were also made for freeze-dried samples of hybrid NPs as shown in Figure 4.22. Except for the sample with AAc:15, which showed an insignificant increase in size of ~ 5% for the freeze-dried sample, other samples were found to have similar sizes to the aqueous ones.

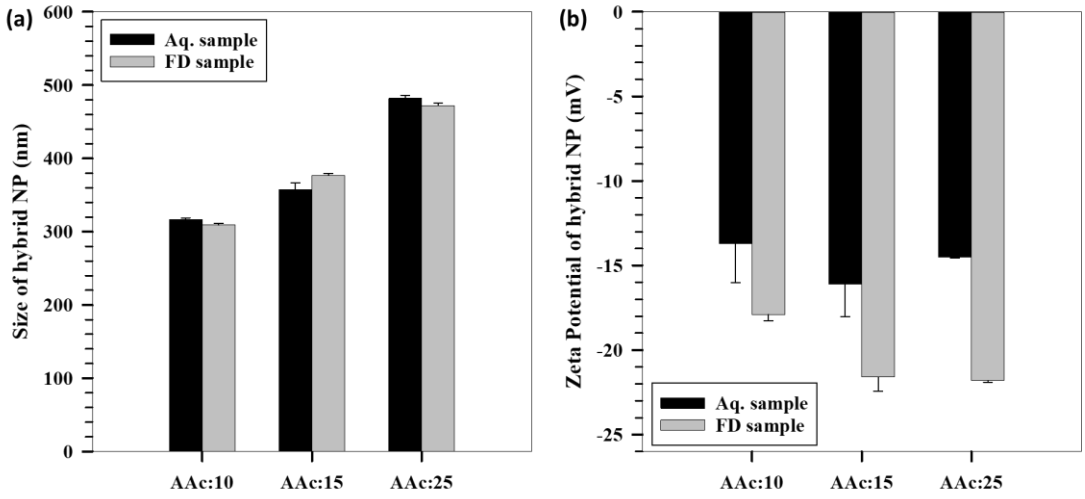

Figure 4.22: Comparison of (a) size, and (b) ZP of aqueous and freeze-dried hybrid NPs.

Figure 4.23 provides a comparison of VCEs of aqueous and freeze-dried NGs/hybrid NPs. It can be observed that the freeze-dried samples have a higher VCE than the aqueous sample for both NGs and hybrid NPs. This was observed at all three molar ratios of AAc. This could be due to removal of loosely bound surfactants (which are still present after dialysis) by freeze drying which enhances the VCE.

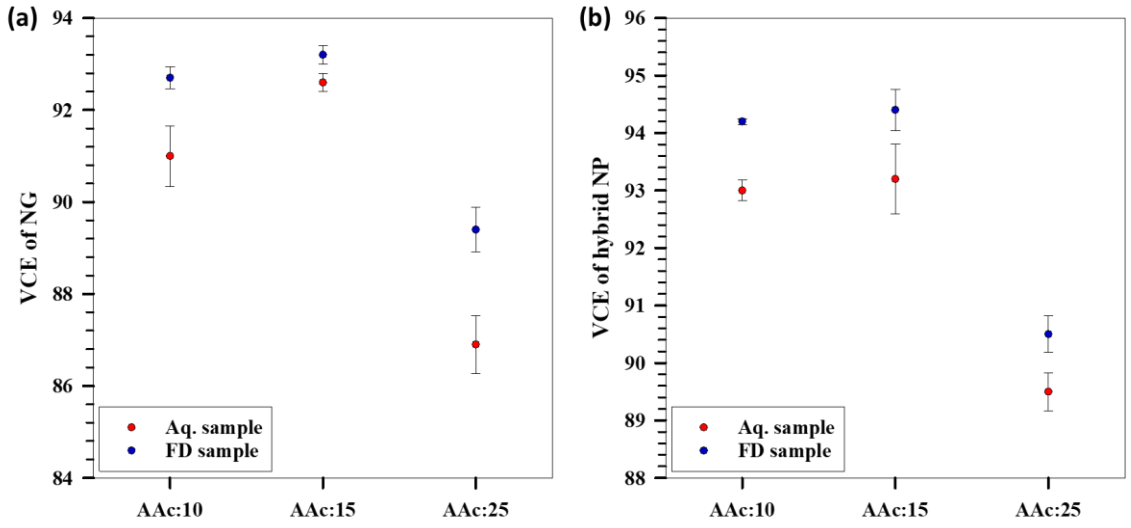

Figure 4.23: VCE comparison of aqueous and freeze-dried (a) NGs (b) hybrid NPs.

4.8 Loading studies

Loading studies were performed on NGs and hybrid NPs using breathing-in technique as described in Section 3.2.8. To 1.7 mg of the freeze-dried sample, 2 ml of 0.5 mg/ml Cyt C was added and kept on shaking for 2 hours. Two different procedures were followed to expel free Cyt C from the loaded system. These loading efficiencies obtained from these methods were compared in order to study their effectiveness.

The first method involved dialysis of the loaded sample in water buffer. The dialysis time is an important parameter to ensure complete removal of free Cyt C. In order to find out the time it takes for complete removal of free Cyt C, a solution of Cyt C of known concentration was dialysed over time. The absorbance value was noted before the start of dialysis and the decrease in absorbance as a function of dialysis time was obtained. By using a calibration curve for Cyt C (Figure 4.24(a)), this decrease in absorbance could be used to predict the concentration of Cyt C within the dialysis tube, thereby giving a measure of drug that has diffused out. This was used to obtain the percentage removal of Cyt C (shown in Appendix E) as a function of time (Figure 4.24(b)). From Figure 4.24(b), it could be observed that ~ 98% of the drug was expelled

out of the dialysis tube with ~ 3 hours of dialysis. However, to ensure complete removal of free Cyt C from the loaded systems, dialysis was performed for a period of 24 hours.

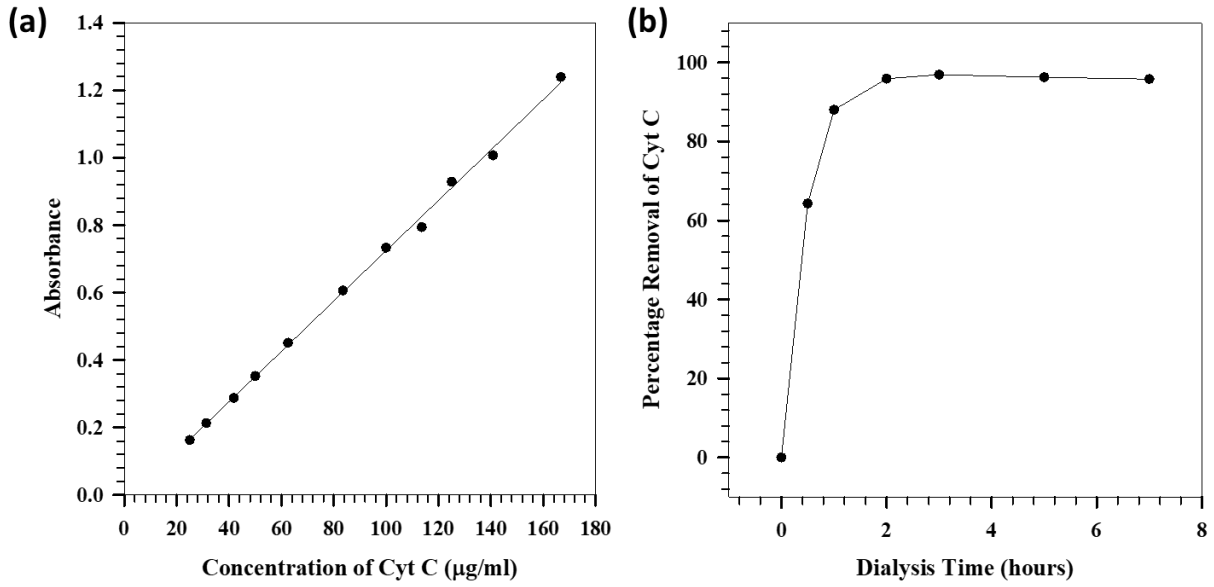

Figure 4.24: (a) Calibration curve of Cyt C; (b) Percentage removal of free Cyt C as a function of dialysis time.

Hence, 2 ml of the loaded samples were put on 24 hours dialysis post shaking for 2 hours. Figure 4.25 shows the post dialysis images of drug loaded NG/hybrid NP samples with different AAc mole ratios. From the figure, drug loaded solutions of both bare NGs and hybrid NPs were observed to show stronger colour with increasing AAc content. This could probably indicate higher loading efficiencies with increased AAc content. These solutions were further diluted, and the absorbance was measured using UV-Vis spectrophotometer. This would give a measure of bound Cyt C after the free drug has diffused out through the dialysis membrane. The loading efficiencies (LEs) were calculated by comparing the absorbance values with that of the initial drug incorporated at similar dilution (shown in Appendix F).

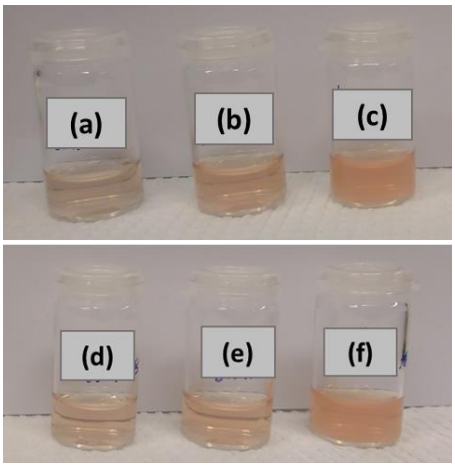

Figure 4.25: Loaded samples post dialysis. (a) bNG_10 (b) bNG_15 (c) bNG_25 (d) hNP_10 (e) hNP_15 (f) hNP_25.

Though free Cyt C was observed to leave the system by performing dialysis, this procedure was found to stain the dialysis tubes. This could be a result of Cyt C molecular weight (12.3 kDa) being close to the MWCO of the dialysis tube (14kDa). The staining effect on the tubes can be seen in Figure 4.26. More staining could be observed at lower molar ratios of AAc and showed a gradual decrease with increase in AAc content. Similar observations made in both NGs and hybrid NPs were in concurrence with the loading efficiencies observed from Figure 4.25. Since NGs/hybrid NPs at low AAc content were observed to show low LEs, these systems would contain increased concentration of free drug. Increased diffusion of free drug through the dialysis tube would lead to increased staining compared to systems having high LEs (AAc:25).

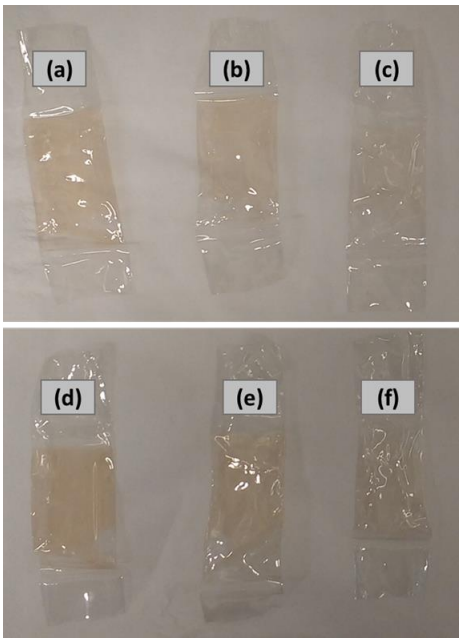

Figure 4.26: Staining observed in tubes post dialysis. (a) bNG_10 (b) bNG_15 (c) bNG_25 (d) hNP_10 (e) hNP_15 (f) hNP_25.

The presence of stains on the dialysis tube might affect the rate of diffusion of free Cyt C through the membrane. Hence a different technique involving centrifuging was also performed to remove free Cyt C from loaded systems. In this method, the loaded samples were transferred to Eppendorf tubes post shaking and centrifuged at 14500 rpm for 10 minutes. Figure 4.27 shows the drug loaded hybrid NP samples with different compositions before and after spinning the particles. It can be observed that the supernatant of the sample containing low mole ratio of AAc (hNP_10) had a stronger colour when compared to other ratios. The colour was also observed to get pale with increasing AAc mole ratios in the sample. This again confirms the previous observations made from dialysis that LEs increase with increasing molar ratios of AAc in the samples.

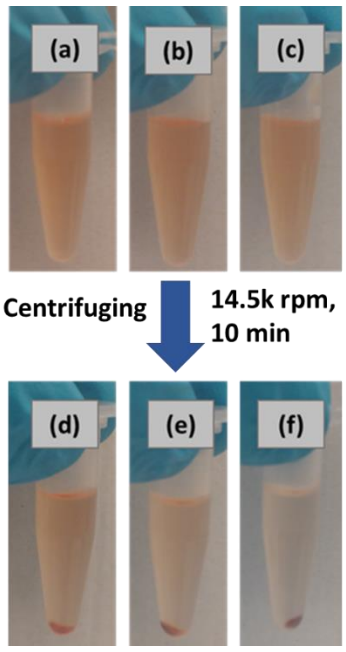

Figure 4.27: Cyt C loaded hybrid NP samples before and after centrifuging (a,d) hNP_10 (b,e) hNP_15 (c,f) hNP_25.

After separating the supernatant, both supernatant and precipitate were diluted sufficiently. Figure 4.28 shows supernatants and bottom precipitates of Cyt C loaded hybrid NP samples with 2.5x dilution. It can be observed from Figure 4.28(d,e,f) that the diluted solutions of bottom precipitates showed stronger colour with increasing mole ratio of AAc, thereby confirming the increased loading of Cyt C.

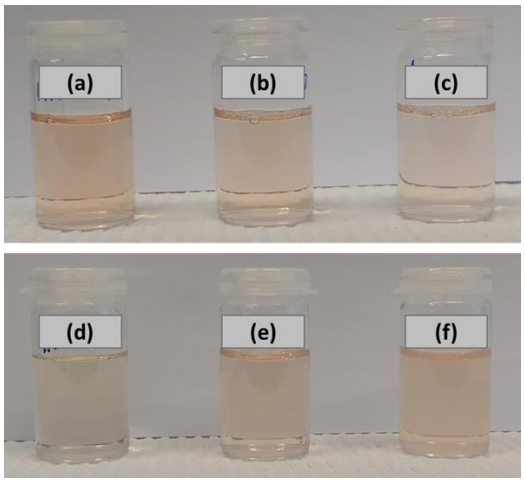

Figure 4.28:(a,b,c) Supernatant (2.5x dilution) of Cyt C loaded hybrid NPs (AAc:10, 15, 25 arranged from left to right); (d,e,f) Bottom precipitate (2.5x dilution) of Cyt C loaded hybrid NPs (AAc: 10, 15, 25 arranged from left to right).

The LEs were calculated by measuring the absorbance of diluted bottom precipitate and comparing it with the absorbance of free drug at same dilution (Shown in Appendix F). Figure 4.29 provides a comparison of LEs obtained using dialysis and spinning methods. As discussed previously, the LEs were found to increase with increasing molar ratios of AAc. This could be attributed to larger pore dimensions at higher AAc content (discussed in Section 4.3.2), thereby enabling more diffusion of drug through the pores, which would result in higher loading. However, no significant changes in LEs were observed between NGs and hybrid NPs having the same composition. Previous studies in literature performed using similar drug and NG/hybrid NP concentrations, have reported coated hybrid NPs to have a lower LEs when compared to bare NGs [15]. From Figure 4.29, highest deviations in LEs obtained from the two methods were observed to be ~13% at high AAc mole ratio (AAc:25). Hence, these methods were found to be comparable at the three molar ratios of AAc. However, due to shorter time requirements and easiness of the technique, spinning method was used for further studies.

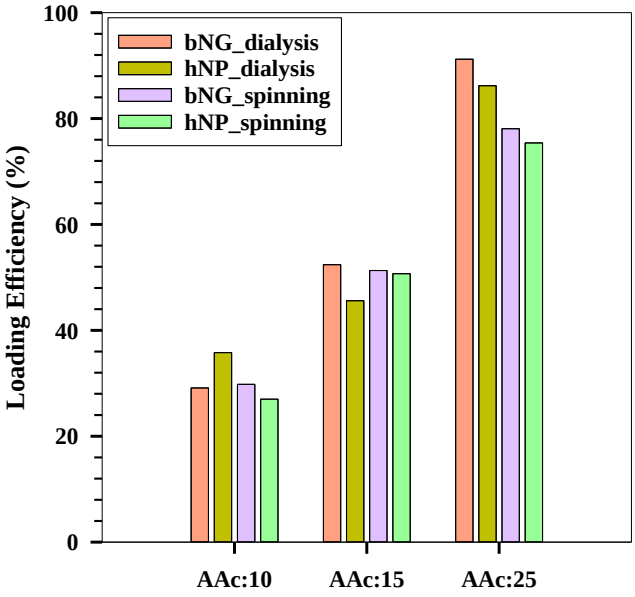

Figure 4.29: Comparison of LEs obtained by dialysis and spinning methods.

In order to capture the variations within the spinning technique, three repeats of loading studies were performed, and free Cyt C was separated via centrifuging. The LEs obtained from the three repeats have been shown in Figure 4.30(a). An average standard deviation ~19% was observed at low AAc content (AAc:10), whereas a lower deviation (~9%) could be seen at higher AAc ratios (AAc:25). This could be a result of experimental errors associated while separating the supernatant after centrifuging. Drug loaded samples with high mole ratio of AAc were bigger in size and heavier compared to the loaded samples with low AAc. Hence, separating the supernatant in these samples were easier than those having low mole ratios of AAc.

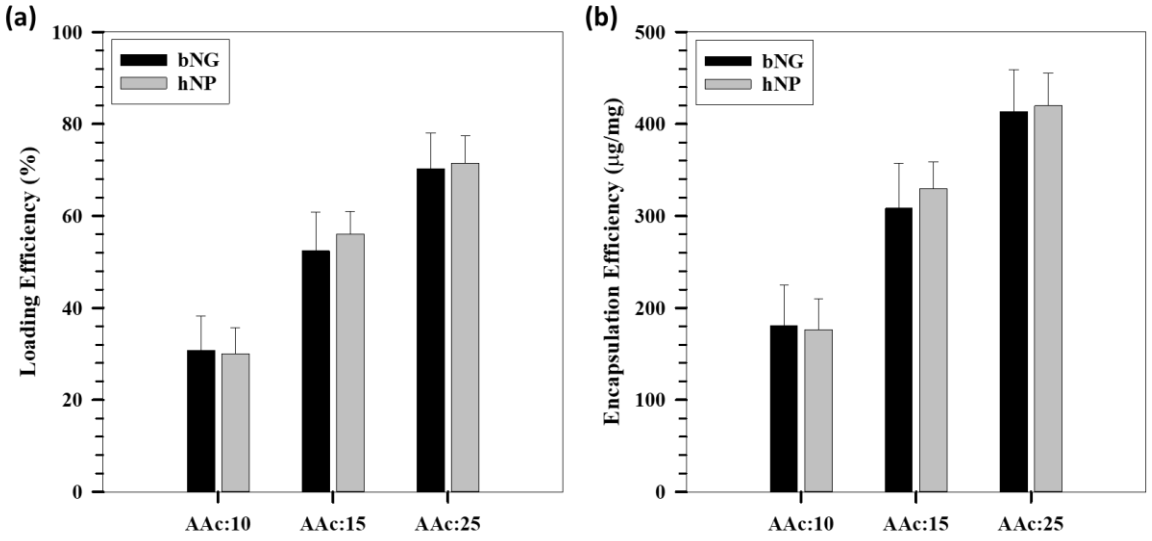

Figure 4.30: (a) LEs as a function of increasing AAc content (b) EEs as a function of increasing AAc content.

Encapsulation efficiency (EE), which gives the amount of drug encapsulated per unit weight of the nanocarrier system, was also calculated (Appendix F). Since the amount of drug and NG/hybrid NP were kept constant throughout the loading studies, the EE was directly proportional to the LE and hence showed a similar trend. Figure 4.30(b) shows the EEs of the NGs and hybrid NPs as a function of varying NG compositions (AAc mole ratios). Table 4.2 lists the loading and encapsulation efficiencies obtained for different NGs and hybrid NPs.

Sample	LE (%)	EE (µg/mg)
bNG_10	30.8 ± 7.4	181 ± 44
bNG_15	52.4 ± 8.4	308 ± 49
bNG_25	70.3 ± 7.8	414 ± 46
hNP_10	30.0 ± 5.7	176 ± 33
hNP_15	56.0 ± 5.0	330 ± 29
hNP_25	71.4 ± 6.0	420 ± 35

Table 4.2: LEs and EEs of different NGs/hybrid NPs.

4.9 Drug Release studies

Release studies of Cyt C were performed on the loaded NGs/hybrid NPs by using a dialysis setup as described in Section 3.2.9. The loaded samples were centrifuged, and the bottom precipitate was diluted sufficiently. This was then transferred into dialysis tubes and placed in the release medium. The initial release profile was monitored at a low pH 3 for a span for 32 hours. This was followed by increasing the temperature of the release medium to 40^{o}C to aid in

further release of the drug. A measure of drug release was obtained by monitoring the decrease in absorbance peak of Cyt C as a function of time.

Prior to performing release studies, pH of the diluted samples of loaded NGs/hybrid NPs were measured and found to be ~ 5.3. This ensured that the NGs/hybrid NPs were in a swelled state prior to release. ZPs of the diluted samples were also measured and were observed to have higher absolute values compared to the freeze-dried samples prior to loading. This is shown in Figure 4.31.

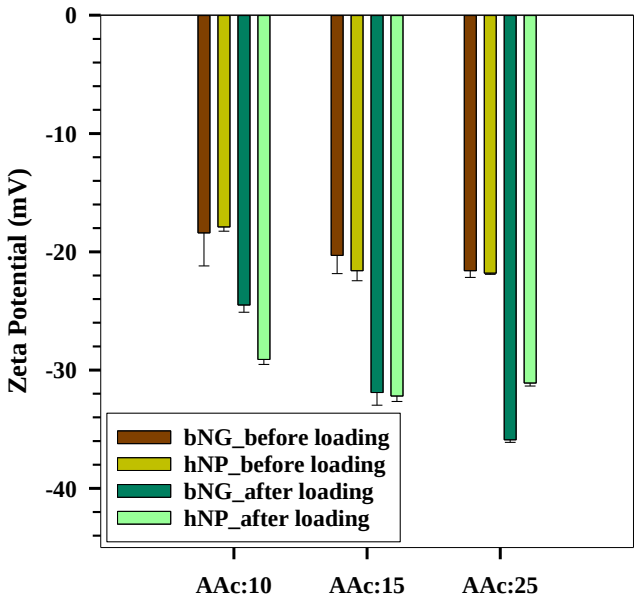

Figure 4.31: ZP of NGs/hybrid NPs before and after loading Cyt C.

The higher ZP for loaded samples would indicate higher stability which could be due to the formation of a stable complex between the drug and the NG/hybrid NP. Figure 4.32 shows the release profile of Cyt C from the NG/hybrid NP systems at low pH (pH 3). The release profile in the first two hours was conducted as a separate study in order to capture more time points. These values have been incorporated in to the larger study conducted for 32 hours and an average value of the drug released was taken at the common time points.

An initial burst release could be observed for AAc:10 and AAc:25 systems. A plausible explanation for this would be a sudden change in the external pH, causing partial collapse of the NGs/hybrid NPs. A low pH would favour the AAc units to be in protonated state, thereby leading to reduced hydrophilic interactions and partial collapse of the system. An average release of ~19% and ~17% were observed within one hour in AAc:10 and AAc:15 systems respectively. However, no significant differences could be observed in the release profiles of

bare NGs and hybrid NPs with the same AAc composition. Few precipitates could be observed in the tubes of NGs/hybrid NPs with AAc:15 around 29 hrs into dialysis. This was associated with a decrease in drug release for these systems as observed from Figure 4.32. This could probably indicate the samples getting unstable with longer durations at a low pH.

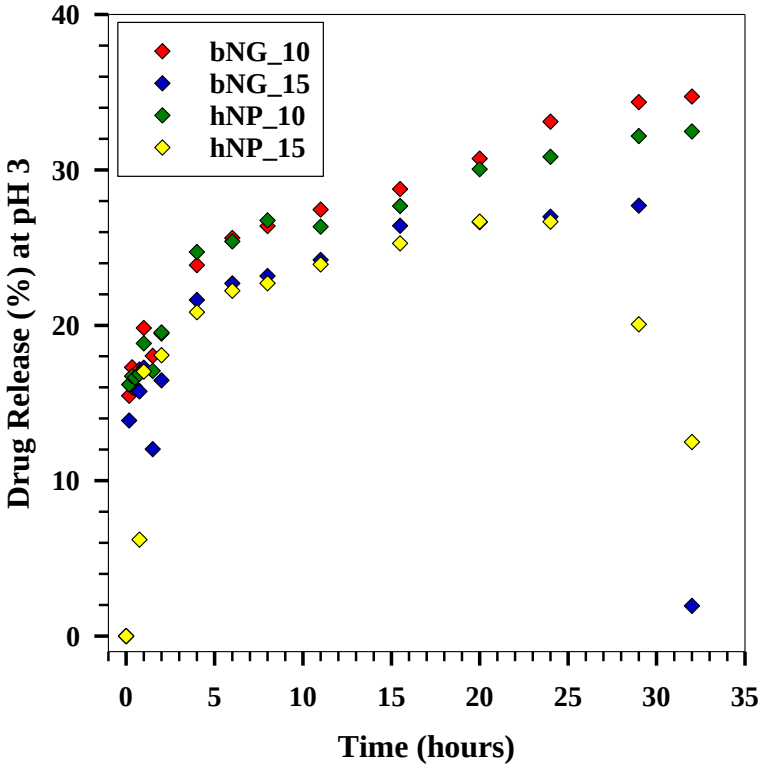

Figure 4.32: Cyt C release profile from bare NGs and hybrid NPs at pH 3.

NG/hybrid NP systems with high AAc (AAc:25) were observed not to show any release at pH 3. This could be due to increased stability of the complex formed with the drug as observed from Figure 4.31. However, precipitates could be observed inside the dialysis tube for these samples (AAc:25) few hours into dialysis, which hints to the fact that the samples were unstable at pH 3. NGs/hybrid NPs with AAc:25 are bigger in size compared to other ratios. This could also indicate bigger pore sizes and void volume leading to more internal location of the drug. For effective release, the drug would have to initially diffuse from matrix to the bulk inside the dialysis tube, followed by diffusion through the membrane. Higher porosities in AAc:25 systems could limit the initial diffusion process, leading to ineffective release of the drug. Whereas, due to smaller sizes of samples with AAc:10 and AAc:15, there could be a higher fraction of the drug located near to the surface, leading to effective diffusion out from the system.

Since not much release could be observed at later time points, the dialysis was stopped at 32 hours, and all samples were taken out from the release medium. pH of the medium was still observed to be at 3. The samples were put back after raising the temperature of release medium to 40^{o}C. Since the absorbance values show an increase with collapse at 40^{o}C, (due to solution becoming turbid leading to increased refractive index) an equilibration time of 10 minutes was provided before measuring the new baseline values for these samples. It was hence assumed that there was no significant release during the first ten minutes after raising the temperature. Figure 4.33 shows the additional release obtained in these samples with an added stimulus. At 40^{o}C, the samples would collapse completely, causing the drug to move out due to shrinkage of the pores.

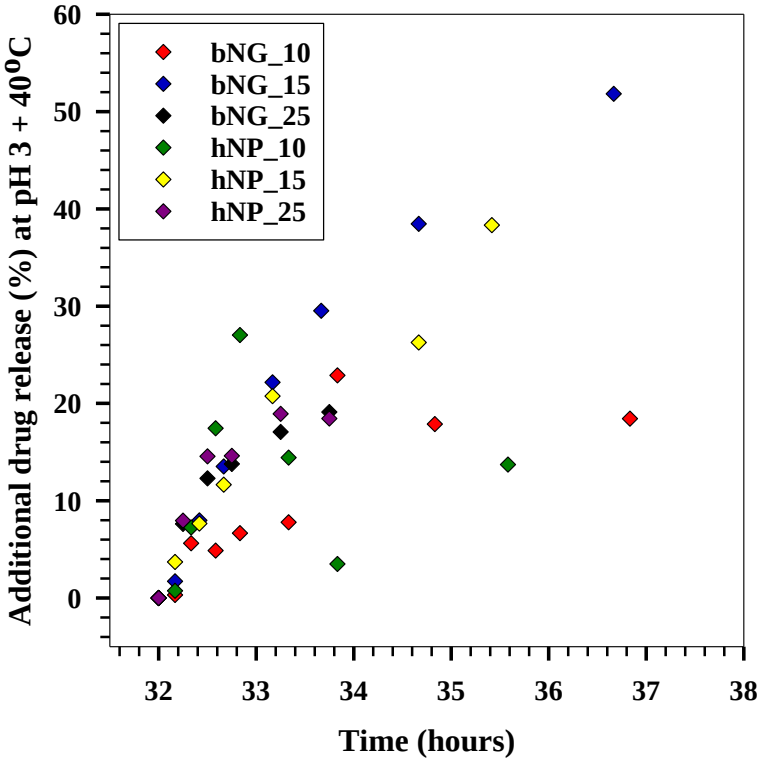

Figure 4.33: Additional release of Cyt C from bare NGs and hybrid NPs by increasing the temperature to 40^{o}C without altering the pH from initial study(pH = 3).

NG/hybrid NP samples with AAc:25 were also found to show release at these conditions. This observation could probably substantiate the hypothesis that the drug is located in the interior of the nanocarrier (for AAc:25) and hence required an additional stimulus to cause complete collapse, leading to drug release.

Different mathematical models have been developed which could be used as effective tools to analyse the kinetics of release from these NG/hybrid NP systems [89, 90]. This would provide

a better understanding on the actual release kinetics and transport mechanism. Few models which have been used in this study are discussed here.

Zero order model, as the name suggests is obtained using the principles of zero-order kinetics. Polymer systems that follow these kinetics release the drug at a constant rate, thereby maintaining a constant drug level in blood throughout the delivery [90]. Hence, this model depicts a direct relationship between the fraction of drug released and time. Zero order model is defined by Equation (5).

$$F = K_0 t \tag{5}$$

where F is the cumulative fraction of drug released in time t, and K_0 is the zero-order rate constant. First order release model represents a linear relationship between the logarithm of the fraction of drug within the nanocarrier and time as shown by Equation (6)

$$\ln(1 - F) = -K_1 t \tag{6}$$

where K_1 denotes the first order rate constant. Higuchi model can be described by a linear relationship between the cumulative fraction of drug released and square root of time.

$$F = K_H \sqrt{t} \tag{7}$$

where K_H is the Higuchi dissolution constant. Besides these models, a power law equation developed by Korsmeyer and Peppas, can be used to describe drug transport mechanism through polymeric matrix. An expression for this is given by Equation (8)

$$F = K_{kp} t^n \tag{8}$$

where K_{kp} is a constant which incorporates structural and geometric information of the nanocarrier system, and n is the release exponent, which indicates the drug release mechanism as shown in Table 4.3 [89]. The release exponent can be obtained from the slope of a plot between $\ln(F)$ and $\ln(t)$.

$$\ln(F) = \ln K_{kp} + n\ln(t) \tag{9}$$

Release Exponent (n)			Drug Release Mechanism
Thin Film	**Cylinder**	**Sphere**	
0.5	0.45	0.43	Fickian diffusion
0.5 < n < 1	0.45 < n < 0.89	0.43 < n < 0.85	Anomalous transport
1	0.89	0.85	Case-II transport

Table 4.3: Drug release mechanisms from different geometries based on the values of release exponent.

Fickian diffusion (Case-I transport) is described by a diffusion coefficient, while Case-II transport is described by a relaxation constant which accounts for the swelling-collapse behaviour of the drug delivery system. Anomalous transport lies intermediate between Fickian diffusion and Case-II transport [91].

Zero order, First order, Higuchi and Power law models were used to study the kinetics of Cyt C release from the NG/hybrid NP systems. These models were fitted separately for the initial 32 hours of pH driven release and the release with combined stimuli (pH + Temperature).

Figure 4.34 shows the fitted models on bNG_10 sample for studies performed at pH 3. Higuchi model was found to give the best fit with a R^2 value of 0.9888 and dissolution constant, K_H = 0.1734 $h^{-0.5}$. From the power law model, the release exponent was found to be 0.526.

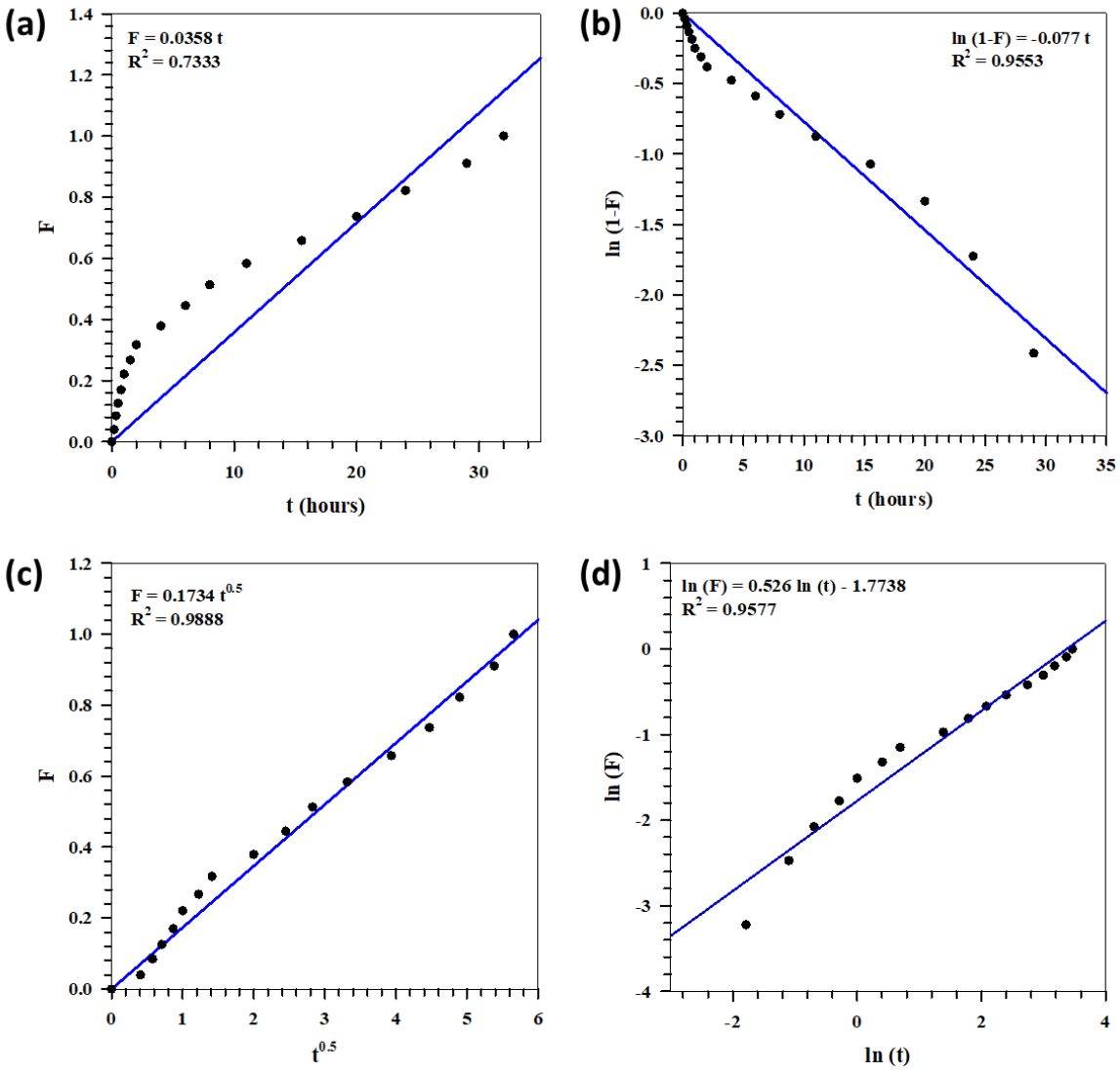

Figure 4.34: Fitting release models in bNG_10 sample for studies performed at pH 3. (a) Zero order model (b) First order model (c) Higuchi model (d) Power law model.

Similarly, release models were fitted to hNP_10, bNG_15 and hNP_15 samples (shown in Appendix H). From the model fitting, it could be observed that all samples that showed a release, followed Higuchi kinetics. The time taken for releasing 50 % of the drug ($t_{1/2}$) was calculated using Higuchi model by substituting F = 0.5. These values along with the Higuchi dissolution constants have been listed in Table 4.4. Insignificant changes observed in the $t_{1/2}$ of these samples, denote that these polymeric devices release similar quantities of drug over time.

Sample	Release Model	Higuchi dissolution constant, K_H ($h^{-0.5}$)	$t_{1/2}$ (hours)
bNG_10	Higuchi	0.1734	8.3
hNP_10		0.1752	8.1
bNG_15		0.1875	7.1
hNP_15		0.1673	8.9

Table 4.4: Release Model, Higuchi dissolution constant and $t_{1/2}$ for bNG/hNP systems at pH 3.

Table 4.5 summarizes the release exponent, geometry of nanocarrier and transport mechanism involved in the release.

Sample	Release exponent (n)	Geometry	Transport mechanism
bNG_10	0.526	Sphere /Cylinder	Anomalous transport
hNP_10	0.5179		
bNG_15	0.5104		
hNP_15	0.7141		

Table 4.5: Release exponent and transport mechanism shown by bNG/hNP samples at pH 3.

From the Table, it can be observed that the release exponents for all samples were fairly similar. The value of release exponent indicated an anomalous transport mechanism for all samples. Since a low pH of 3 would only cause partial collapse of the drug device, the drug would still have to diffuse through the matrix to leave the system. Therefore, the NG/hybrid NP matrix was assumed to have a spherical/cylindrical geometry rather than thin film geometry. The model fitting done for the samples at multiple stimuli release conditions (pH 3 + 40°C) have been discussed next.

Figure 4.35 shows the fitted models on bNG_10 sample for studies performed at pH 3 and 40°C. Zero order model gave the best fit with a $R^2 = 0.9497$ and $K = 0.2325\ h^{-1}$. The release exponent was obtained from the slope of Power law model and was found to be 1.5138.

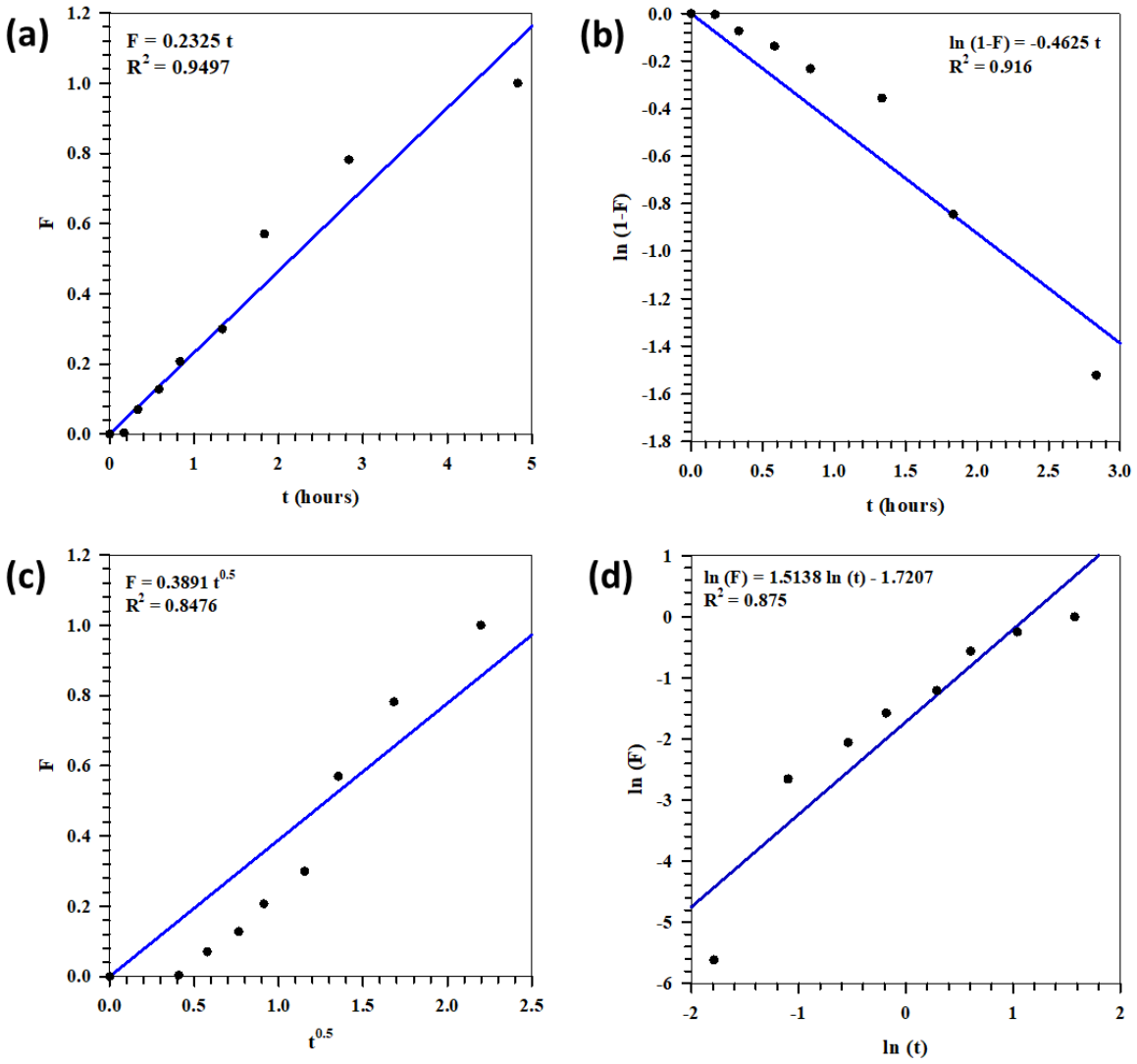

Figure 4.35: Fitting release models in bNG_10 sample for studies performed at pH 3 + 40°C. (a) Zero order model (b) First order model (c) Higuchi model (d) Power law model.

Figure 4.36 shows the fitted models on hNP_10 sample for studies performed at pH 3 and 40°C. First order model gave the best fit with a R^2 = 0.9411 and K = 1.0301 h^{-1}. The release exponent was obtained from the slope of Power law model and was found to be 1.4927.

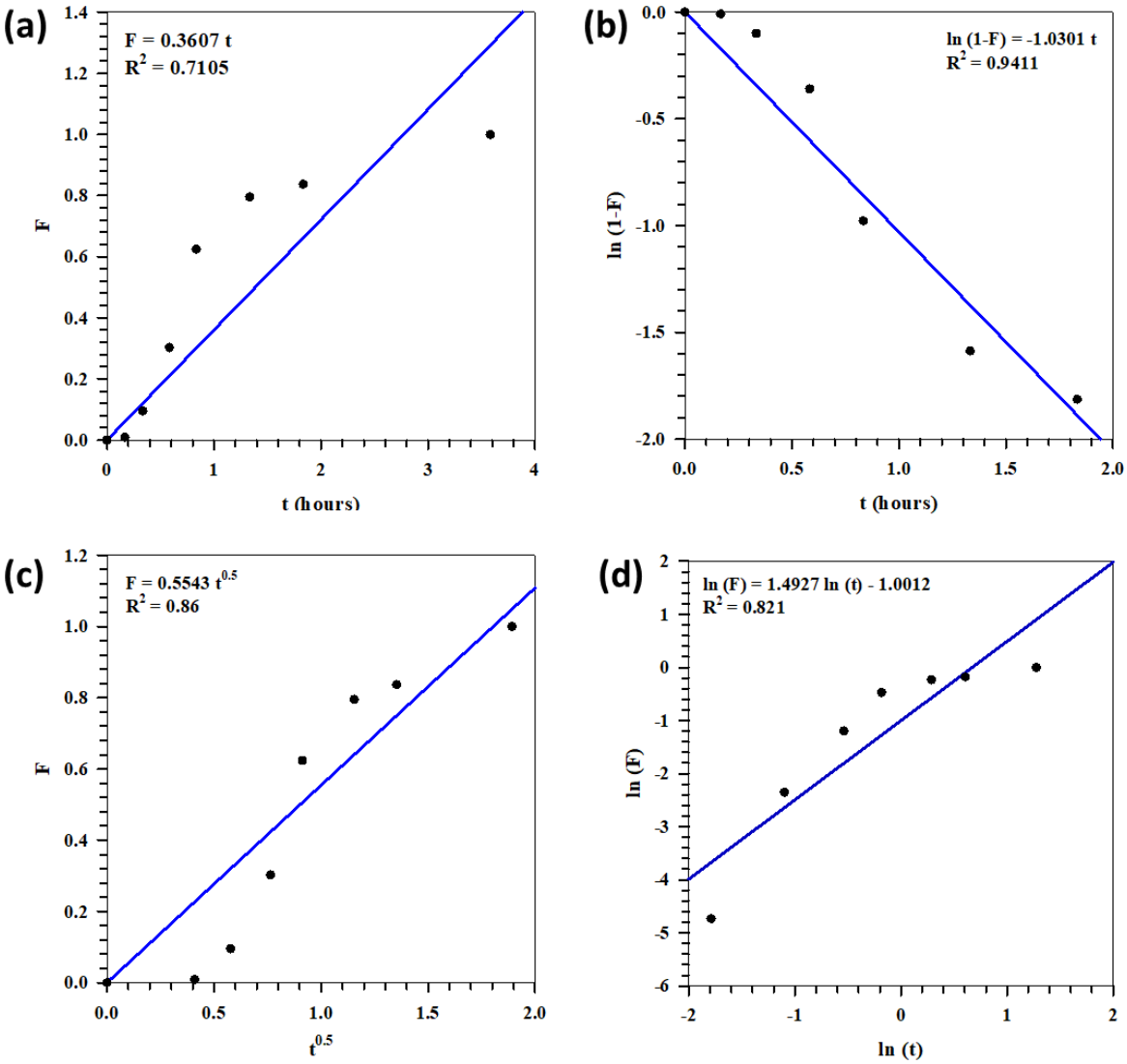

Figure 4.36: Fitting release models in hNP_10 sample for studies performed at pH 3 + 40ºC. (a) Zero order model (b) First order model (c) Higuchi model (d) Power law model.

Similarly, release models were fitted for other samples (shown in Appendix I).

Table 4.6 summarizes the release model, rate constant and $t_{1/2}$ obtained from model fitting. bNG_25 and hNP_25 were observed to have the similar K, which indicated the presence of NPs not to influence the release kinetics of these systems. As discussed before, this could be due to the bigger sizes of bNG/hNP with AAc:25 when compared to the size of Au NPs incorporated. However, hNP_10 and hNP_15 were observed to have different K values when compared to the corresponding NGs. This could be due to the shift in kinetics observed from zero order to

first order in these cases with the incorporation of NPs. But since the $t_{1/2}$ of these systems were similar, it could be concluded that presence of NPs does not show significant effect on the release of drug.

Sample	Release Model	Rate constant, K ($hour^{-1}$)	$t_{1/2}$ (hours)
bNG_10	Zero order	0.2325	2.15
hNP_10	First order	1.0301	0.67
bNG_15	Zero order	0.2284	2.19
hNP_15	First order	0.3931	1.76
bNG_25	Zero order	0.5799	0.86
hNP_25	Zero order	0.5895	0.85

Table 4.6: Release Model, rate constant and $t_{1/2}$ for bNG/hNP systems at pH 3 + 40°C.

Sample	Release Exponent (n)	Geometry	Transport Mechanism
bNG_10	1.5138	Thin Film	Super Case-II
hNP_10	1.4927		Super Case-II
bNG_15	1.3769		Case-II
hNP_15	1.0803		Case-II
bNG_25	1.1292		Case-II
hNP_25	1.1372		Case-II

Table 4.7: Release exponent and transport mechanism for bNG/hNP systems at pH 3 + 40°C.

It can be noted from Table 4.7, that the release exponents are higher than that observed in case of release controlled by pH alone (Table 4.5). This could be explained by the change in geometry of the NG/hybrid NP system with additional temperature stimuli. The matrix was assumed to have a spherical/cylindrical geometry during initial release conditions at pH 3. Increasing the temperature of the release medium to 40°C, leads to complete collapse of the NG/hybrid NP thus shifting the geometry to a thin film. This would reduce the diffusion path of the drug, thereby leading to more effective release of the drug. From Table 4.7, it can also be noted that, the release exponents were fairly similar for NGs and hybrid NPs having same AAc mole ratio. However, a small decrease in the release exponent values could be observed at higher AAc mole ratios. This could indicate that even though the presence of Au NPs in the hybrid does not affect the release of the drug, increasing AAc mole ratio is an important

parameter controlling release. As discussed previously, higher AAc mole ratios would probably give rise to NGs/hybrid NPs with higher porosities, leading to more internal location of the drugs. Since the drug molecules were observed to form stable complexes with the nanocarrier (Figure 4.31), internal location of the drug could limit its diffusion to the surface of the nanocarrier.

5 Conclusion

This work aimed at studying the growth and physico-chemical properties of multifunctional NPs. Multifunctional NPs were synthesized by combining Au NSs with temperature and pH sensitive pNIPAm-AAc NGs. Incorporating Au NSs into the NGs were observed to provide enhanced properties to the hybrid, stemming from plasmonic attributes of Au NS in addition to pH and temperature sensitivities of the NG.

Initial part of this work dealt with the synthesis of Au NSs of various sizes and surface charges. These were synthesized using modified-Turkevich method and seed mediated growth method. This was followed by the synthesis of pNIPAm-AAc NGs using a procedure which was previously developed in Ugelstad Laboratory [19, 79]. The synthesized particles were characterized using techniques such as UV-Vis spectroscopy, DLS, and S(T)EM.

Three different mole ratios of the monomers were used to synthesize NGs having different physico-chemical properties. The sizes of the NGs showed an increase with increasing molar ratio of AAc, with sizes ranging from 318 ± 26 nm at AAc:10 to 462 ± 23 nm at AAc:25. Samples with higher molar ratios of AAc were also associated with a drop in VCE due to increased hydrophilic interactions of the carboxylic group. The effect of reaction medium pH on the properties of the NG was studied by varying the pH of SDS solution in the synthesis process. Low pH (3) conditions were observed to favour the growth of larger NGs.

Hybrid NPs were prepared by in situ polymerization method in which the NPs dispersed in the SDS solution were added to the reaction mixture. The effect of concentration, size and surface charge of the NPs on the properties of the resulting hybrid were analysed. Increased concentration of NPs showed an increase in VCE of the hybrid. However, no significant changes in the properties of the hybrid could be observed with changes in size and surface charge of the NP. The NGs were hypothesized to have larger pore dimensions compared to the size of NPs, leading to internal location of NPs in the matrix. A weight of 0.75 mg Au NS was found to give prominent LSPR peak of Au, thereby enabling easy detection in addition to enhanced physico-chemical properties of the hybrid.

The swelling -collapse properties of hybrid NPs as a function of temperature and pH were compared to that of bare NGs at different mole ratios of AAc. NGs/hybrid NPs with higher AAc content were observed to show rapid response to temperature when cycled through the VPTT. The VPTT was hypothesized to be influenced by pore size and porosities of the NG/hybrid NP matrix in addition to hydrophilic interactions of AAc units. The pH response of

NG/hybrid NP systems were studied by varying the pH of the samples from 3 to 9. A small collapse (~55%) of the NG/hybrid NP could be observed at low pH due to reduced hydrophilic interactions brought about by protonation of AAc units. At high pH, the hybrid NPs were observed to swell to a lower extent compared to bare NGs which was suggested to be a result of enhanced hydrophobic interactions brought about by the incorporation of NPs in the NG matrices. Swelling characteristics observed at high pH, for NGs/hybrid NP samples maintained above VPTT, indicated pH to have more significant effect on the system.

From time-based studies performed to understand the growth, a rapid initial increase could be observed in the sizes of NGs/hybrid NPs followed by stabilization. The hybrid NPs were found to stabilize at a lower size compared to bare NGs. Though NGs/hybrid NPs showed similar growth curves, it was suggested that they might follow different kinetics.

Loading studies with Cyt C were performed on NGs/hybrid NPs using breathing-in technique. Two different methods (dialysis and centrifuging) were studied to expel free Cyt C from the loaded systems. The loaded samples showed increased stability compared to the freeze-dried samples hinting to the formation of a stable complex between Cyt C and the nanocarrier. The LEs were found to increase for both NGs/hybrid NPs with increase in AAc mole ratio. The values of LEs ranged from ~30% at AAc:10 to ~71% at AAc:25. This was hypothesized to be a result of larger pore dimensions at higher AAc content, thereby enabling more diffusion of drug through the pores. However, no significant differences could be observed in the LEs of NGs and hybrid NPs having the same composition. The EEs were also observed to increase with AAc content and had values ranging from ~180 µg/mg (AAc:10) to ~417 µg/mg (AAc:25).

Finally, drug release profiles of bare NGs and hybrid NPs were studied at different release conditions. At pH 3, a release of ~34% and ~26% could be observed for AAc:10 and AAc:15 systems respectively. However, AAc:25 systems showed no release at low pH. An additional temperature stimulus at 40°C was observed to cause release from all systems. The release exponents were higher at multi-stimuli release conditions (pH 3 + 40°C) than at pH 3. This was attributed to the change in matrix geometry from spherical/cylindrical to thin film, as the NG/hybrid NP undergoes complete collapse in presence of additional temperature stimuli. The transport mechanism of the drug was also observed to switch from anomalous to case-II/super case-II transport on adding temperature stimuli.

6 Future work

The observations made from this study, lead to a hypothesis that the pore sizes and porosities of NGs/hybrid NPs increase with increasing AAc mole ratio. Hence, using BET to analyse the pore size and porosities of freeze dried NG/hybrid NP samples could validate the hypothesis.

Replacing spherical Au NPs with anisotropic counterparts in the hybrids would be a novel field to delve into. The surface plasmon oscillations of anisotropic Au NPs, for instance Au nanorods, could be exploited and this could lead to sensitization of the stimuli sensitive polymeric gels by applying a electromagnetic field of a particular wavelength. Moreover, by tuning the size and shape of anisotropic Au NPs, the plasmon absorption can be shifted towards the near-infrared (NIR) region in which living tissues show minimum absorption.

Since the synthesis of hybrid NPs were associated with a fraction of NPs sticking to the magnet, it would be interesting to perform Thermogravimetric Analysis of these samples to obtain an idea of how much NPs actually goes into the hybrid. Though the effect of varying pH of medium on the properties of NGs have been studied, the study could be further extended by incorporating NPs into it and exploring the behavioural differences of the hybrids.

Furthermore, the growth of bare NGs and hybrid NPs could be monitored using UV-Vis spectrophotometer maintained at 70°C by performing time-based studies after initiating the reaction. This could be compared with the present findings to get a more comprehensive understanding of the underlying mechanism.

7 Bibliography

1. Li, Y., Y. Wu, and B.S. Ong, *Facile synthesis of silver nanoparticles useful for fabrication of high-conductivity elements for printed electronics.* Journal of the American Chemical Society, 2005. **127**(10): p. 3266-3267.
2. Daniel, M.-C. and D. Astruc, *Gold nanoparticles: assembly, supramolecular chemistry, quantum-size-related properties, and applications toward biology, catalysis, and nanotechnology.* Chemical reviews, 2004. **104**(1): p. 293-346.
3. Moisala, A., A.G. Nasibulin, and E.I. Kauppinen, *The role of metal nanoparticles in the catalytic production of single-walled carbon nanotubes—a review.* Journal of Physics: condensed matter, 2003. **15**(42): p. S3011.
4. Xiao, C., et al., *Nanostructured Gold/Bismutite Hybrid Heterocatalysts for Plasmon-Enhanced Photosynthesis of Ammonia.* ACS Sustainable Chemistry & Engineering, 2017. **5**(11): p. 10858-10863.
5. Latorre, M. and C. Rinaldi, *Applications of magnetic nanoparticles in medicine: magnetic fluid hyperthermia.* Puerto Rico health sciences journal, 2009. **28**(3).
6. Salata, O.V., *Applications of nanoparticles in biology and medicine.* Journal of nanobiotechnology, 2004. **2**(1): p. 3.
7. Sanvicens, N. and M.P. Marco, *Multifunctional nanoparticles – properties and prospects for their use in human medicine.* Trends in Biotechnology, 2008. **26**(8): p. 425-433.
8. Holowka, E.P. and S.K. Bhatia, *Controlled-Release Systems*, in *Drug Delivery*. 2014, Springer. p. 7-62.
9. Cheng, Z., et al., *Multifunctional Nanoparticles: Cost Versus Benefit of Adding Targeting and Imaging Capabilities.* Science, 2012. **338**(6109): p. 903-910.
10. Aguilar, M.R. and J. San Román, *Smart polymers and their applications*. 2014: Elsevier.
11. Xu, M.-m., R.-j. Liu, and Q. Yan, *Biological stimuli-responsive polymer systems: design, construction and controlled self-assembly.* Chinese Journal of Polymer Science, 2017: p. 1-19.
12. Lim, E.-K., B.H. Chung, and S.J. Chung, *Recent Advances in pH-Sensitive Polymeric Nanoparticles for Smart Drug Delivery in Cancer Therapy*. Current Drug Targets, 2018. **19**(4): p. 300-317.
13. Lee, K.Y. and D.J. Mooney, *Hydrogels for Tissue Engineering.* Chemical Reviews, 2001. **101**(7): p. 1869-1880.
14. Bandyopadhyay, S., et al., *Incorporation of Fe@Au nanoparticles into multiresponsive pNIPAM-AAc colloidal gels modulates drug uptake and release.* Colloid and Polymer Science, 2016. **294**(12): p. 1929-1942.
15. Bandyopadhyay, S., A. Sharma, and W. Glomm, *The Influence of Differently Shaped Gold Nanoparticles Functionalized with NIPAM-Based Hydrogels on the Release of Cytochrome C.* Gels, 2017. **3**(4): p. 42.
16. Kratz, K., T. Hellweg, and W. Eimer, *Influence of charge density on the swelling of colloidal poly(N-isopropylacrylamide-co-acrylic acid) microgels.* Colloids and Surfaces A: Physicochemical and Engineering Aspects, 2000. **170**(2): p. 137-149.

17. Pelton, R., *Temperature-sensitive aqueous microgels.* Advances in Colloid and Interface Science, 2000. **85**(1): p. 1-33.

18. Bandyopadhyay, S., et al., *Influence of polymer coating on release of l-dopa from core-shell Fe@ Au nanoparticle systems.* Colloid and Polymer Science, 2017. **295**(2): p. 391-402.

19. Chakraborty, R., *Smart Polymeric Nanoplatform for Environmental Applications.* Specialization Project NTNU, 2017.

20. Khlebtsov, N. and L. Dykman, *Biodistribution and toxicity of engineered gold nanoparticles: a review of in vitro and in vivo studies.* Chemical Society Reviews, 2011. **40**(3): p. 1647-1671.

21. Eustis, S. and M.A. El-Sayed, *Why gold nanoparticles are more precious than pretty gold: noble metal surface plasmon resonance and its enhancement of the radiative and nonradiative properties of nanocrystals of different shapes.* Chemical society reviews, 2006. **35**(3): p. 209-217.

22. Kelly, K.L., et al., *The optical properties of metal nanoparticles: the influence of size, shape, and dielectric environment*. 2003, ACS Publications.

23. Yeh, Y.-C., B. Creran, and V.M. Rotello, *Gold nanoparticles: preparation, properties, and applications in bionanotechnology.* Nanoscale, 2012. **4**(6): p. 1871-1880.

24. Billot, L., et al., *Surface enhanced Raman scattering on gold nanowire arrays: Evidence of strong multipolar surface plasmon resonance enhancement.* Chemical Physics Letters, 2006. **422**(4): p. 303-307.

25. Thakkar, K.N., S.S. Mhatre, and R.Y. Parikh, *Biological synthesis of metallic nanoparticles.* Nanomedicine: Nanotechnology, Biology and Medicine, 2010. **6**(2): p. 257-262.

26. Thiruvengadathan, R., et al., *Nanomaterial processing using self-assembly-bottom-up chemical and biological approaches.* Rep Prog Phys, 2013. **76**(6): p. 066501.

27. Li, N., P. Zhao, and D. Astruc, *Anisotropic gold nanoparticles: synthesis, properties, applications, and toxicity.* Angewandte Chemie International Edition, 2014. **53**(7): p. 1756-1789.

28. Nikoobakht, B. and M.A. El-Sayed, *Preparation and growth mechanism of gold nanorods (NRs) using seed-mediated growth method.* Chemistry of Materials, 2003. **15**(10): p. 1957-1962.

29. Cho, K., et al., *Therapeutic Nanoparticles for Drug Delivery in Cancer*. Clinical Cancer Research, 2008. **14**(5): p. 1310-1316.

30. Srivastava, A., et al., *Polymers in drug delivery.* Journal of Biosciences and Medicines, 2015. **4**(01): p. 69.

31. Khalil, I., et al., *Bacterial-Derived Polymer Poly-y-Glutamic Acid (y-PGA)-Based Micro/Nanoparticles as a Delivery System for Antimicrobials and Other Biomedical Applications.* International Journal of Molecular Sciences, 2017. **18**(2): p. 313.

32. Moffitt, M., K. Khougaz, and A. Eisenberg, *Micellization of ionic block copolymers.* Accounts of Chemical Research, 1996. **29**(2): p. 95-102.

33. Kataoka, K., A. Harada, and Y. Nagasaki, *Block copolymer micelles for drug delivery: design, characterization and biological significance.* Advanced drug delivery reviews, 2001. **47**(1): p. 113-131.

34. Bandyopadhyay, S., *Smart and Multifunctional Core-Shell Nanoparticles (NPs) for Drug Delivery.* 2016.

35. Lee, C.C., et al., *Designing dendrimers for biological applications.* Nature biotechnology, 2005. **23**(12): p. 1517.

36. Owen, S.C., D.P.Y. Chan, and M.S. Shoichet, *Polymeric micelle stability.* Nano Today, 2012. **7**(1): p. 53-65.

37. Anees, M., et al., *NANOPARTICLES AS A NOVEL DRUG DELIVERY SYSTEM A REVIEW*. Vol. 2. 2016. 160.

38. Das, N., *Preparation methods and properties of hydrogel: A review.* Int J Pharm Pharm Sci, 2013. **5**(3): p. 112-117.

39. Kamath, K.R. and K. Park, *Biodegradable hydrogels in drug delivery.* Advanced Drug Delivery Reviews, 1993. **11**(1): p. 59-84.

40. Wang, D., et al., *Synthesis and applications of stimuli-responsive hyperbranched polymers.* Progress in Polymer Science, 2017. **64**: p. 114-153.

41. Ebara, M., et al., *Smart biomaterials*. 2014: Springer.

42. Ilić-Stojanović, S., et al., *Stimuli-sensitive hydrogels for pharmaceutical and medical applications.* Facta universitatis-series: Physics, Chemistry and Technology, 2011. **9**(1): p. 37-56.

43. Roy, I. and M.N. Gupta, *Smart polymeric materials: emerging biochemical applications.* Chemistry & biology, 2003. **10**(12): p. 1161-1171.

44. Matteucci, M.L. and D.E. Thrall, *The role of liposomes in drug delivery and diagnostic imaging: a review.* Veterinary Radiology & Ultrasound, 2000. **41**(2): p. 100-107.

45. Gupta, P., K. Vermani, and S. Garg, *Hydrogels: from controlled release to pH-responsive drug delivery.* Drug Discovery Today, 2002. **7**(10): p. 569-579.

46. Cabane, E., et al., *Stimuli-responsive polymers and their applications in nanomedicine.* Biointerphases, 2012. **7**(1-4): p. 9.

47. Painter, P.C. and M.M. Coleman, *Essentials of polymer science and engineering*. 2008: DEStech Publications, Inc.

48. Phillips, D.J. and M.I. Gibson, *Towards being genuinely smart: 'isothermally-responsive' polymers as versatile, programmable scaffolds for biologically-adaptable materials.* Polymer Chemistry, 2015. **6**(7): p. 1033-1043.

49. Prasannan, A., H.-C. Tsai, and G.-H. Hsiue, *Formulation and evaluation of epinephrine-loaded poly (acrylic acid-co-N-isopropylacrylamide) gel for sustained ophthalmic drug delivery.* Reactive and Functional Polymers, 2018.

50. Nayak, S. and L.A. Lyon, *Soft nanotechnology with soft nanoparticles.* Angewandte chemie international edition, 2005. **44**(47): p. 7686-7708.

51. Schild, H.G., *Poly (N-isopropylacrylamide): experiment, theory and application.* Progress in polymer science, 1992. **17**(2): p. 163-249.

52. Kita, R., G. Kircher, and S. Wiegand, *Thermally induced sign change of Soret coefficient for dilute and semidilute solutions of poly(N-isopropylacrylamide) in ethanol*. Vol. 121. 2004. 9140-6.

53. Bekhradnia, S., et al., *Structure, swelling, and drug release of thermoresponsive poly (amidoamine) dendrimer–poly (N-isopropylacrylamide) hydrogels.* Journal of materials science, 2014. **49**(17): p. 6102-6110.

54. Guyton, A. and J. Hall, *Secretory functions of the alimentary tract.* Textbook of medical physiology, 1991. **8**: p. 801-815.

55. Kim, S.W. and Y.H. Bae, *Stimuli-modulated delivery systems.* DRUGS AND THE PHARMACEUTICAL SCIENCES, 2000. **102**: p. 547-574.

56. Kocak, G., C. Tuncer, and V. Bütün, *pH-Responsive polymers.* Polymer Chemistry, 2017. **8**(1): p. 144-176.

57. J., S.M. and P. Ji-Ho, *Hybrid Nanoparticles for Detection and Treatment of Cancer.* Advanced Materials, 2012. **24**(28): p. 3779-3802.

58. Nadagouda, M.N. and R.S. Varma, *A greener synthesis of core (Fe, Cu)-shell (Au, Pt, Pd, and Ag) nanocrystals using aqueous vitamin C.* Crystal Growth and Design, 2007. **7**(12): p. 2582-2587.

59. Bréchignac, C., P. Houdy, and M. Lahmani, *Nanomaterials and nanochemistry*. 2008: Springer Science & Business Media.

60. Bandyopadhyay, S., et al., *Synthesis and in vitro cellular interactions of superparamagnetic iron nanoparticles with a crystalline gold shell.* Applied Surface Science, 2014. **316**: p. 171-178.

61. Corot, C., et al., *Recent advances in iron oxide nanocrystal technology for medical imaging.* Advanced drug delivery reviews, 2006. **58**(14): p. 1471-1504.

62. Wang, Y.-X.J., S.M. Hussain, and G.P. Krestin, *Superparamagnetic iron oxide contrast agents: physicochemical characteristics and applications in MR imaging.* European Radiology, 2001. **11**(11): p. 2319-2331.

63. Tartaj, P., et al., *The preparation of magnetic nanoparticles for applications in biomedicine.* Journal of physics D: Applied physics, 2003. **36**(13): p. R182.

64. Sun, C., J.S.H. Lee, and M. Zhang, *Magnetic nanoparticles in MR imaging and drug delivery.* Advanced Drug Delivery Reviews, 2008. **60**(11): p. 1252-1265.

65. Wang, L., et al., *Monodispersed core− shell Fe3O4@ Au nanoparticles.* The Journal of Physical Chemistry B, 2005. **109**(46): p. 21593-21601.

66. Otsuka, H., Y. Nagasaki, and K. Kataoka, *PEGylated nanoparticles for biological and pharmaceutical applications.* Advanced Drug Delivery Reviews, 2012. **64**: p. 246-255.

67. Yu, H., et al., *Dumbbell-like bifunctional Au− Fe3O4 nanoparticles.* Nano letters, 2005. **5**(2): p. 379-382.

68. O'Connor, C.J., et al., *Fabrication and properties of magnetic particles with nanometer dimensions.* Synthetic Metals, 2001. **122**(3): p. 547-557.

69. Jafari, T., A. Simchi, and N. Khakpash, *Synthesis and cytotoxicity assessment of superparamagnetic iron–gold core–shell nanoparticles coated with polyglycerol.* Journal of Colloid and Interface Science, 2010. **345**(1): p. 64-71.

70. Gupta, A.K. and M. Gupta, *Synthesis and surface engineering of iron oxide nanoparticles for biomedical applications.* Biomaterials, 2005. **26**(18): p. 3995-4021.

71. Capek, I., *Preparation of metal nanoparticles in water-in-oil (w/o) microemulsions.* Advances in colloid and interface science, 2004. **110**(1-2): p. 49-74.

72. Mahmoudi, M., et al., *Superparamagnetic iron oxide nanoparticles with rigid cross-linked polyethylene glycol fumarate coating for application in imaging and drug delivery.* The Journal of Physical Chemistry C, 2009. **113**(19): p. 8124-8131.

73. Sood, A., et al., *Multifunctional gold coated iron oxide core-shell nanoparticles stabilized using thiolated sodium alginate for biomedical applications.* Materials Science and Engineering: C, 2017. **80**: p. 274-281.

74. Prasannan, A., H.-C. Tsai, and G.-H. Hsiue, *Formulation and evaluation of epinephrine-loaded poly(acrylic acid-co-N-isopropylacrylamide) gel for sustained ophthalmic drug delivery.* Reactive and Functional Polymers, 2018. **124**: p. 40-47.

75. Constantin, M., et al., *Smart composite materials based on chitosan microspheres embedded in thermosensitive hydrogel for controlled delivery of drugs.* Carbohydrate Polymers, 2017. **157**: p. 493-502.

76. Chen, S., X. Jiang, and L. Sun, *Reaction Mechanisms of N-isopropylacrylamide Soap-Free Emulsion Polymerization Based on Two Different Initiators.* Journal of Macromolecular Science, Part A, 2014. **51**(5): p. 447-455.

77. Crippa, F., et al., *Dynamic and biocompatible thermo-responsive magnetic hydrogels that respond to an alternating magnetic field.* Journal of Magnetism and Magnetic Materials, 2017. **427**: p. 212-219.

78. Li, S.-D. and L. Huang, *Stealth nanoparticles: high density but sheddable PEG is a key for tumor targeting.* Journal of controlled release: official journal of the Controlled Release Society, 2010. **145**(3): p. 178.

79. Raghunathan, K., *Tailoring Multifunctional Nanoparticles for Encapsulation of Bio-molecules.* Master Thesis NTNU, 2017.

80. Fellows, P., *Food processing technology : principles and practice.* 2016.

81. Guan, Y. and Y. Zhang, *PNIPAM microgels for biomedical applications: from dispersed particles to 3D assemblies.* Soft Matter, 2011. **7**(14): p. 6375-6384.

82. Koppel, D.E., *Analysis of macromolecular polydispersity in intensity correlation spectroscopy: the method of cumulants.* The Journal of Chemical Physics, 1972. **57**(11): p. 4814-4820.

83. *Malvern Instruments, Zetasizer Nano User Manual MANO317.* 2009.

84. Ekkekakis, P., *Illuminating the Black Box: Investigating Prefrontal Cortical Hemodynamics during Exercise with Near-Infrared Spectroscopy*. Vol. 31. 2009. 505-53.

85. Bandyopadhyay, S., et al., *A robust method to calculate the volume phase transition temperature (VPTT) for hydrogels and hybrids.* RSC Advances, 2017. **7**(84): p. 53192-53202.

86. Bruce, C.D., et al., *Molecular Dynamics Simulation of Sodium Dodecyl Sulfate Micelle in Water: Micellar Structural Characteristics and Counterion Distribution.* The Journal of Physical Chemistry B, 2002. **106**(15): p. 3788-3793.

87. Yan, Q. and A.S. Hoffman, *Synthesis of macroporous hydrogels with rapid swelling and deswelling properties for delivery of macromolecules.* Polymer, 1995. **36**(4): p. 887-889.

88. Lue, S.J., C.-H. Chen, and C.-M. Shih, *Tuning of Lower Critical Solution Temperature (LCST) of Poly(N-Isopropylacrylamide-co-Acrylic acid) Hydrogels.* Journal of Macromolecular Science, Part B, 2011. **50**(3): p. 563-579.

89. Costa, P. and J.M.S. Lobo, *Modeling and comparison of dissolution profiles.* European journal of pharmaceutical sciences, 2001. **13**(2): p. 123-133.

90. Dash, S., et al., *Kinetic modeling on drug release from controlled drug delivery systems.* Acta Pol Pharm, 2010. **67**(3): p. 217-23.

91. Ritger, P.L. and N.A. Peppas, *A simple equation for description of solute release II. Fickian and anomalous release from swellable devices.* Journal of Controlled Release, 1987. **5**(1): p. 37-42.

Appendix

A. Significance of recrystallization of NIPAm batch

As stated in Section 3.2.2, NIPAm monomer purchased from Sigma-Aldrich was further purified by recrystallizing it. The recrystallization step was found to very important as presence of impurities in the NIPAm monomer was observed to cause precipitation of the NGs during synthesis. Even though both batches of NIPAm used in this study were recrystallized before further use, NGs synthesized via batch 1 were observed to phase separate and in few cases were observed to stick to the magnet (Figure 7.1). Recrystallizing the same batch again solved this problem thereby highlighting the significance of recrystallization.

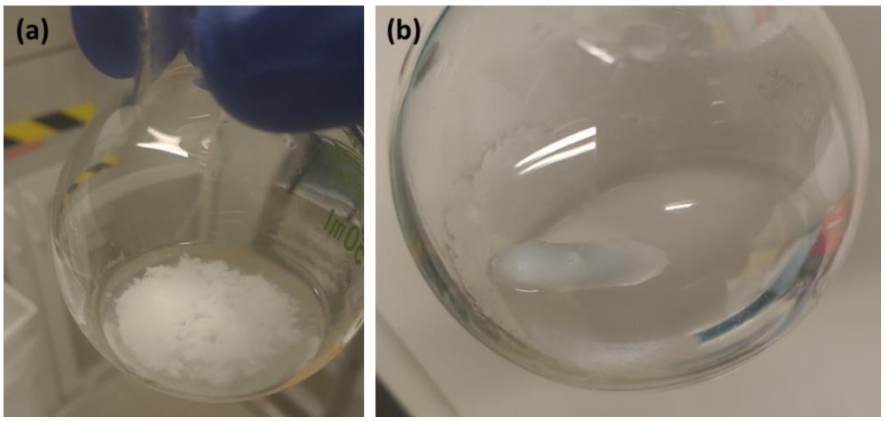

Figure 7.1: Polymers (a) phase separating, (b) sticking to the magnet after the reaction.

B. Effect of stirring speed in synthesis of hybrid NPs

Stirring speed post addition of KPS and AAc were found to have a significant effect in the synthesis of hybrid NPs. As a fraction of Au NPs in the system were observed to stick to the magnet as described in Section 4.3, synthesis reactions were tried at higher stirring speeds of 550 rpm. However, no hybrid NPs were obtained at these stirring conditions. Similar observations were made in hybrid NP synthesis experiments conducted at different mole ratios of AAc. Experiments performed by changing the stirring speed back to 250 rpm post addition of AAc and KPS proved that stirring speed after the addition of comonomer and initiator played crucial role in the synthesis reactions.

C. Size versus Temperature plots

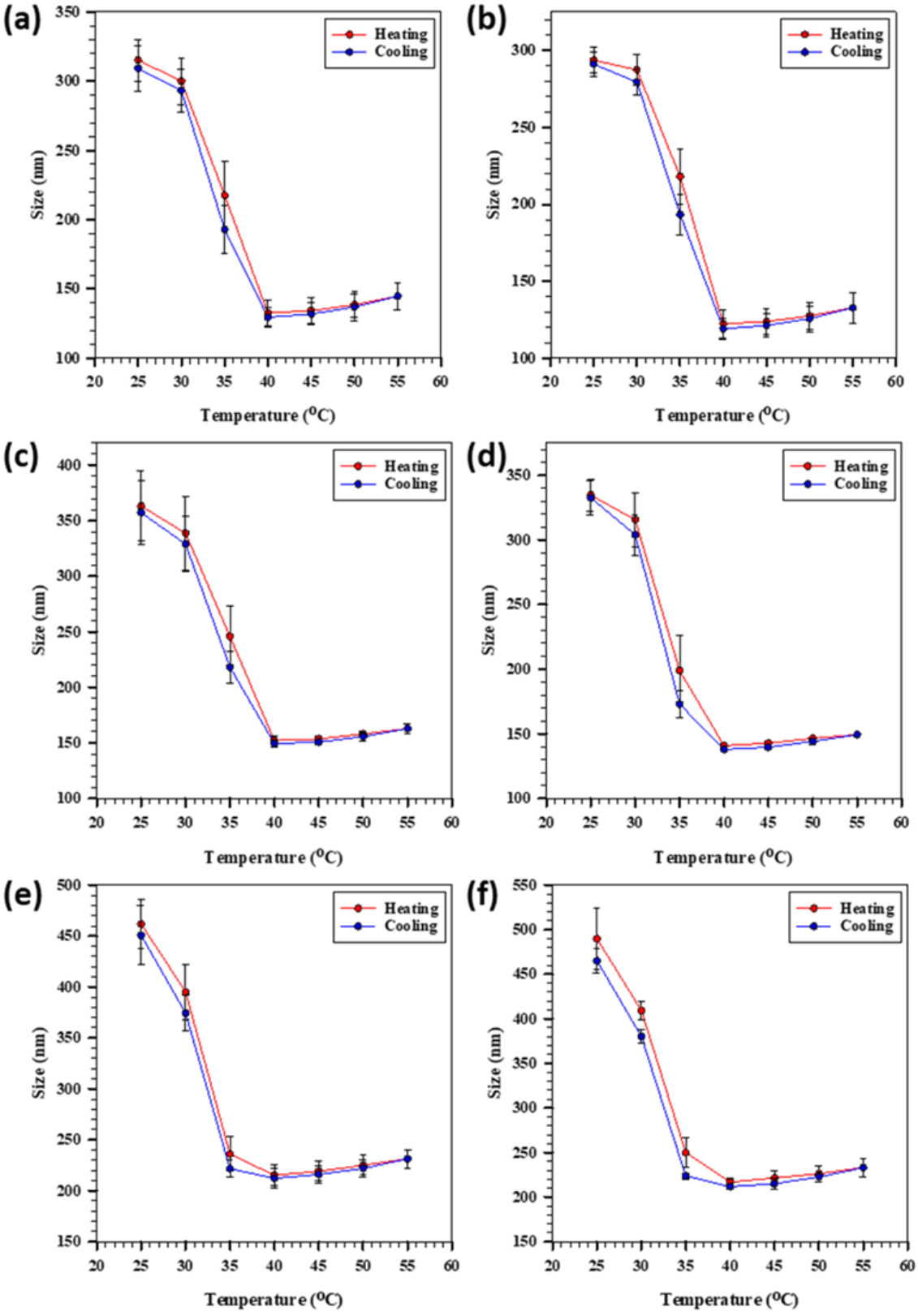

Figure 7.2: Size versus temperature for (a) bNG_10 (b) hNP_10 (c) bNG_15 (d) hNP_15 (e) bNG_25 (f) hNP_25.

D. Curve fitting on normalized growth curves

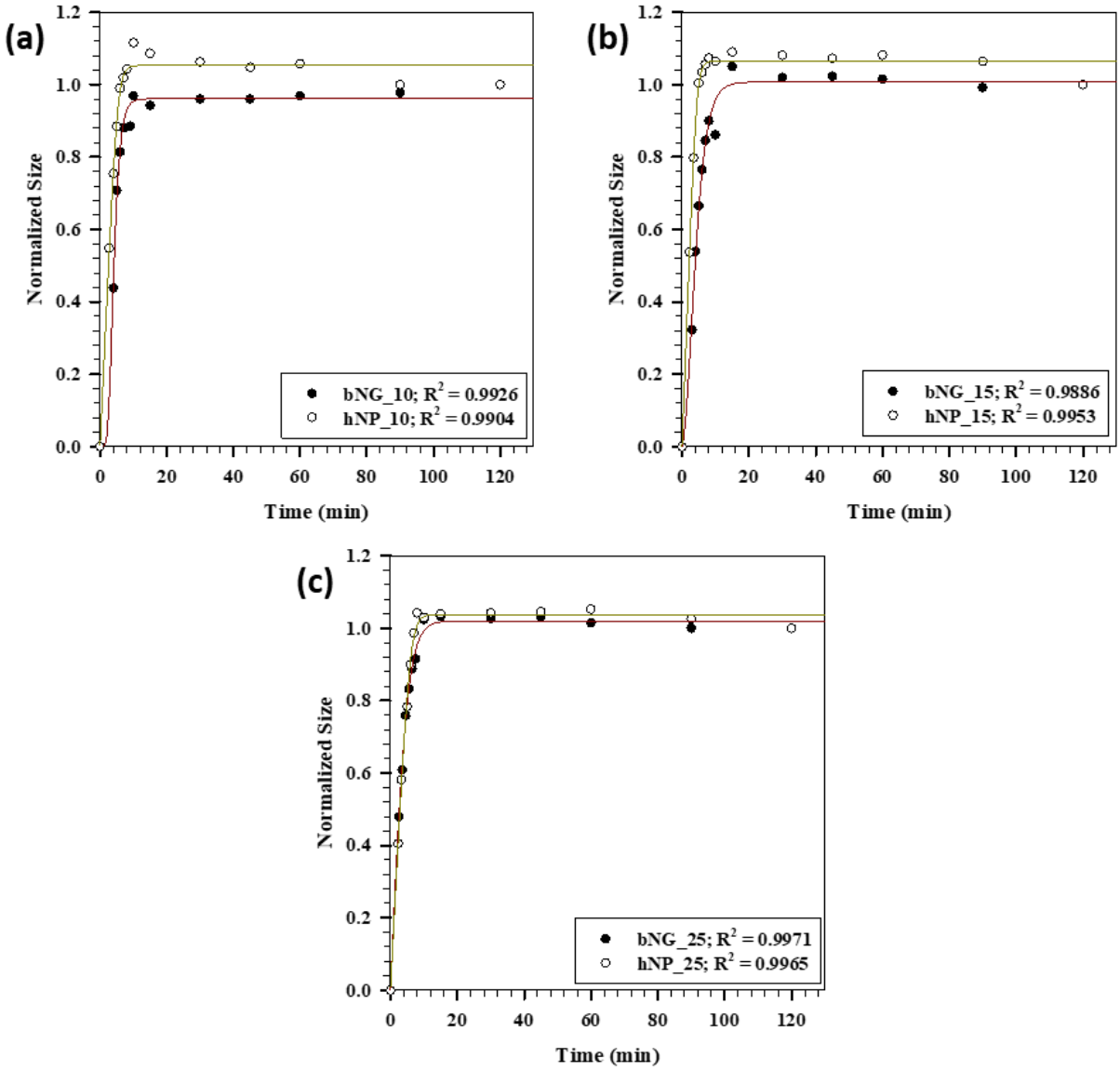

Figure 7.3: Sigmoidal 5 parameter curve fits for growth curves of (a) bNG_10 and hNP_10 (b) bNG_15 and hNP_15 (c) bNG_25 and hNP_25 .

E. Percentage removal of Cyt C using dialysis

Sample calculations to obtain the percentage removal of Cyt C using dialysis have been shown below:-

The 0.5 mg/ml stock solution of Cyt C was sufficiently diluted to prevent saturation of UV-Vis spectrophotometer. 4 ml of 0.167 mg/ml Cyt C (3x dilution of 0.5 mg/ml) was used for dialysis.

Absorbance (t_0) = 1.23892

Absorbance (t_{30min}) = 0.42812

The concentration corresponding to these absorbance values were obtained from the calibration curve equation given below.

$$y = -0.0221 + 0.0075x \tag{10}$$

Conc (t_0) = 168.136 µg/ml

Conc (t_{30min}) = 60.029 µg/ml

Percentage removal of Cyt C at 30 min = $\frac{168.136 - 60.029}{168.136} \times 100$ = 64.29 %

F. Calculating loading and encapsulation efficiencies

The loading efficiencies were calculated by obtaining the absorbance values of bound Cyt C (A_{bound}) after dilution. The absorbance peak of Cyt C was noted at a wavelength of 409 nm. The absorbance noise of bNG/hNP samples at 409 nm was taken into account by subtracting a correction factor ($A_{correction}$) corresponding to their absorbance at 409 nm. A measure of initial concentration of Cyt C was obtained by measuring the absorbance of Cyt C solution (A_{CytC}) at same dilution.

The LEs were calculated using Equation (11)

$$\mathrm{LE} = \frac{\mathrm{A_{bound}} - \mathrm{A_{correction}}}{\mathrm{A_{CytC}}} \times 100 \tag{11}$$

Encapsulation efficiency gives a measure of amount of drug in unit weight of the nanocarrier. EEs were calculated using the following equation.

$$\mathrm{EE} = \frac{\mathrm{LE} \times \text{Mass of drug (µg)}}{\text{Mass of nanocarrier system (mg)} \times 100} \tag{12}$$

Sample calculations for obtaining LE and EE have been shown by considering bNG_15 sample.

A_{CytC} = 1.4756

A_{bound} = 0.81992

$A_{correction}$ = 0.06329

$$LE = \frac{0.81992 - 0.06329}{1.4756} \times 100$$

$$LE = 51.3\ \%$$

Mass of drug = 1000 µg (2 ml of 0.5mg/ml solution)

Mass of nanocarrier system = 1.7 mg

$$EE = \frac{51.3 \times 1000}{1.7 \times 100}$$

$$EE = 301.8\ \mu g/mg$$

G. Finding drug release profiles and kinetics

The percentage release of drug from the nanocarrier system was obtained using the following equation.

$$\text{Drug release } (\%) = \frac{\text{Absorbance at time } (t_0) - \text{Absorbance at time } (t)}{\text{Absorbance at time } (t_0)} \times 100$$

where t_o is the initial time at the start of release and t corresponds to time at the point of measurement.

Cumulative mass of drug released in time t (M_t) was calculated from the % release as follows.

$$M = \frac{\text{Drug release } (\%) \times LE \times \text{Mass of drug}}{100 \times 100}$$

$$M_t = \sum_{0}^{t} M_t$$

The cumulative fraction of drug released (F) in time t was calculated as

$$F = \frac{M_t}{M_\infty}$$

where M_∞ represents the cumulative mass released at the final time point.

Sample calculations for these have been demonstrated by using the release data obtained for bNG_10. The calculations are based on drug release obtained after a time of 4 hrs.

Absorbance at time (t_0) = 0.39236

Absorbance at time (t_4) = 0.29868

LE of bNG_10 system = 31.3 %

Mass of drug introduced = 1 mg

M_∞ = 1.22 mg

$$\text{Drug release (\%)} = \frac{0.39236 - 0.29868}{0.39236} \times 100$$

$$\text{Drug release (\%)} = 23.88\ \%$$

Cumulative mass of drug released in 4 hours was obtained as:-

$$M_4 = 0.39 + \frac{23.88 \times 31.3 \times 1}{100 \times 100} = 0.46\ \text{mg}$$

Cumulative fraction of drug released in 4 hours was obtained by dividing M_4 with M_∞.

$$F = \frac{0.46}{1.22} = 0.38$$

Table 7.1 illustrates the values of parameters obtained for bNG_10 sample (for release at pH 3) to determine the release kinetics.

Time (t)	**% Release**	**Mass released (mg)**	**M_t (mg)**	**F**	**ln(1-F)**	**$t^{0.5}$**	**ln(F)**	**ln(t)**
0.00	0.00	0.00	0.00	0.00	0.00	0.00		
0.17	15.46	0.05	0.05	0.04	-0.04	0.41	-3.22	-1.79
0.33	17.29	0.05	0.10	0.08	-0.09	0.58	-2.47	-1.10
0.50	15.93	0.05	0.15	0.13	-0.13	0.71	-2.08	-0.69
0.75	17.15	0.05	0.21	0.17	-0.19	0.87	-1.77	-0.29
1.00	19.83	0.06	0.27	0.22	-0.25	1.00	-1.51	0.00
1.50	18.03	0.06	0.32	0.27	-0.31	1.22	-1.32	0.41
2.00	19.47	0.06	0.39	0.32	-0.38	1.41	-1.15	0.69
4.00	23.88	0.07	0.46	0.38	-0.48	2.00	-0.97	1.39
6.00	25.62	0.08	0.54	0.44	-0.59	2.45	-0.81	1.79
8.00	26.39	0.08	0.62	0.51	-0.72	2.83	-0.67	2.08
11.00	27.45	0.09	0.71	0.58	-0.88	3.32	-0.54	2.40
15.50	28.77	0.09	0.80	0.66	-1.07	3.94	-0.42	2.74
20.00	30.73	0.10	0.90	0.74	-1.33	4.47	-0.31	3.00
24.00	33.11	0.10	1.00	0.82	-1.73	4.90	-0.20	3.18
29.00	34.36	0.11	1.11	0.91	-2.41	5.39	-0.09	3.37
32.00	34.72	0.11	1.22	1.00		5.66	0.00	3.47

Table 7.1: Release kinetics data for bNG_10 sample at pH 3.

H. Fitting release models for pH controlled release

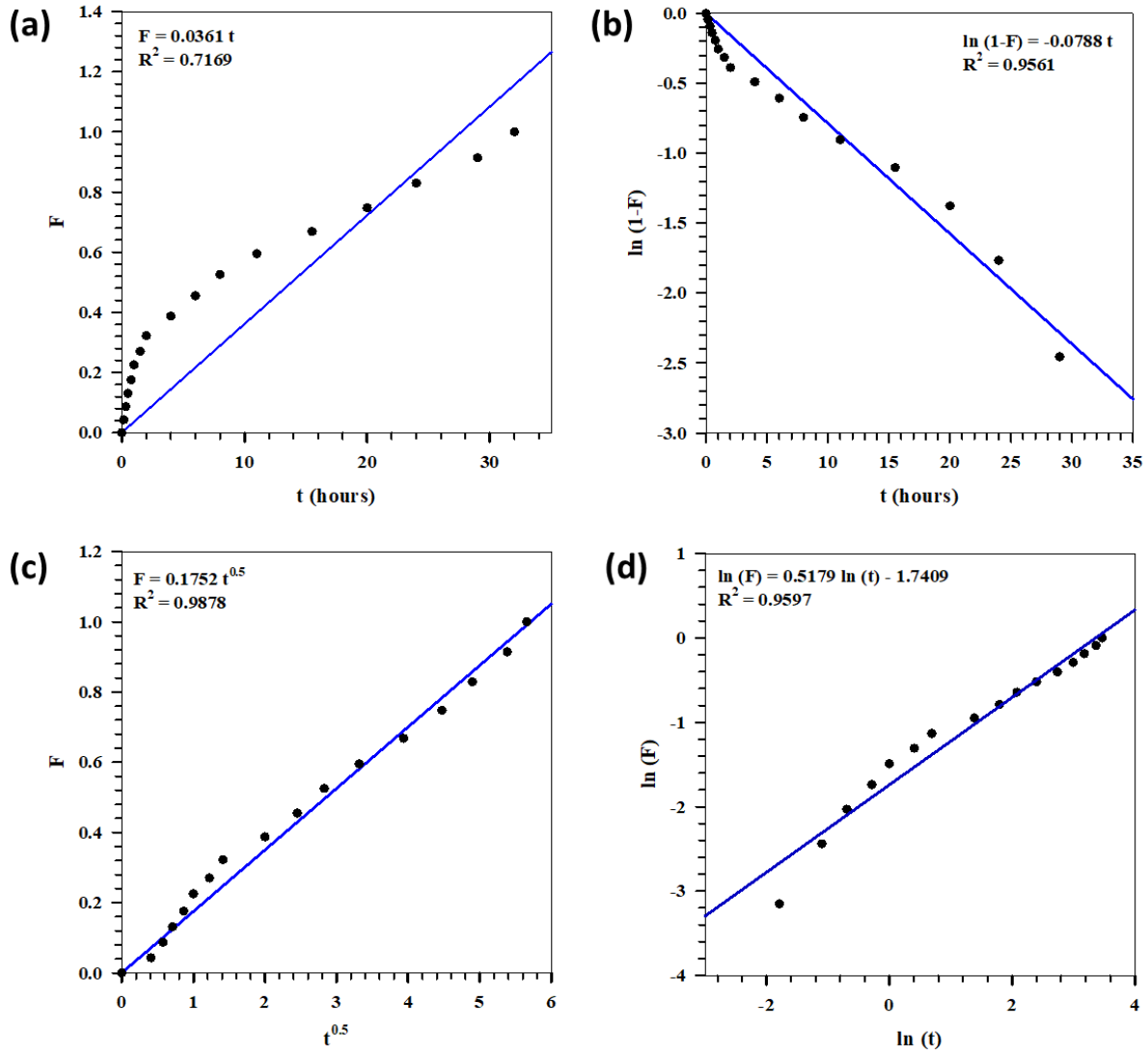

Figure 7.4: Fitting release models in hNP_10 sample for studies performed at pH 3. (a) Zero order model (b) First order model (c) Higuchi model (d) Power law model.

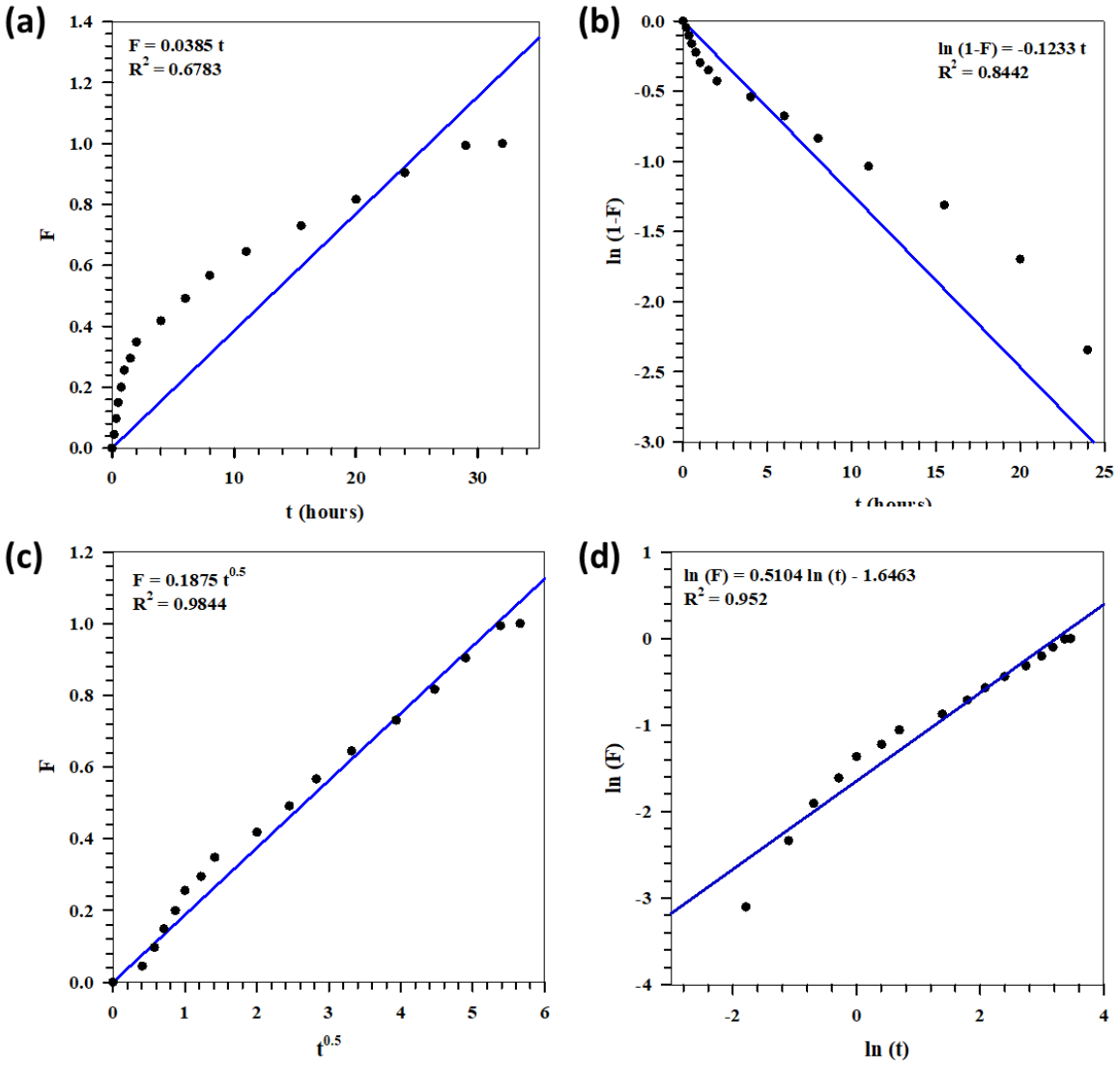

Figure 7.5: Fitting release models in bNG_15 sample for studies performed at pH 3. (a) Zero order model (b) First order model (c) Higuchi model (d) Power law model.

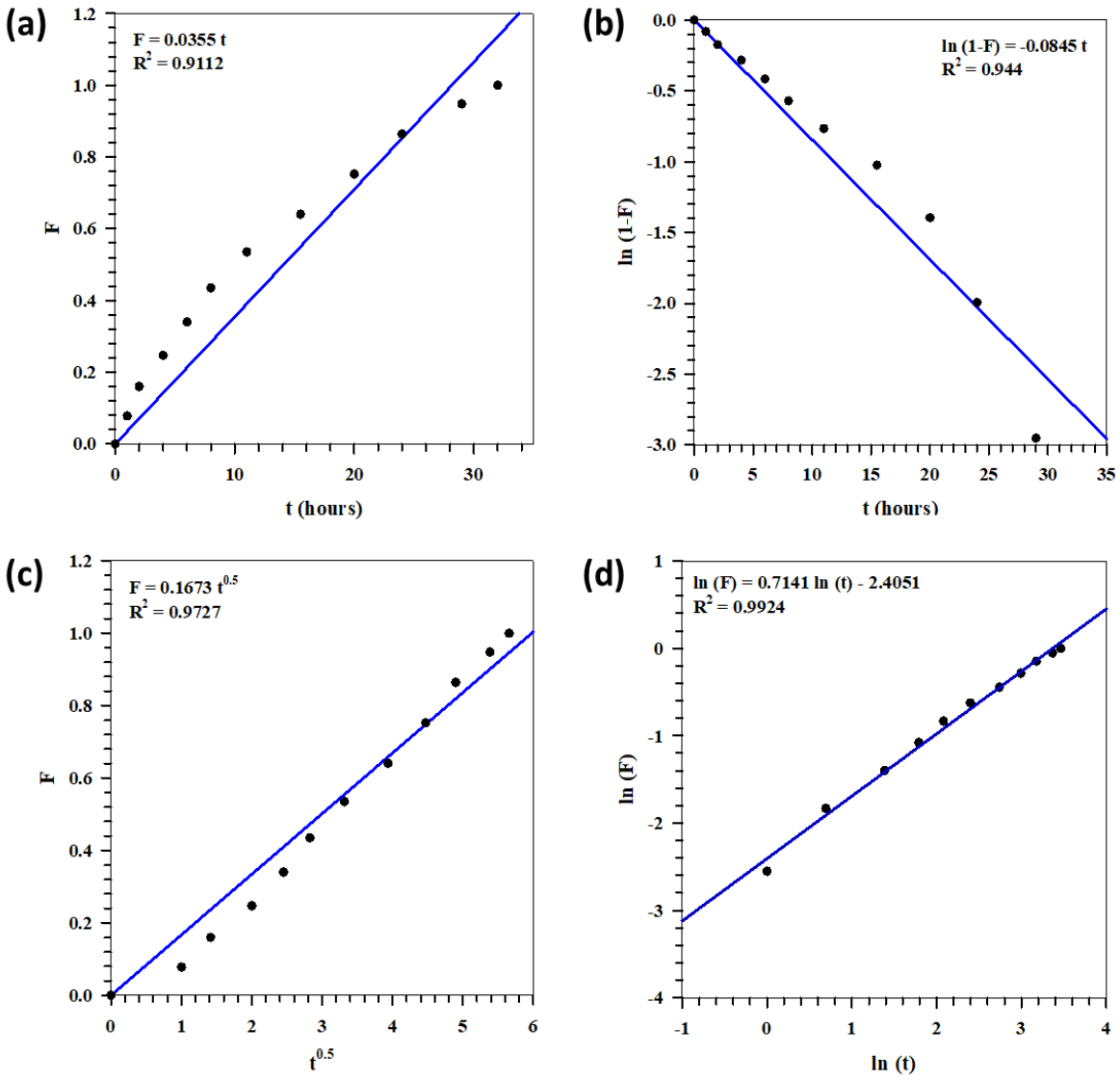

Figure 7.6: Fitting release models in hNP_15 sample for studies performed at pH 3. (a) Zero order model (b) First order model (c) Higuchi model (d) Power law model.

I. Fitting release models for pH + Temperature controlled release

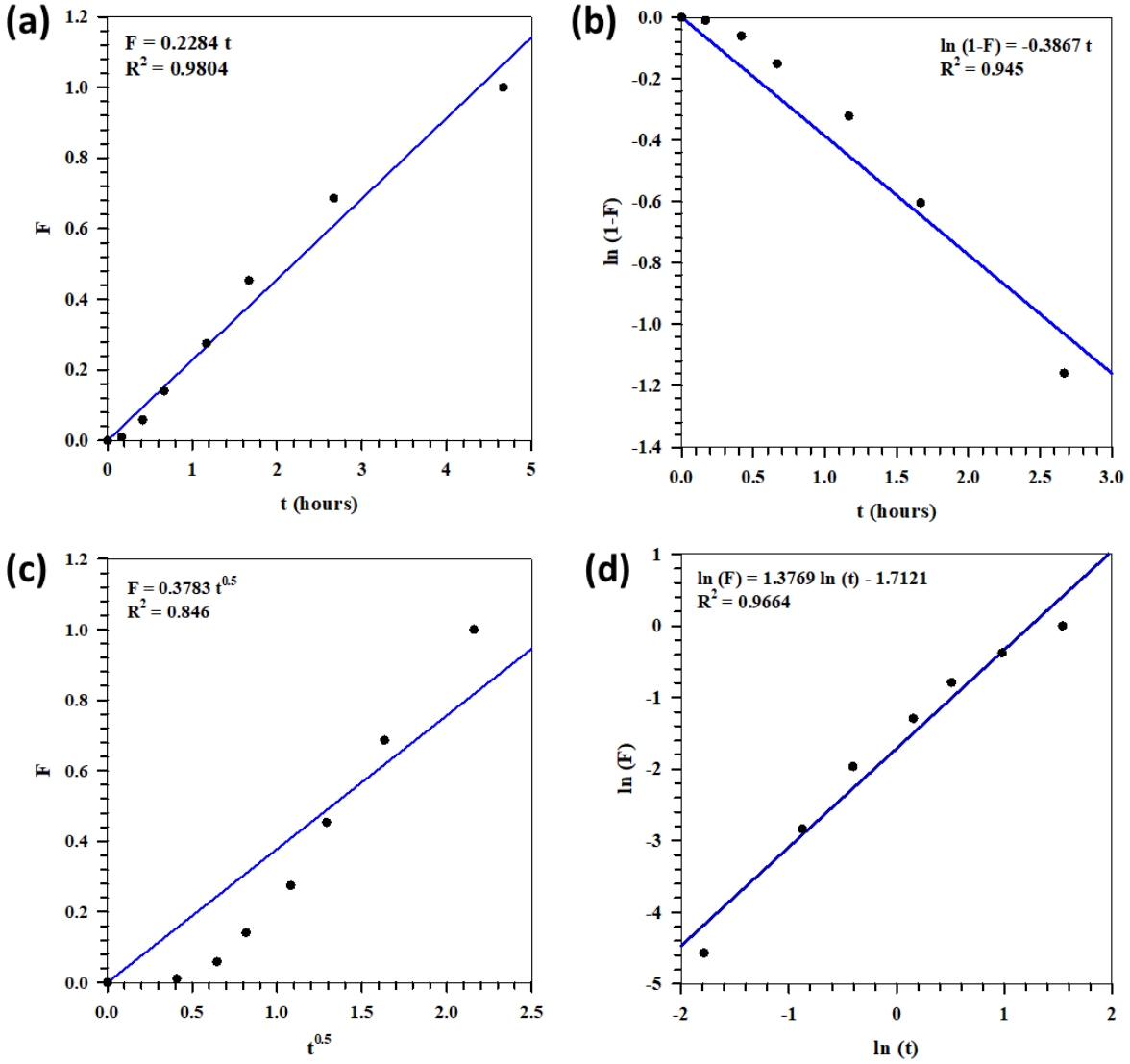

Figure 7.7: Fitting release models in bNG_15 sample for studies performed at pH 3 + 40ºC. (a) Zero order model (b) First order model (c) Higuchi model (d) Power law model.

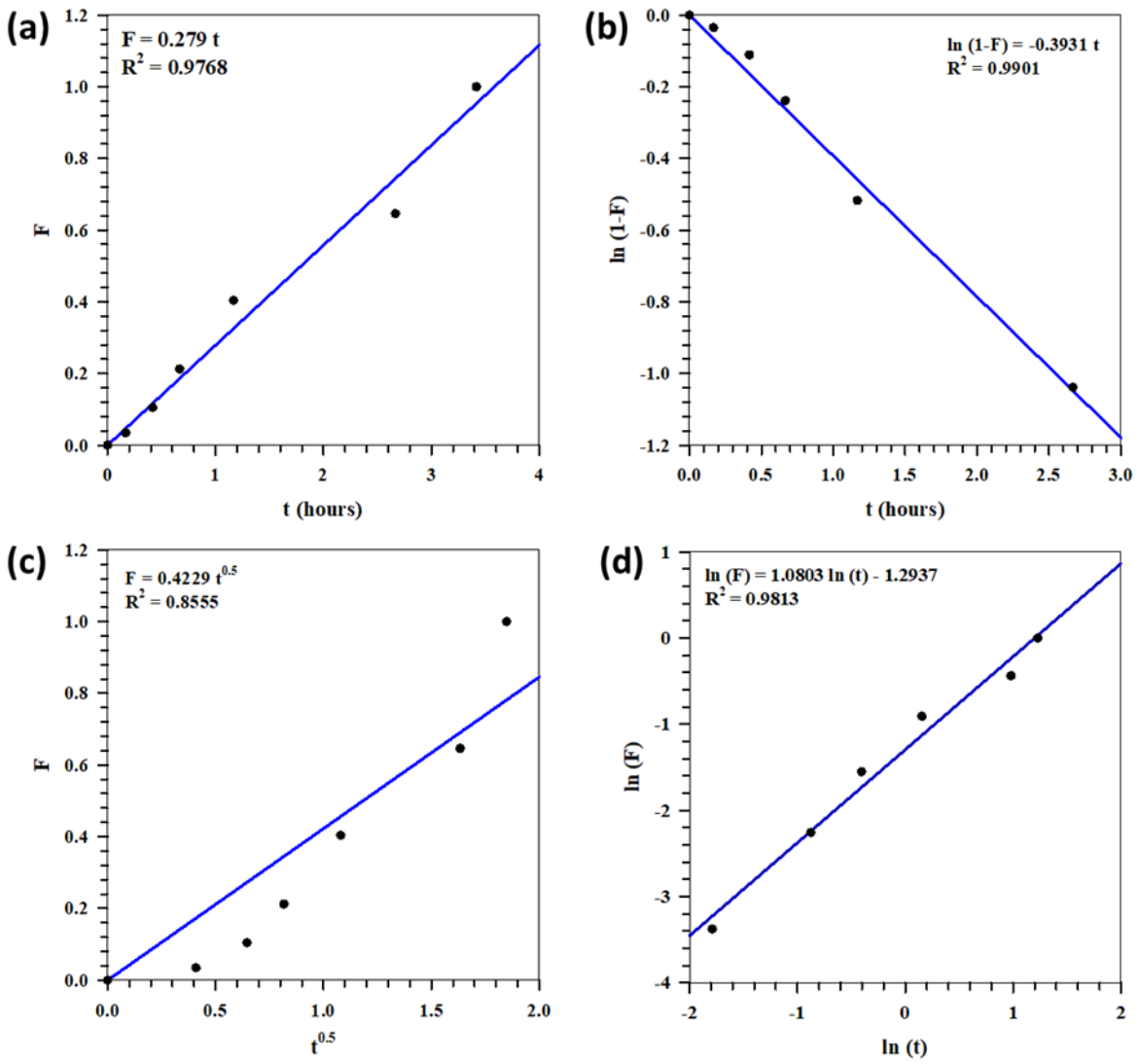

Figure 7.8: Fitting release models in hNP_15 sample for studies performed at pH 3 + 40°C. (a) Zero order model (b) First order model (c) Higuchi model (d) Power law model.

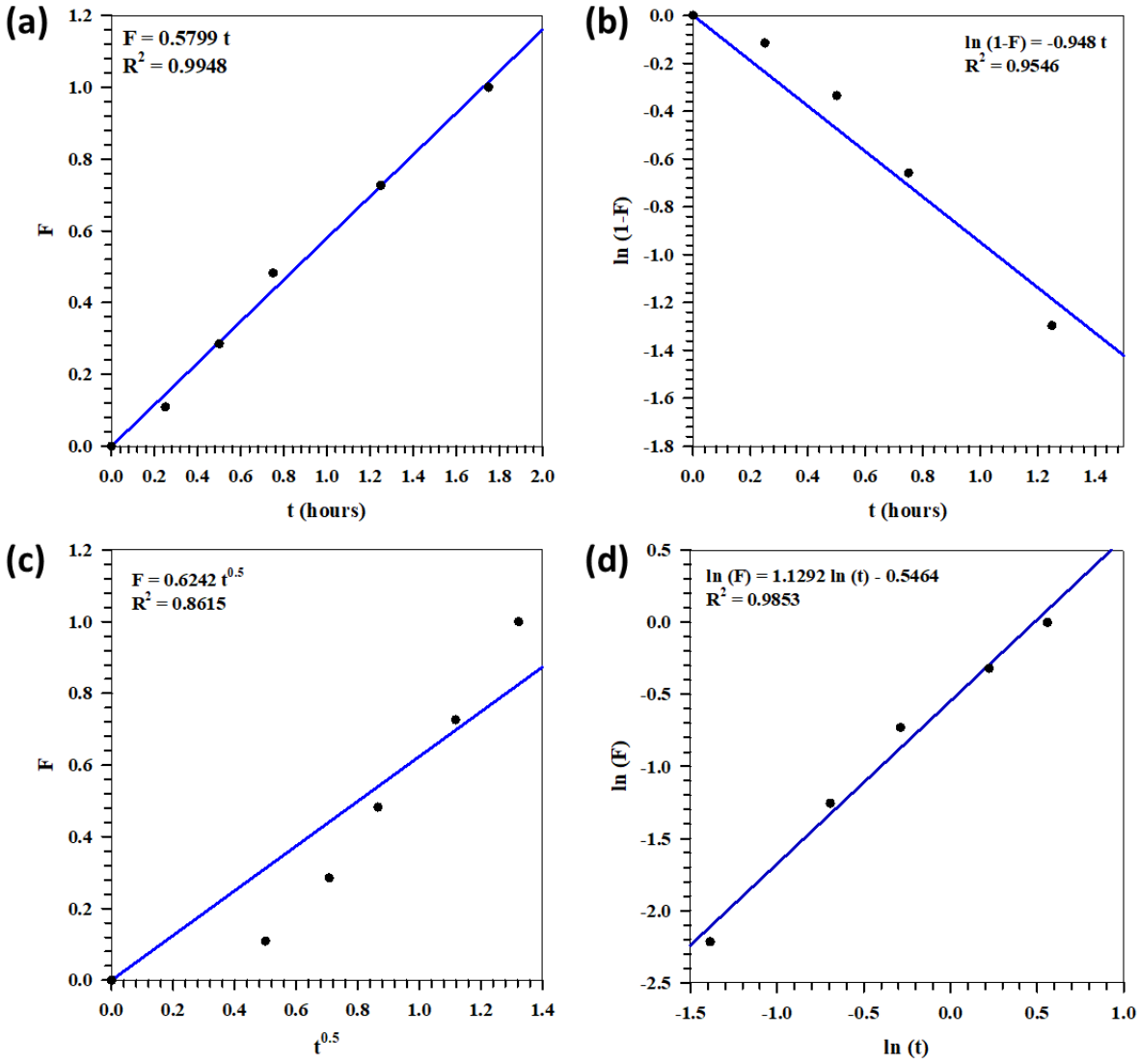

Figure 7.9: Fitting release models in bNG_25 sample for studies performed at pH 3 + 40ºC. (a) Zero order model (b) First order model (c) Higuchi model (d) Power law model.

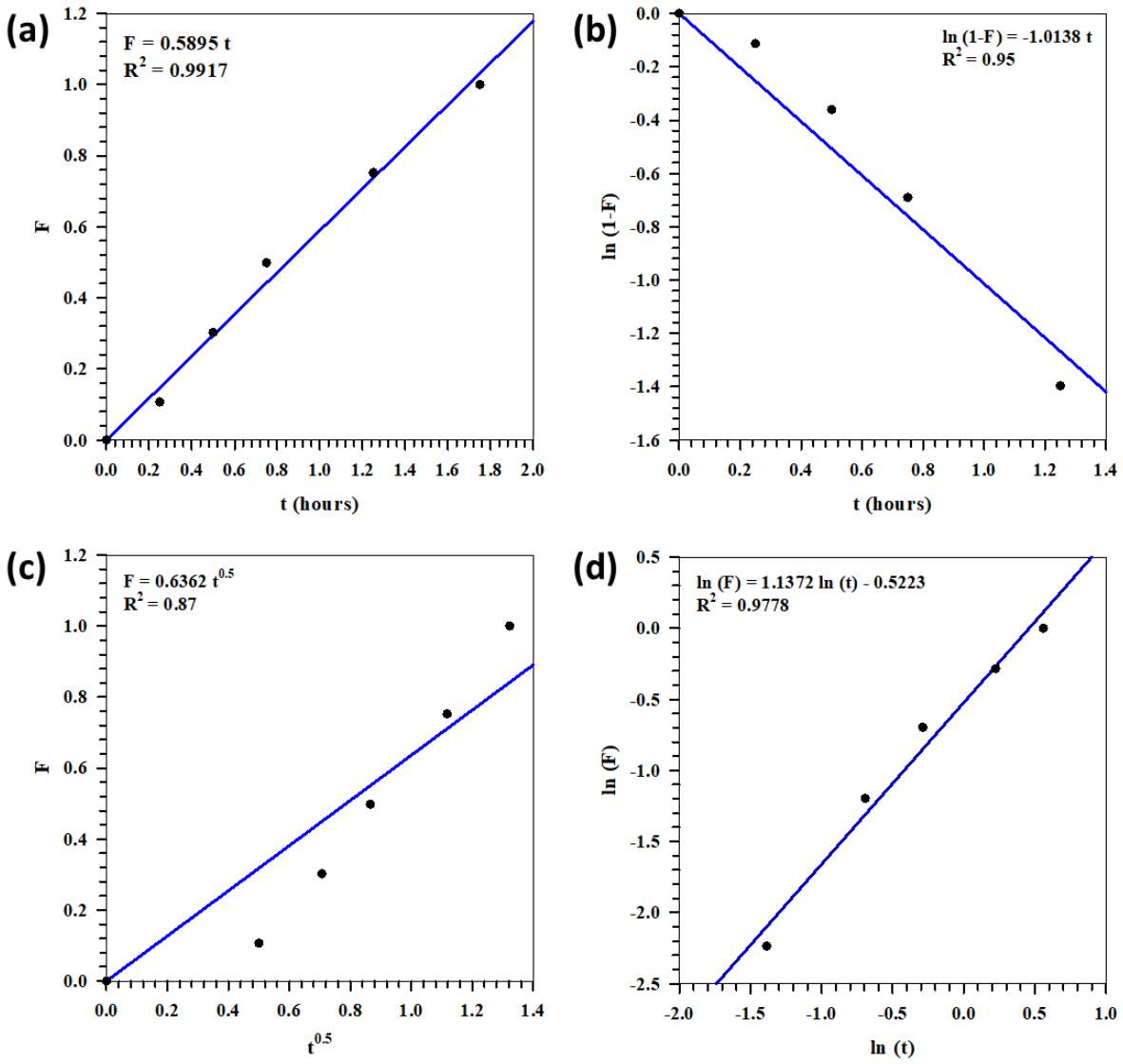

Figure 7.10: Fitting release models in hNP_25 sample for studies performed at pH 3 + 40ºC. (a) Zero order model (b) First order model (c) Higuchi model (d) Power law model.